Study on Forming and Resistive Switching Phenomena in Tantalum Oxide for Analog Memory Devices

Toshiki MIYATANI

Study on Forming and Resistive Switching Phenomena in Tantalum Oxide for Analog Memory Devices

2023

Toshiki MIYATANI

Electronic Science and Engineering
Kyoto University

Abstract

Resistive random access memories (ReRAMs) have attracted great attention as a promising candidate for emerging nonvolatile memory. A single ReRAM cell consists of a thin film of metal oxide sandwiched between electrodes and stores information using the electrical resistance of the oxide. The resistance of the oxide can be controlled by applying a voltage to the ReRAM cells, which is understood as a phenomenon that conductive paths originating from oxygen vacancies, so-called filaments, are repeatedly formed and ruptured in the oxide.

In recent years, research on ReRAMs for analog control of cell resistance has been enthusiastic. However, ReRAM cells based on transition metal oxides generally show abrupt resistive switching when the cell resistance decreases (set process), which inhibits the analog control of the cell resistance by the applied voltage. The abrupt set processes are believed to be attributed to a positive feedback phenomenon that an increase in current due to the growth of filaments causes an increase in Joule heating, which further assists the filament growth. Since it is extremely difficult to directly observe the growth and dissolution process of a filament in a local area (several nm in diameter) of an oxide thin film (several tens nm in thickness), the understanding of the mechanism of the filament growth/dissolution caused by oxygen vacancy transport in the oxide layer is still insufficient.

Based on the above issues, this thesis aims to demonstrate analog resistive switching in both the increase and decrease of the cell resistance, which is called reset and set processes, respectively, and to elucidate the mechanism of the filament growth/dissolution during the analog resistive switching operations in tantalum (Ta) oxide-based ReRAM cells, which are promising for practical use.

In Chapter 2, modeling of a Ta oxide deposition by reactive sputtering was performed, based on the properties of Ta oxide thin films such as chemical composition and density. First, a simplified theoretical model was used to calculate the relationship between the oxygen gas flow rate during deposition and the composition and density of the Ta oxide films. Second, the composition and density of Ta oxide films fabricated with different oxygen gas flow rates during deposition were characterized by Rutherford backscattering spectroscopy. The experimental values of the composition and density were consistent with the theoretical values. Third, the results of X-ray diffraction, cross-sectional transmission electron microscopy, and electron diffraction revealed that the Ta oxide films are microcrystalline close to amorphous. Finally, high-resolution RBS for $TaO_x/TaO_y/Pt$ stacking samples,

where the TaO_y and TaO_x layers were deposited at oxygen gas flow rates of 2.0 sccm and 0.8–1.2 sccm, respectively, revealed that the oxygen composition ratio in the TaO_x layer linearly increases from 1.51 to 2.13 with the oxygen gas flow rate during the TaO_x deposition and that the oxygen composition ratio of the TaO_y layer is 2.5 (stoichiometry). These results indicate that the oxygen composition of the Ta oxide deposited by reactive sputtering was precisely controlled by the oxygen gas flow rate.

In Chapter 3, the impacts of stacking a Ta-rich TaO_x layer on the stoichiometric Ta_2O_5 layer were investigated. Comparing the initial electrical characteristics in Pt/Ta_2O_5/Pt cells and Pt/TaO_x/Ta_2O_5/Pt cells, where the diameter of the Pt top electrode is 100 μm, stacking the TaO_x layer significantly reduces the device-to-device variation. Next, the temperature dependence of the initial conductance was characterized to clarify the electrical conduction mechanism in Pt/TaO_x/Ta_2O_5/Pt cells. As a result, it was revealed that variable range hopping conduction via localized states in the Ta_2O_5 layer is dominant below 200 K, and that variable range hopping conduction and band conduction contribute to the conductance in parallel from 200 K to 400 K. Furthermore, secondary ion mass spectrometry for TaO_x/Ta_2O_5/Pt samples fabricated with isotopic oxygen revealed that oxygen migration occurs from the Ta_2O_5 layer to the TaO_x layer, indicating that the origin of the localized states in the Ta_2O_5 layer could be oxygen vacancies supplied from the TaO_x layer. Finally, analyses of the temperature dependence of the initial conductance based on the variable range hopping conduction equation for Pt/TaO_x/Ta_2O_5/Pt cells revealed that the density of oxygen vacancies supplied from the TaO_x layer to the Ta_2O_5 layer can be controlled by the oxygen composition (1.5–2.1) and thickness in the TaO_x layer.

In Chapter 4, forming and resistive switching characteristics in Pt/TaO_x/Ta_2O_5/Pt cells were investigated for the demonstration of analog resistive switching. First, the author found a unique forming phenomenon (semi-forming) that transitions to a high-resistance state of several kilo-ohms. Moreover, the author investigated the dependence of semi-forming properties on the density of oxygen vacancies supplied from the TaO_x layer to the Ta_2O_5 layer, revealing that the semi-forming phenomenon is more likely to occur when more oxygen vacancies are supplied to the Ta_2O_5 layer. Based on these results, the mechanism of semi-forming was proposed. Second, the author also found that in Pt/TaO_x/Ta_2O_5/Pt cells after semi-forming, set and subsequent reset processes occur at both positive and negative polarities of the applied voltage, so-called complementary resistive switching characteristics. Furthermore, in the complementary resistive switching of Pt/TaO_x/Ta_2O_5/Pt cells, analog control of the cell resistance can be demonstrated even in the set processes. Finally, the author proposed a qualitative model for the origin of the analog resistive switching that the growth and dissolution of the filament compete with each other.

In Chapter 5, the effects of Joule heating generated in the filament on resistive switching characteristics in Pt/TaO_x/Ta_2O_5/Pt cells were investigated from both experimental and theoretical approaches. As for the experimental approach, local Joule heating generated at a single spot in Pt/TaO_x/Ta_2O_5/Pt cells during resistive switching operations was experi-

mentally observed by a temperature imaging microscope. As for the theoretical approach, a coupled simulation of electric potential distribution, temperature distribution, and oxygen-vacancy distribution during a reset process in $Pt/TaO_x/Ta_2O_5/Pt$ cells was performed. Here, key parameters such as the density and conductivity of a filament region dependent on temperature and oxygen vacancy concentration were determined based on the results obtained from Chapters 2–4. As a result of the simulation, current–voltage characteristics and the maximum surface temperature of the $Pt/TaO_x/Ta_2O_5/Pt$ cell in a reset process were consistent with the experimental results. Moreover, the transient distribution of oxygen vacancies in the reset process suggests that the dominant driving force of the oxygen vacancy transport in the filament dissolution process is the oxygen-vacancy drift caused by the electric field.

In Chapter 6, the summary of this thesis was presented, together with suggestions for future work.

Acknowledgments

During my Ph.D. life at Kyoto University, a lot of people supported and encouraged me in so many ways and I would like to thank them here.

First of all, I would like to express my most sincere gratitude to Professor Tsunenobu Kimoto for his continuous and attentive supervision, invaluable advice and suggestions, and ceaseless encouragement. In addition, his generous and graceful personality has deeply inspired me. I am also deeply grateful to Professor Masashi Shiraishi and Associate Professor Kei Kobayashi for their invaluable comments and suggestions through regular discussions on my Ph.D. thesis. I am much indebted to Associate Professor Yusuke Nishi not only for plenty of his insightful comments and advice but also for instructing me in experimental procedures of device process and characterization. He also gave me valuable comments and support in the beginning years of my research life. I have also greatly benefited from Assistant Professor Mitsuaki Kaneko for his constructive comments and support in my daily work, especially during lunchtime. I would also like to thank Assistant Professor Hajime Tanaka for his fruitful comments and suggestions based on his deep understanding of physics.

During my Ph.D., I cloud have a precious opportunity to collaborate with Professor Yukiharu Uraoka and Associate Professor Mutsunori Uenuma in Nara Institute of Science and Technology (NAIST). I am very much obliged to Professor Yukiharu Uraoka for having readily accepted my visit to NAIST for a few weeks despite his busyness. I am full of gratitude to Associate Professor Mutsunori Uenuma for his instructions for my study almost every day, which resulted in fortunate achievements.

Dr. Takuma Kobayashi, Dr. Satoshi Asada, Dr. Takuya Maeda, Dr. Kazutaka Kanegae, and Dr. Keita Tachiki kindly talked to me. I enjoyed discussing topics on research and other activities with them. Thank you.

I would like to show my deep gratitude to Dr. Masaya Arahata Dr. Kouji Ito, Mr. Naoki Kanegami, Mr. Masashi Nakajima, and Mr. Shoma Yamashita for sharing pleasant and precious time in our laboratory.

I appreciate the kindness and supports from the members of our laboratory, thus my special thanks also go to

Dr. Stefanakis Dionysios Mr. Akifumi Iijima, Mr. Taro Enokizono, Ms. Kana Hiramatsu, Mr. Zhao Ying Xin, Mr. Chi Xilun, Mr. Masahiro Hara, Mr. Takuya Ohku, Mr. Chansun

Ku, Mr. Yuto Tsuchiya, Mr. Toshiya Kobayashi, Mr. Osho Yamada, Mr. Ishikawa Ryoya, Mr. Do Euihyeon, Mr. Jin Qimin, Mr. Makoto Imuro, Mr. Mizuki Sato, Mr. Kento Nomoto, Mr. Haruki Fujii, Mr. Noriyuki Maeda, Mr. Taiga Matsuoka, Mr. Kyota Mikami, Mr. Gaku Gouhara, Mr. Katsuya Takahashi, Mr. Akira Inoue, Mr. Takeaki Kitawaki, Mr. Shunya Shibata, Mr. Yuta Murakami, Mr. Shunsei Muraki, B4 Mr. Ryusuke Ikeda, Mr. Shion Toshimitsu, Mr. Manato Takayasu, Mr. Shouta Kozakai, and Mr. Koutarou Kuwahara.

The discussions and chats with them enabled me to spend a meaningful and enjoyable time in this laboratory. In particular, chatting and discussing in coffee breaks mainly with Mr. Masahiro Hara, Mr. Ryoya Ishikawa, and Mr. Haruki Fujii were a great comfort to me when I was writing this thesis. For very kind support in my daily work, I also wish to thank Ms. Yoriko Ohnaka.

This work was partly supported by the Japan Society of Promotion of Science (JSPS) through the Grant-in-Aid for JSPS Research Fellow (JSPS KAKENHI Grant Number 21J15097) and WISE Program, MEXT.

Finally, I sincerely wish to thank my family, and all of my friends for their understanding, support, and heartfelt encouragement.

February, 2023
Toshiki MIAYANI

Contents

Chapter 1

Introduction

1.1 Background

Since the pandemic of COVID-19, most people around the world have been forced to stay their home, and they have kept in touch with the outside world primarily through online virtual spaces. This situation rather facilitated the development of various information technologies (IT) related to the virtual spaces, the so-called "metaverse". Data centers in the real world store the vast amounts of data generated in the metaverse. The field of semiconductor memories, which is a fundamental technology for data centers, has shown remarkable development.

Current semiconductor memories can be broadly divided into volatile memories, such as static random access memory (SRAM) and dynamic random access memory (DRAM) involved in computation, and nonvolatile memories such as Flash memory for storage. Figure 1.1 shows a hierarchical structure of the current semiconductor memories [1]. SRAM and DRAM are suitable for cache and main memories because they can operate at high speeds, though they are not suitable for storage because it requires a power supply for memory retention. In contrast, Flash memory is suitable for storage due to its non-volatility and large capacity, though it is not suitable for computation due to its much slower operating speed compared with SRAM and DRAM. The performance of Flash memory has greatly been improved according to Moore's law by miniaturization [2]. However, the physical limit of miniaturization is approaching, and further dramatic improvement in performance is difficult [3]. However, there is still a large operating speed gap between Flash memory and SRAM/DRAM, so-called the latency gap, as shown in Fig. 1.1. Therefore, research and development of emerging memories, which operate at a higher speed enough to fill the latency gap and have non-volatility, have shown rapid progress in recent years [4–7]. The four leading candidates for the emerging memories are ferroelectric RAM (FeRAM), phase change RAM (PCRAM), spin-transfer-torque magnetoresistive RAM (STT-MRAM), and resistive RAM (ReRAM). Each of these emerging memories has different advantages and disadvantages. FeRAM is superior to other emerging memories in terms of power consump-

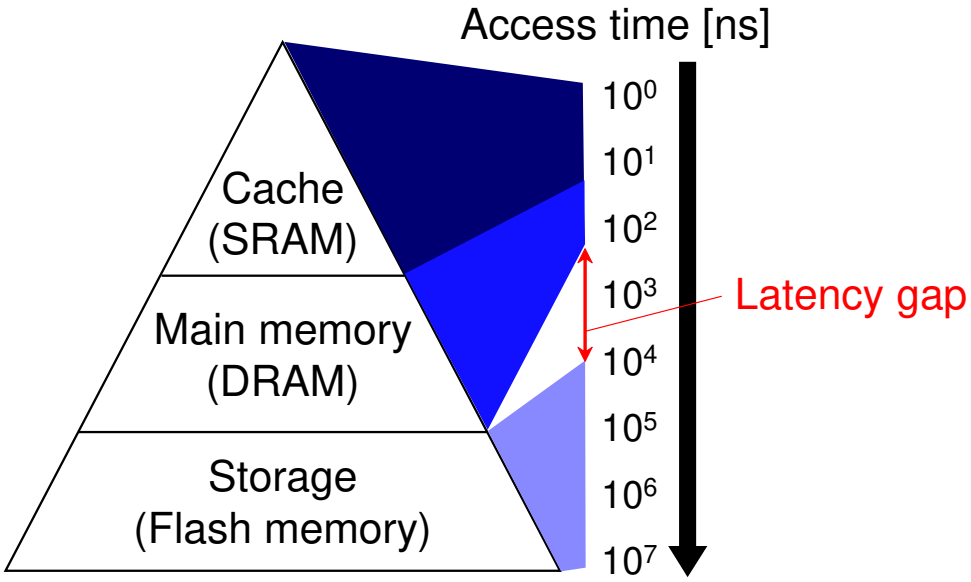

Figure 1.1: Hierarchy of the current semiconductor memory [1].

tion because of the electric field drive, while FeRAM is inferior in terms of the scalability and is needed to rewrite the stored data after readout because the stored data is destroyed at each time of the readout [8–11]. PCRAM has the advantage of integration due to the scalability of phase change materials, while there are issues to be resolved that a high current density and a relatively long current pulse are necessary in a phase change from crystalline to amorphous and from amorphous to crystalline, respectively [12–14]. STT-MRAM enables high-speed writing operations, but its high operating current causes concerns about reliability degradation and an increase in power consumption [15–18]. ReRAM has attracted great attention because of its compatibility with conventional semiconductor fabrication processes and the excellent scalability of its simple metal-oxide-metal (MOM) structure [19–21]. Moreover, ReRAM has various advantages of high writing speeds, low fabrication costs, and low power consumption [21–24]. However, the community faces a big challenge in that the operation principle is not completely clear [25, 26], and thus, ReRAM is a very interesting device in terms of academic research. For reference, Fig. 1.2 shows storage capacity trends of emerging nonvolatile memories [27], and Table 1.1 summarizes the characteristics of the four emerging nonvolatile memories [5, 7].

1.2 Resistive switching phenomenon

1.2.1 Concept of resistive switching operation

A "forming" operation is generally required for ReRAM cells in an initial state. Resistance of ReRAM cells after the forming operation changes reversibly between a high-resistance state (HRS) and a low-resistance state (LRS) by electrical stimuli, which is called a resistive switching (RS) phenomenon. The logic "0" and "1" are assigned to the HRS and LRS, respectively. A writing operation from the HRS to the LRS is called "set" while an erasing operation from the HRS to the LRS is called "reset". Based on voltage polarities at which these RS operations occur, various modes of RS characteristics are well known in ReRAM, as shown in Fig. 1.3. In bipolar RS, the voltage polarities of set and reset operations are opposite to each other, as shown in panels (a) and (b) of Fig. 1.3. Comparing the direction of the trace in the I–V plot to a drawing of the number "8", the operation modes in panels (a) and (b) of Fig. 1.3 are referred to as 8-wise and counter 8-wise RS, respectively [28, 29]. Although these two modes of bipolar RS operations are often recognized as the same, they should be distinguished strictly. Unipolar RS, which is also called nonpolar RS, in panel (c) of Fig. 1.3 shows set and reset operations regardless of voltage polarity. In complementary RS, set and subsequent reset operations occur at both positive and negative voltages, as shown in panel (d) of Fig. 1.3 [30–32]. Here, compliance current (I_{comp}) is often adopted during forming and set operations by a measurement system or an external circuit to avoid current overshoot. Set and reset operations occur above a certain threshold voltage in any RS modes. Therefore, a reading operation is performed at a smaller magnitude of

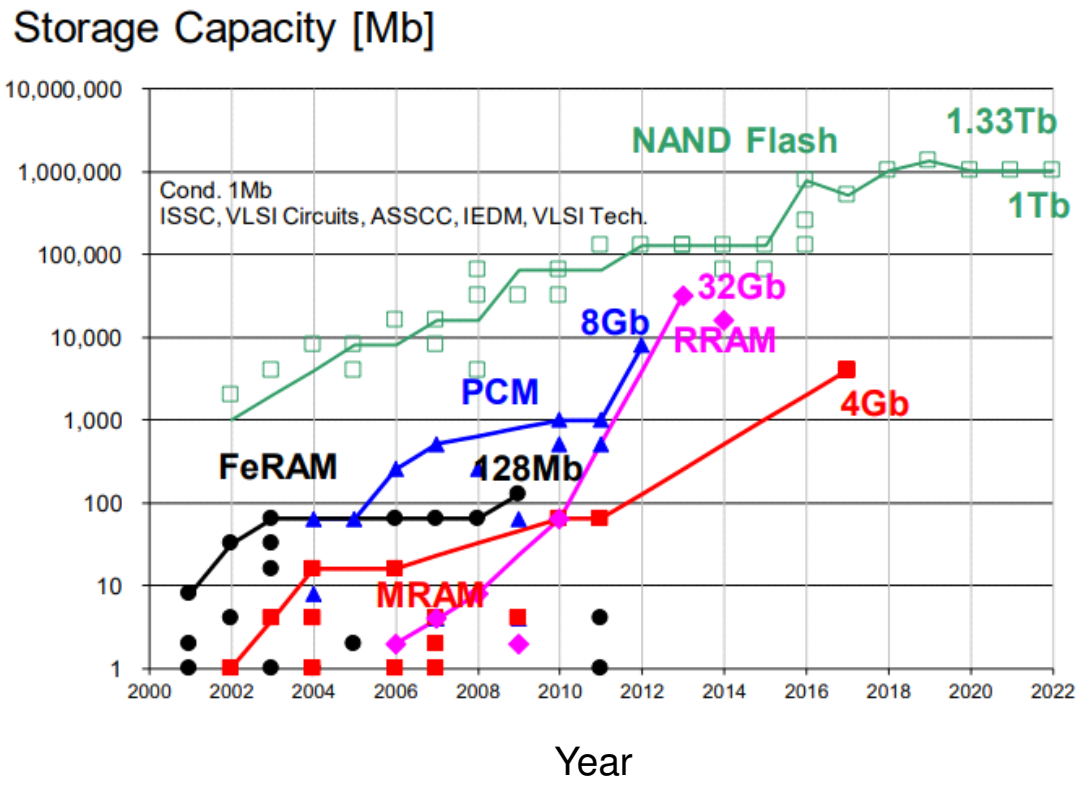

Figure 1.2: Storage capacity trends of emerging nonvolatile memories [27].

Table 1.1: Comparison of the four leading candidates for the emerging nonvolatile memories [5, 7].

	NAND Flash	FeRAM	PCRAM	STT-MRAM	ReRAM
Scalability	$4F^2$	15–35F^2	4–16F^2	6–20F^2	4–6F^2
Write time	$>$ 10 μs	$<$ 10 ns	$\sim$100 ns	$<$ 10 ns	$>$ 20 ns
Read time	$>$ 50 ns	$<$ 20 ns	$<$ 20 ns	$<$ 20 ns	$<$ 20 ns
Power consumption	High	Low	Middle	Middle	Low

(F: the lithographically defined minimum feature size)

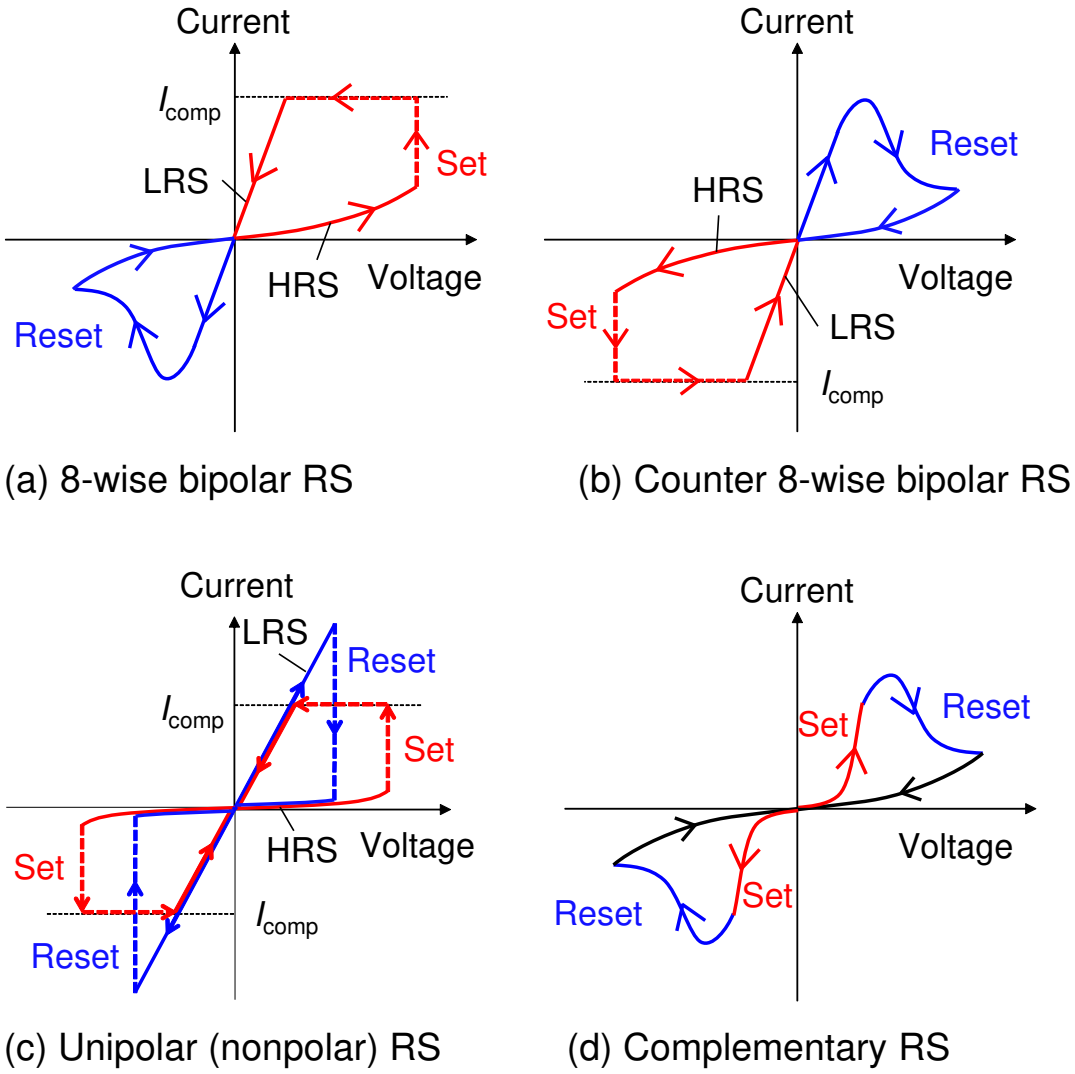

Figure 1.3: Current–voltage characteristics for the four most common modes of RS operation. (I_{comp}: compliance current) The classification is based on voltage polarities at which set and reset operations occur.

voltage than the threshold voltage. In actual memory devices, writing, erasing, and reading operations are performed by applying pulse voltages rather than by voltage sweeps.

1.2.2 Classification based on mechanisms and materials

ReRAM cells can be classified by their basic switching mechanism dependent on various materials of oxides and electrodes. The three main mechanisms of the RS phenomenon are electro-chemical memory (ECM), thermo-chemical memory (TCM), and valence-change memory (VCM). Although these switching behaviors could co-exist in the same cell [33, 34], generally, ECM and VCM show bipolar RS while TCM exhibits unipolar RS.

ECM cells with a metal/insulator/metal (MIM) stack structure include at least one electrochemically active metal such as silver (Ag) and copper (Cu). When applying a positive voltage to the active electrode, the active electrode can be oxidized and dissolve into the insulator layer as cations. The cations migrate to the counter electrode, where the reduction of the cations takes place, leading to the growth of a metallic bridge between both electrodes, a so-called conductive filament (CF), corresponding to forming or set processes. Therefore, ECM cells are also called conductive bridge RAM (CBRAM). Under a negative applied voltage to the active electrode, the metal bridge can be dissolved as a reset process.

TCM cells with an MOM stack structure are typically composed of inert electrodes, such as platinum (Pt) and iridium (Ir), and a single metal oxide, such as nickel oxide (NiO) [35–42] and titanium oxide TiO_2 [33, 43–45]. A forming process in TCM cells is believed to be the formation of local CFs with metal-rich or oxygen-deficient chemical composition by electrical stress. Set and reset processes independent of the voltage polarity in TCM cells indicate the CF is formed and dissolved due to thermo-chemical redox reactions in the metal-oxide layer [46, 47].

In VCM cells, a metal-oxide layer is sandwiched between electrodes with different oxygen affinity. In particular, the filamentary-type of VCM cells with two oxide layers, which are composed of a metal-rich layer and a stoichiometric layer, have been investigated intensely, such as TaO_x/Ta_2O_5 [48, 49] and Hf/HfO_x [50, 51]. It was demonstrated that the bilayer structure improved the performance of memory devices [48, 51–53]. Figure 1.4 illustrates a schematic of the mechanism in the filamentary-type of VCM. The forming process generates ionic defects such as oxygen vacancies (V_Os) in the stoichiometric layer by a valence change in the cations, resulting in the formation of the oxygen-deficient CFs. When a negative voltage is applied to the top inert electrode in the LRS, V_Os are driven toward the metal-rich layer across the electric field, leading to the dissolution of the CF, corresponding to the reset process. The filament gap mainly contributes to the cell resistance in the HRS. On the other hand, when a positive voltage is applied in the HRS, V_Os migrate to the bottom electrode and the CF grows again, corresponding to the set process. Thus, the CFs in VCM can be formed and dissolved by the migration of the cations or V_Os due to the electric field.

In contrast, a forming process is typically unnecessary for the interface-type of VCM [54],

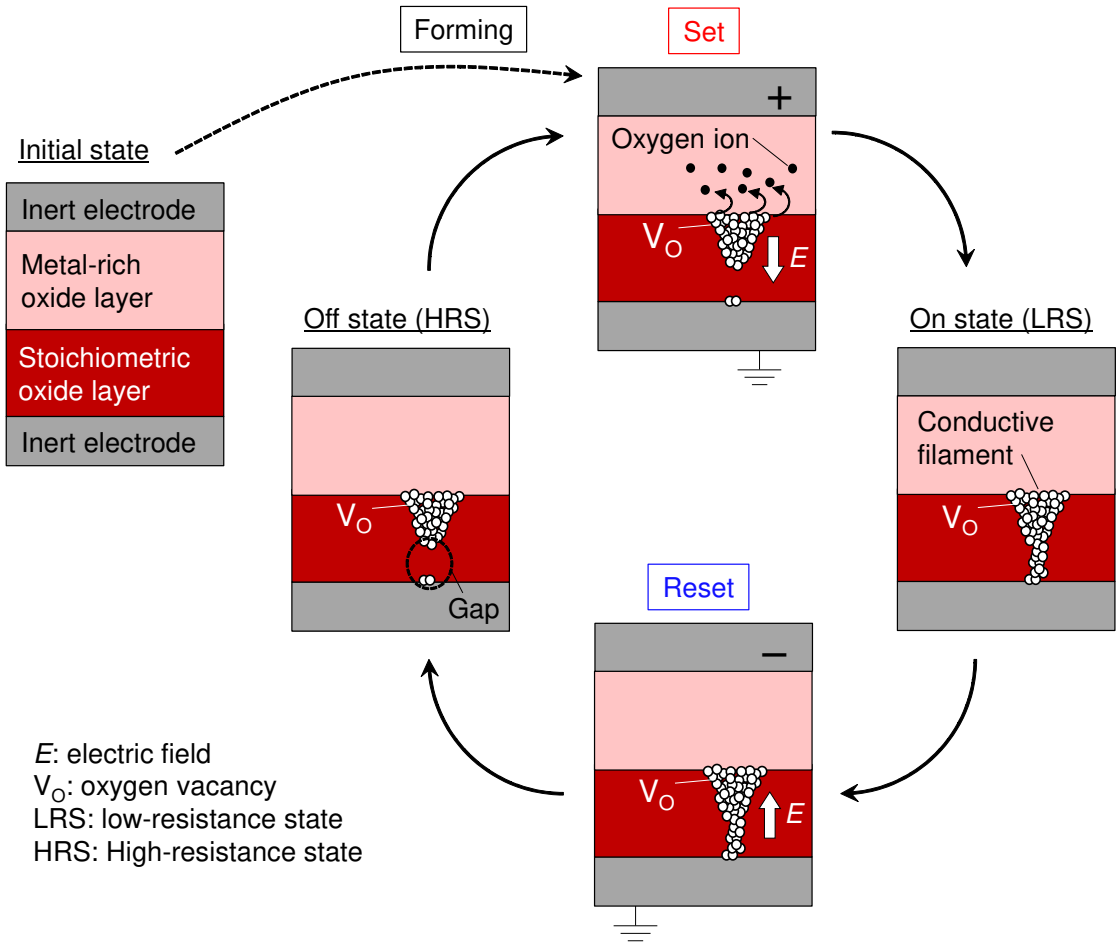

Figure 1.4: Schematic of mechanism in the filamentary-type of VCM.

which occur only when perovskite oxides such as $Pr_{0.7}Ca_{0.3}MnO_{3-\delta}$ [55] and $SrTiO_{3-\delta}$ [56] are used. Although some mechanisms of the RS phenomenon in the interface-type of VCM are proposed, the prevailing model is a valence change in the interfacial layer between the electrode and the oxide layer due to the migration of V_O [57, 58].

1.2.3 Application for emerging nonvolatile memory devices

ReRAM has been studied in various oxides for more than five decades with the goal of a nonvolatile memory that is high-speed, high-integration, and compatible with conventional silicon CMOS technology. In particular, VCM-type ReRAM has been developed rapidly since the 2000s. In this section, the performance and advantages of the filamentary-VCM ReRAM (hereafter simply referred to as ReRAM) are described in various aspects. Great scalability is a major advantage of ReRAM, compared with other emerging memories. Device sizes of 10 nm $\times$ 10 nm have been demonstrated [51]. The scalability is attributed to the fact that RS phenomena are associated with ionic motions within a much more localized spot [59]. The reading operation is nondestructive, which is different from FeRAM, and the writing speed is in the order of nanoseconds [60]. One of the key reasons for the fast operation is considered that the nano-scale switching region is under a very high electric field and Joule heating during switching, leading to enhancement of ion mobility [61, 62]. When removing the electrical pulse, the heated region cools down quickly to the ambient temperature, which causes decreasing the ion mobility again. This leads to great retention under low bias and room temperature (RT). Moreover, a very high endurance of 10^{12} cycles has been reported in TaO_x-based ReRAM cells [48], which is superior to that of 10^5 cycles in NAND Flash memories.

As shown in Fig. 1.5 [30], in case the read-out cell is in the HRS and the surrounding cells are in the LRS, the reading current can easily flow through the surrounding cells, which is called a sneak path current issue. To prevent the sneak path current issue, each memory cell is connected to a transistor, which is called one-transistor-one-resistor (1T1R), in the crossbar memory array. Fig. 1.6 shows the schematic of the 1T1R architecture. Word lines and bit lines are connected to transistor gates and RS cells, respectively. Source lines are connected to the common source of transistors. The range of 1T1R cell area is $6F^2$ (F: the lithographically defined minimum feature size). The transistor plays several important roles: (i) electrical isolation as a selector device for suppression of the sneak path current; (ii) current compliance to prevent current overshoot at forming and set operations; (iii) voltage regulation to allow sufficient voltage on the RS cell during reset and read operations.

1.2.4 Application for synaptic analog memory devices

The era of the Internet of Things (IoT) generates more and more digital data all over the world every day. Processing of these big data requires further development of AI (artifi-

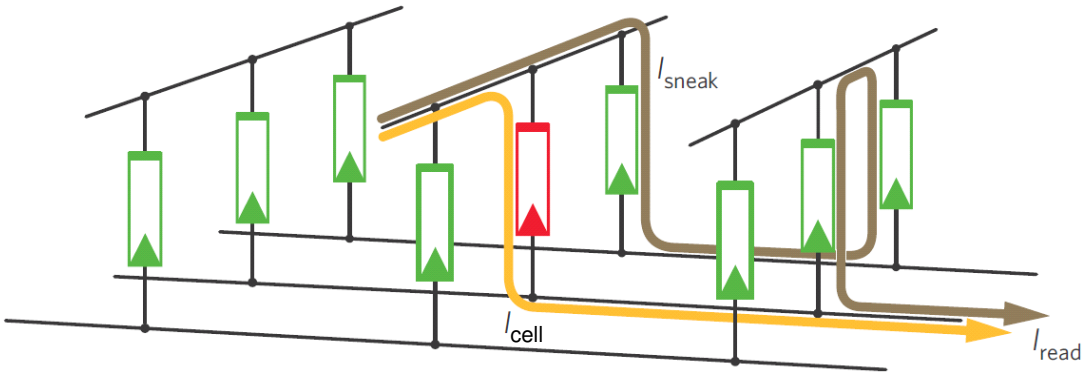

Figure 1.5: A sneak path issue in a crossbar architecture [30]. Only the addressed cell in the center of the crossbar array is in the HRS (red), and all surrounding cells are in the LRS (green). The current through the addressed cell (I_{cell}) and through the neighboring cells (I_{sneak}) flow when reading.

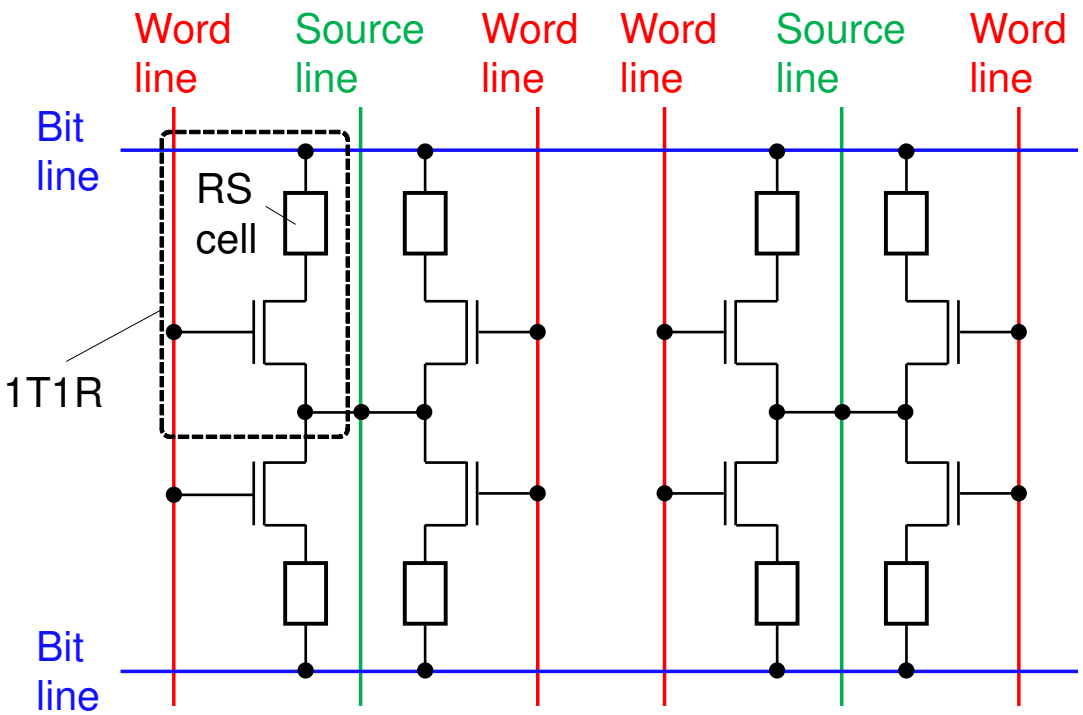

Figure 1.6: A schematic of the 1T1R architecture.

cial intelligence) technology. Deep neural network (DNN) has been studied as one of the AI technology [63]. Figure 1.7 (a) shows a illustration of a biological neural system with pre-neurons connected with a post-neuron via synapses [64, 65]. Moreover, Fig. 1.7 (b) shows a simple perceptron that models the biological neural system, where an output value y is determined by the accumulation of input values x_{i} multiplied by the synaptic weight w_{i}. The multiply-accumulate (MAC) operation is conventionally performed by utilizing massively parallel computing hardware such as GPU [66, 67]. However, a conventional von Neumann-type computer architecture, where the data processing units and the memory units are separated, faces a physical limit of dramatic improvement in power and speed of computation, so-called the von Neumann bottleneck [68, 69]. As one of the novel computing architectures to solve the problems, neuromorphic computing, which mimics the human brain working with extremely low power consumption, has been intensively studied [70, 71]. Fig. 1.8 shows a schematic of a perceptron circuit using analog memory devices in the neuromorphic computing. The synaptic weight can be stored in a single analog memory device, allowing the memory units to be incorporated into the data processing units, and so enabling parallel computations with high speed and low power consumption without the conventional massively parallel computing hardware [63, 72–74]. Such a computer architecture is also called in-memory computing. ReRAM is a promising candidate not only for emerging nonvolatile memories but also for analog memory devices, because ReRAM exhibiting gradual RS characteristics has the possibility to achieve analog control of cell resistance as synaptic weights by applying a voltage [23, 75].

1.3 Key issues for resistive switching cells

In this section, several important issues in the field of ReRAM are presented, focusing on the insufficiency of the previous reports and the need for further studies.

Transport properties of oxygen vacancy

As mentioned in 1.2.2, the operating principles of the filamentary-VCM ReRAM are understood by the phenomenon that the growth and dissolution of the CFs repeatedly occur by applying a voltage. However, the growth and dissolution processes of the CFs are difficult to observe experimentally because the growth and dissolution processes occur in an unpredictable localized spot (a diameter of a few nano-meters) and in ultra-thin oxide films ($\sim$10 nm). Therefore, the mechanism of the growth and dissolution processes of the CFs, in other words, transport properties of V_Os in the oxide films during resistive switching operations are still unclear. Although the mechanism of the CF's growth and dissolution has not been clarified, its practical application is progressing. Fundamental research on the mechanism is essential to establish guidelines for device design to improve performance.

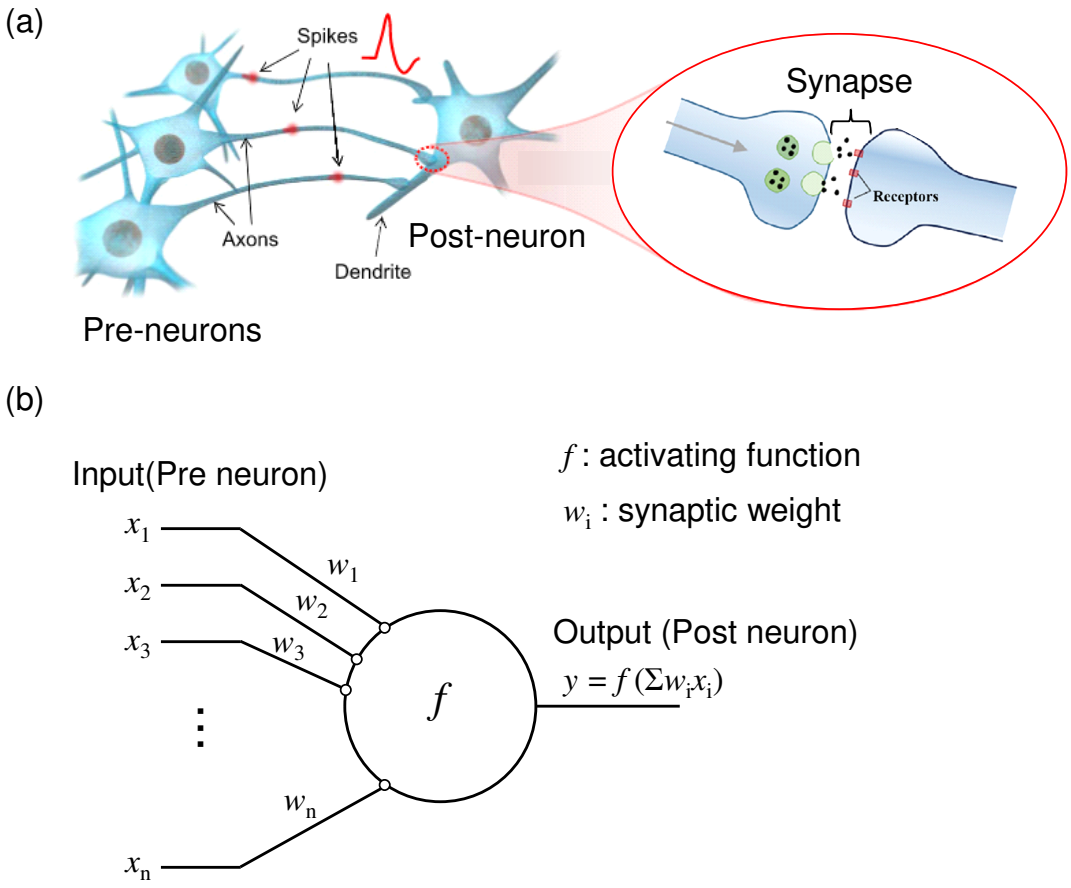

Figure 1.7: (a) A biological neural system with pre-neurons connected with a post-neuron via synapses [64, 65]. (b) A simple perceptron that models the biological neural system, where an output value y is determined by the accumulation of input values x_i multiplied by the synaptic weight w_i [66, 71].

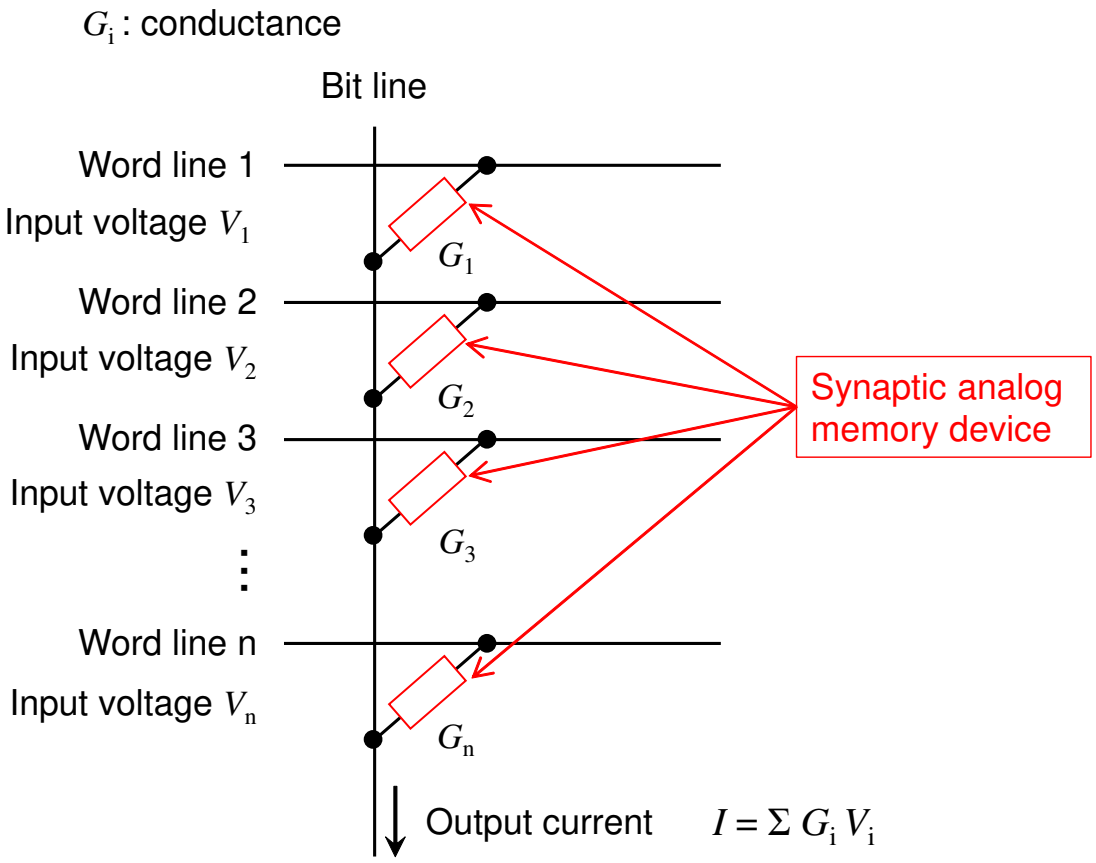

Figure 1.8: A schematic of a perceptron circuit using analog memory devices in the neuromorphic computing.

Impacts of stacking a metal-rich layer and a stoichiometric layer

Most ReRAM cells already in practical use have a structure of stacking a metal-rich layer on a stoichiometric layer. This is because the bilayer-oxide structure improves performance, such as endurance, retention, and reliability [48, 51–53]. Here, the metal-rich layer is believed to act as a reservoir layer that supplies V_Os to the stoichiometric layer under applying a voltage [52, 76]. However, it is extremely difficult to experimentally observe the V_O supply under applying a voltage in an unpredictable localized spot in the ultra-thin oxide films. Therefore, impacts of stacking a metal-rich layer and a stoichiometric layer on electrical characteristics has not been completely clarified.

Abrupt set processes

Numerous studies have reported gradual reset processes in binary transition-metal-oxide-based RS cells [77–81]. The gradual reset processes enable the multi-level or analog control of the cell resistance by the magnitude of the applied voltage. In contrast, most binary transition-metal-oxide-based RS cells exhibit abrupt set processes [71, 82–84]. The abrupt set processes might be caused by positive feedback between the filament growth and a rise in Joule heating [65, 78]. Some previous studies have demonstrated multi-level control of the cell resistance by suppressing the rise in Joule heating with compliance currents, which induce undesired external circuits [65, 77, 85]. Therefore, setting the compliance current is not desirable. As a result, suppressing the abrupt set processes is the major challenge of ReRAM for the analog memory application.

1.4 Purpose and outline of this thesis

Based on the issues mentioned in Sec. 1.3, the purpose of this thesis is controllable demonstration of analog resistive switching and to elucidate the mechanism of the CF's growth and dissolution during the analog resistive switching operations. As an oxide material, the author selected a tantalum oxide, which has been reported to be stable in various compositional states and is also in practical use.

In Chapter 2, for modeling reactive sputtering deposition of tantalum (Ta) oxide in the author's experimental system, the relationship between deposition conditions of Ta oxide films and various properties of Ta oxide films deposited by reactive sputtering, such as crystallinity and chemical composition, is investigated. Moreover, a simplified theoretical model for reactive sputtering is used to calculate the relationship between the oxygen gas flow rate during deposition and the chemical composition of the Ta oxide films.

In Chapter 3, the impacts of introducing a Ta-rich TaO_x layer on initial characteristics in $Pt/Ta_2O_5/Pt$ cells are investigated by comparing the electrical properties of $Pt/Ta_2O_5/Pt$ and $Pt/TaO_x/Ta_2O_5/Pt$ cells. In addition, temperature dependence of initial conductance is characterized to clarify the electrical conduction mechanism in $Pt/TaO_x/Ta_2O_5/Pt$ cells.

Furthermore, secondary ion mass spectrometry for $TaO_x/Ta_2O_5/Pt$ samples fabricated with isotopic oxygen is performed to reveal oxygen migration between the Ta_2O_5 layer and the TaO_x layer.

In Chapter 4, forming and RS characteristics in $Pt/TaO_x/Ta_2O_5/Pt$ cells when oxygen composition and thickness of the TaO_x layer varied are investigated in detail for the demonstration of analog RS characteristics, focused on a unique forming phenomenon (semi-forming) observed in $Pt/TaO_x/Ta_2O_5/Pt$cells.

In Chapter 5, the effects of Joule heating generated in the filament on transport properties of V_Os in $Pt/TaO_x/Ta_2O_5/Pt$ cells are investigated with both experimental and theoretical approaches. As for the experimental approach, local Joule heating is observed on the surface of $Pt/TaO_x/Ta_2O_5/Pt$ cells during forming and RS operations. As for the theoretical approach, a coupled simulation of electric potential distribution, temperature distribution, and V_O concentration distribution during a reset process in $Pt/TaO_x/Ta_2O_5/Pt$ cells is performed.

In Chapter 6, the author summarizes this thesis and suggests the future outlooks.

References

[1] H. Akinaga, *Japanese Journal of Applied Physics* **52**, 100001 (2013).

[2] G. E. Moore, *Electronics* **38**, 114 (1965).

[3] Y. Fujisaki, *Japanese Journal of Applied Physics* **49**, 1000011 (2010).

[4] X. Dong, C. Xu, Y. Xie, and N. P. Jouppi, *IEEE Transactions on Computer-Aided Design of Integrated Circuits and Systems* **31**, 994 (2012).

[5] J. S. Meena, S. M. Sze, U. Chand, and T. Y. Tseng, *Nanoscale Research Letters* **9**, 1 (2014).

[6] H. S. Wong and S. Salahuddin, *Nature Nanotechnology* **10**, 191 (2015).

[7] T. Endoh, H. Koike, S. Ikeda, T. Hanyu, and H. Ohno, *IEEE Journal on Emerging and Selected Topics in Circuits and Systems* **6**, 109 (2016).

[8] R. E. Jones, P. D. Maniar, R. Moazzami, P. Zurcher, J. Z. Witowski, Y. T. Lii, P. Chu, and S. J. Gillespie, *Thin Solid Films* **270**, 584 (1995).

[9] T. Mikolajick, C. Dehm, W. Hartner, I. Kasko, M. J. Kastner, N. Nagel, M. Moert, and C. Mazure, *Microelectronics Reliability* **41**, 947 (2001).

[10] H. Kohlstedt, Y. Mustafa, A. Gerber, A. Petraru, M. Fitsilis, R. Meyer, U. Böttger, and R. Waser, *Microelectronic Engineering* **80**, 296 (2005).

[11] T. Mikolajick, U. Schroeder, and S. Slesazeck, *IEEE Transactions on Electron Devices* **67**, 1434 (2020).

[12] H. S. Wong, S. Raoux, S. Kim, J. Liang, J. P. Reifenberg, B. Rajendran, M. Asheghi, and K. E. Goodson, *Proceedings of the IEEE* **98**, 2201 (2010).

[13] R. E. Simpson, P. Fons, A. V. Kolobov, T. Fukaya, M. Krbal, T. Yagi, and J. Tominaga, *Nature Nanotechnology* **6**, 501 (2011).

[14] D. Loke, T. H. Lee, W. J. Wang, L. P. Shi, R. Zhao, Y. C. Yeo, T. C. Chong, and S. R. Elliott, *Science* **336**, 1566 (2012).

[15] T. Kishi, H. Yoda, T. Kai, T. Nagase, E. Kitagawa, M. Yoshikawa, K. Nishiyama, T. Daibou, M. Nagamine, M. Amano, S. Takahashi, M. Nakayama, N. Shimomura, H. Aikawa, S. Ikegawa, S. Yuasa, K. Yakushiji, H. Kubota, A. Fukushima, M. Oogane, T. Miyazaki, and K. Ando, *Technical Digest - International Electron Devices Meeting 2008 (San Francisco, 2008)*, p. 309.

[16] M. Gajek, J. J. Nowak, J. Z. Sun, P. L. Trouilloud, E. J. O'Sullivan, D. W. Abraham, M. C. Gaidis, G. Hu, S. Brown, Y. Zhu, R. P. Robertazzi, W. J. Gallagher, and D. C. Worledge, *Applied Physics Letters* **100**, 132408 (2012).

[17] A. V. Khvalkovskiy, D. Apalkov, S. Watts, R. Chepulskii, R. S. Beach, A. Ong, X. Tang, A. Driskill-Smith, W. H. Butler, P. B. Visscher, D. Lottis, E. Chen, V. Nikitin, and M. Krounbi, *Journal of Physics D: Applied Physics* **46**, 074001 (2013).

[18] D. Apalkov, B. Dieny, and J. M. Slaughter, *Proceedings of the IEEE* **104**, 1796 (2016).

[19] R. Waser and M. Aono, *Nature Materials* **6**, 833 (2007).

[20] A. Sawa, *Materials Today* **11**, 28 (2008).

[21] H. Akinaga and H. Shima, *Proceedings of the IEEE* **98**, 2237 (2010).

[22] H. S. P. Wong, H. Y. Lee, S. Yu, Y. S. Chen, Y. Wu, P. S. Chen, B. Lee, F. T. Chen, and M. J. Tsai, *Proceedings of the IEEE* **100**, 1951 (2012).

[23] J. J. Yang, D. B. Strukov, and D. R. Stewart, *Nature Nanotechnology* **8**, 13 (2013).

[24] F. Pan, S. Gao, C. Chen, C. Song, and F. Zeng, *Materials Science and Engineering R* **83**, 1 (2014).

[25] R. Waser, R. Dittmann, C. Staikov, and K. Szot, *Advanced Materials* **21**, 2632 (2009).

[26] D. Ielmini, *Semiconductor Science and Technology* **31**, 063002 (2016).

[27] *ISSCC 2022 Press Kit: Memory – 2022 Trends.*

[28] R. Waser, R. Dittmann, S. Menzel, and T. Noll, *Faraday Discussions* **213**, 11 (2019).

[29] S. Petzold, E. Miranda, S. U. Sharath, J. Muñoz-Gorriz, T. Vogel, E. Piros, N. Kaiser, R. Eilhardt, A. Zintler, L. Molina-Luna, J. Suñé, and L. Alff, *Journal of Applied Physics* **125**, 234503 (2019).

[30] E. Linn, R. Rosezin, C. Kügeler, and R. Waser, *Nature Materials* **9**, 403 (2010).

[31] Y. Yang, P. Sheridan, and W. Lu, *Applied Physics Letters* **100**, 203112 (2012).

[32] F. Nardi, S. Balatti, S. Larentis, D. C. Gilmer, and D. Ielmini, *IEEE Transactions on Electron Devices* **60**, 70 (2013).

[33] D. S. Jeong, H. Schroeder, and R. Waser, *Electrochemical and Solid-State Letters* **10**, G51 (2007).

[34] F. Nardi, S. Balatti, S. Larentis, and D. Ielmini, *Technical Digest - International Electron Devices Meeting 2011 (Washington DC, 2011)*, p. 709 (2011).

[35] I. Baek, M. Lee, S. Seo, M. Lee, D. Seo, D. Suh, J. Park, S. Park, H. Kim, I. Yoo, U. Chung, and J. Moon, *Technical Digest - International Electron Devices Meeting 2004 (San Francisco, 2004)*, p. 587 (2004).

[36] S. Seo, M. J. Lee, D. H. Seo, E. J. Jeoung, D. S. Suh, Y. S. Joung, I. K. Yoo, I. R. Hwang, S. H. Kim, I. S. Byun, J. S. Kim, J. S. Choi, and B. H. Park, *Applied Physics Letters* **85**, 5655 (2004).

[37] L. Goux, J. G. Lisoni, X. P. Wang, M. Jurczak, and D. J. Wouters, *IEEE Transactions on Electron Devices* **56**, 2363 (2009).

[38] T. Iwata, Y. Nishi, and T. Kimoto, *Japanese Journal of Applied Physics* **50**, 081102 (2011).

[39] T. Iwata, Y. Nishi, and T. Kimoto, *Japanese Journal of Applied Physics* **52**, 041801 (2013).

[40] H. Sasakura, Y. Nishi, and T. Kimoto, *Applied Physics Letters* **107**, 2 (2015).

[41] Y. Nishi and T. Kimoto, *Journal of Applied Physics* **120**, 115308 (2016).

[42] Y. Nishi, H. Sasakura, and T. Kimoto, *Journal of Materials Research* **32**, 2631 (2017).

[43] B. J. Choi, D. S. Jeong, S. K. Kim, C. Rohde, S. Choi, J. H. Oh, H. J. Kim, C. S. Hwang, K. Szot, R. Waser, B. Reichenberg, and S. Tiedke, *Journal of Applied Physics* **98**, 033715 (2005).

[44] J. P. Strachan, J. J. Yang, L. A. Montoro, C. A. Ospina, A. J. Ramirez, A. L. Kilcoyne, G. Medeiros-Ribeiro, and R. S. Williams, *Beilstein Journal of Nanotechnology* **4**, 467 (2013).

[45] M. Arahata, Y. Nishi, and T. Kimoto, *AIP Advances* **8**, 125010 (2018).

[46] U. Russo, D. Ielmini, C. Cagli, and A. L. Lacaita, *IEEE Transactions on Electron Devices* **56**, 186 (2009).

[47] D. Ielmini, R. Bruchhaus, and R. Waser, *Phase Transitions* **84**, 570 (2011).

[48] M. J. Lee, C. B. Lee, D. Lee, S. R. Lee, M. Chang, J. H. Hur, Y. B. Kim, C. J. Kim, D. H. Seo, S. Seo, U. I. Chung, I. K. Yoo, and K. Kim, *Nature Materials* **10**, 625 (2011).

[49] G. S. Park, Y. B. Kim, S. Y. Park, X. S. Li, S. Heo, M. J. Lee, M. Chang, J. H. Kwon, M. Kim, U. I. Chung, R. Dittmann, R. Waser, and K. Kim, *Nature Communications* **4**, 1 (2013).

[50] Y. S. Chen, H. Y. Lee, P. S. Chen, T. Y. Wu, C. C. Wang, P. J. Tzeng, F. Chen, M. J. Tsai, and C. Lien, *IEEE Electron Device Letters* **31**, 1473 (2010).

[51] B. Govoreanu, G. S. Kar, Y. Y. Chen, V. Paraschiv, S. Kubicek, A. Fantini, I. P. Radu, L. Goux, S. Clima, R. Degraeve, N. Jossart, O. Richard, T. Vandeweyer, K. Seo, P. Hendrickx, G. Pourtois, H. Bender, L. Altimime, D. J. Wouters, J. A. Kittl, and M. Jurczak, *Technical Digest - International Electron Devices Meeting 2008 (San Francisco, 2008)*, 729 (2011).

[52] F. Miao, J. P. Strachan, J. J. Yang, M. X. Zhang, I. Goldfarb, A. C. Torrezan, P. Eschbach, R. D. Kelley, G. Medeiros-Ribeiro, and R. S. Williams, *Advanced Materials* **23**, 5633 (2011).

[53] Z. Wei, T. Takagi, Y. Kanzawa, Y. Katoh, T. Ninomiya, K. Kawai, S. Muraoka, S. Mitani, K. Katayama, S. Fujii, R. Miyanaga, Y. Kawashima, T. Mikawa, K. Shimakawa, and K. Aono, *Technical Digest - International Electron Devices Meeting 2011 (Washington DC, 2011)*, 721 (2011).

[54] N. Kanegami, Y. Nishi, and T. Kimoto, *Applied Physics Letters* **116**, 013501 (2020).

[55] D.-j. Seong, M. Hassan, H. Choi, J. Lee, J. Yoon, J.-B. Park, W. Lee, M.-S. Oh, and H. Hwang, *IEEE Electron Device Letters* **30**, 919 (2009).

[56] Y. Watanabe, J. G. Bednorz, A. Bietsch, C. Gerber, D. Widmer, A. Beck, and S. J. Wind, *Applied Physics Letters* **78**, 3738 (2001).

[57] Z. L. Liao, Z. Z. Wang, Y. Meng, Z. Y. Liu, P. Gao, J. L. Gang, H. W. Zhao, X. J. Liang, X. D. Bai, and D. M. Chen, *Applied Physics Letters* **94**, 253503 (2009).

[58] T. Yamamoto, R. Yasuhara, I. Ohkubo, H. Kumigashira, and M. Oshima, *Journal of Applied Physics* **110**, 053707 (2011).

[59] V. V. Zhirnov, R. Meade, R. K. Cavin, and G. Sandhu, *Nanotechnology* **22**, 254027 (2011).

[60] A. C. Torrezan, J. P. Strachan, G. Medeiros-Ribeiro, and R. S. Williams, *Nanotechnology* **22**, 485203 (2011).

[61] D. B. Strukov and R. S. Williams, *Applied Physics A: Materials Science and Processing* **94**, 515 (2009).

[62] S. Menzel, M. Waters, A. Marchewka, U. Böttger, R. Dittmann, and R. Waser, *Advanced Functional Materials* **21**, 4487 (2011).

[63] Y. Lecun, Y. Bengio, and G. Hinton, *Nature* **521**, 436 (2015).

[64] W. Wang, G. Pedretti, V. Milo, R. Carboni, A. Calderoni, N. Ramaswamy, A. S. Spinelli, and D. Ielmini, *Science Advances* **4**, eaat4752 (2018).

[65] W. Zhang, B. Gao, J. Tang, X. Li, W. Wu, H. Qian, and H. Wu, *Physica Status Solidi - Rapid Research Letters* **13**, 1 (2019).

[66] G. W. Burr, R. M. Shelby, A. Sebastian, S. Kim, S. Kim, S. Sidler, K. Virwani, M. Ishii, P. Narayanan, A. Fumarola, L. L. Sanches, I. Boybat, M. Le Gallo, K. Moon, J. Woo, H. Hwang, and Y. Leblebici, *Advances in Physics: X* **2**, 89 (2017).

[67] R. B. Jacobs-Gedrim, S. Agarwal, R. S. Goeke, C. Smith, P. S. Finnegan, J. Niroula, D. R. Hughart, P. G. Kotula, C. D. James, and M. J. Marinella, *Journal of Applied Physics* **124**, 202101 (2018).

[68] S. H. Jo, T. Chang, I. Ebong, B. B. Bhadviya, P. Mazumder, and W. Lu, *Nano Letters* **10**, 1297 (2010).

[69] B. Rajendran and F. Alibart, *IEEE Journal on Emerging and Selected Topics in Circuits and Systems* **6**, 198 (2016).

[70] T. Hasegawa, K. Terabe, T. Tsuruoka, and M. Aono, *Advanced Materials* **24**, 252 (2012).

[71] D. Ielmini, *Microelectronic Engineering* **190**, 44 (2018).

[72] A. Wedig, M. Luebben, D. Y. Cho, M. Moors, K. Skaja, V. Rana, T. Hasegawa, K. K. Adepalli, B. Yildiz, R. Waser, and I. Valov, *Nature Nanotechnology* **11**, 67 (2016).

[73] P. Yao, H. Wu, B. Gao, S. B. Eryilmaz, X. Huang, W. Zhang, Q. Zhang, N. Deng, L. Shi, H. S. Wong, and H. Qian, *Nature Communications* **8**, 1 (2017).

[74] J. Tang, F. Yuan, X. Shen, Z. Wang, M. Rao, Y. He, Y. Sun, X. Li, W. Zhang, Y. Li, B. Gao, H. Qian, G. Bi, S. Song, J. J. Yang, and H. Wu, *Advanced Materials* **31**, 1902761 (2019).

[75] Z. Wang, M. Yin, T. Zhang, Y. Cai, Y. Wang, Y. Yang, and R. Huang, *Nanoscale* **8**, 14015 (2016).

[76] W. Kim, S. Menzel, D. J. Wouters, Y. Guo, J. Robertson, B. Roesgen, R. Waser, and V. Rana, *Nanoscale* **8**, 17774 (2016).

[77] A. Prakash, J. Park, J. Song, J. Woo, E. J. Cha, and H. Hwang, *IEEE Electron Device Letters* **36**, 32 (2015).

[78] S. Yu, *Proceedings of the IEEE* **106**, 260 (2018).

[79] Y. Nishi, H. Sasakura, and T. Kimoto, *Journal of Applied Physics* **124**, 152134 (2018).

[80] W. Wu, H. Wu, B. Gao, N. Deng, and H. Qian, *Journal of Applied Physics* **124**, 152108 (2018).

[81] T. Iwata, Y. Nishi, and T. Kimoto, *Thin Solid Films* **709**, 138203 (2020).

[82] S. Yu, Y. Wu, R. Jeyasingh, D. Kuzum, and H. S. Wong, *IEEE Transactions on Electron Devices* **58**, 2729 (2011).

[83] S. Ambrogio, S. Balatti, F. Nardi, S. Facchinetti, and D. Ielmini, *Nanotechnology* **24**, 384012 (2013).

[84] S. J. Li, B. Y. Dong, B. Wang, Y. Li, H. J. Sun, Y. H. He, N. Xu, and X. S. Miao, *IEEE Transactions on Electron Devices* **66**, 810 (2019).

[85] J. Chen, C. Y. Lin, Y. Li, C. Qin, K. Lu, J. M. Wang, C. K. Chen, Y. H. He, T. C. Chang, S. M. Sze, and X. S. Miao, *IEEE Electron Device Letters* **40**, 542 (2019).

Chapter 2

Deposition and Characterization of Tantalum-Oxide Films

2.1 Introduction

As described in Chapter 1, resistive switching (RS) characteristics in resistive random access memory (ReRAM) cells with a simple metal/metal-oxides/metal (MOM) stack structure vary depending on the materials of the top and bottom electrodes and the oxide layers. Not only that, properties such as crystallinity and oxygen composition of the oxides also have significant effects on RS characteristics. In this chapter, the deposition of tantalum (Ta) oxides by reactive sputtering was described by a simple theoretical model. Furthermore, properties such as oxygen composition, density, and crystallinity of Ta oxides deposited by reactive sputtering were investigated in detail.

2.2 Reactive radio frequency sputtering for tantalum oxide deposition

2.2.1 Sputtering system

The author used a sputtering system (EIKO: ES-250L) for the deposition of Ta oxides, as schematically shown in Fig. 2.1. The sputtering system can install up to 5 targets, which also act as cathodes on a sputtering gun. A substrate holder playing the role of the anode is located diagonally opposite from the sputtering gun to reduce sputtering damage to the substrates as much as possible. The substrate holder can be rotated for uniform deposition of oxides over the substrates in the plane. A shutter under the substrate enables a minimal change in the main chamber state from pre-deposition to deposition. Vacuum chambers are composed of a main sputtering chamber and a load-lock (LL) chamber with a transfer rod so that the substrate holder can be exchanged without exposing the main chamber to the air. The main chamber and the LL chamber are continuously evacuated by each turbo molecular

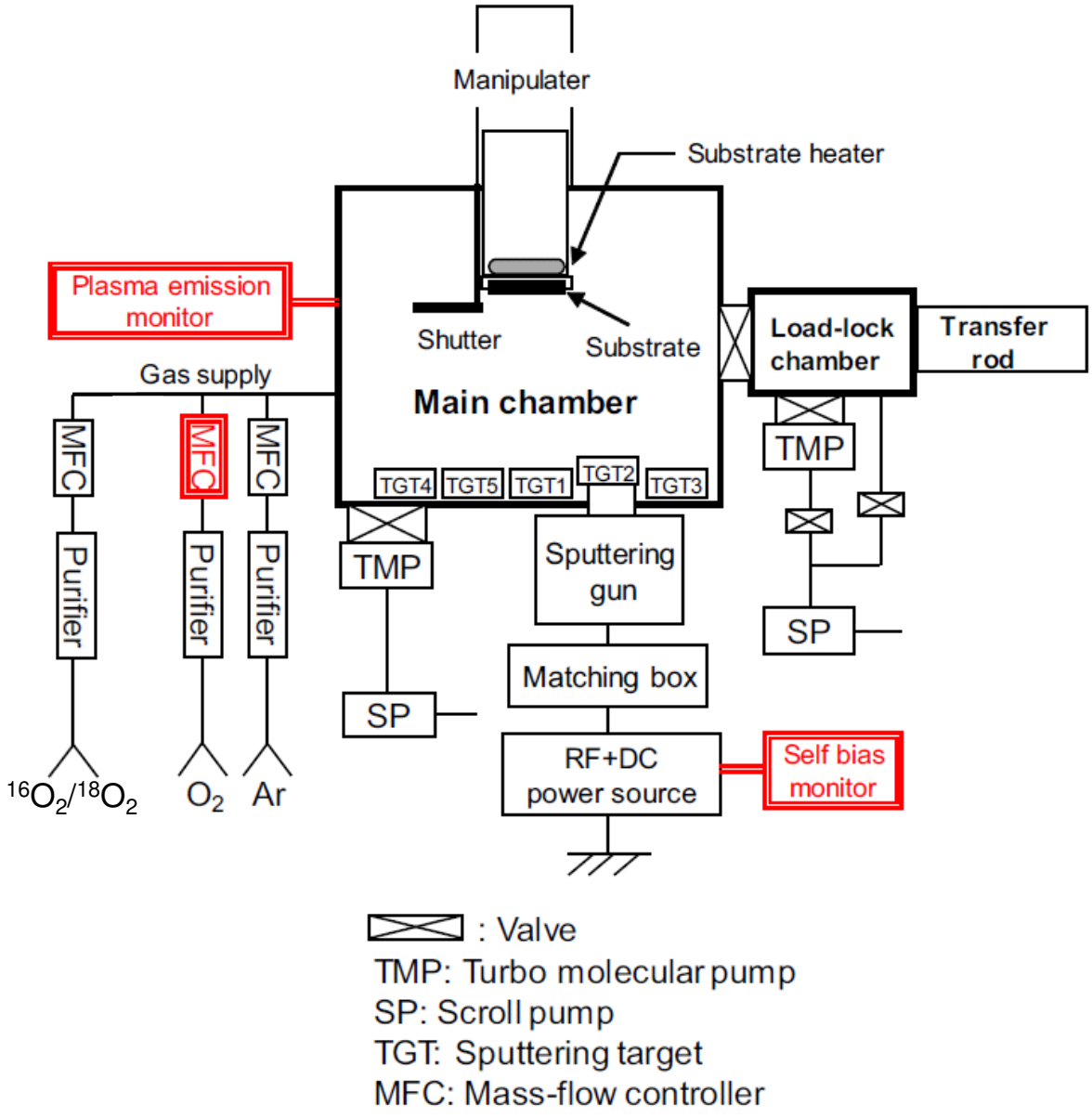

Figure 2.1: A schematic illustration of the sputtering system for deposition of tantalum oxides.

pump (TMP) with each auxiliary scroll pump (SP). The background pressure of the main chamber can be less than 2×10^{-5} Pa. Three kinds of gases, argon (Ar), oxygen (O_2), and high-purity isotopic oxygens ($^{18}O_2$ or $^{16}O_2$) can be introduced to the main chamber through each indispensable purifier with a flow rate controlled by each mass-flow controller (MFC). An RF power supply (frequency: 290 Hz) under the sputtering gun is mainly used for glow discharge. The stability of plasma emissions can be confirmed by a plasma emission monitor (PEM) during the pre-sputtering and sputtering. A logger software can monitor the self-bias voltage during the pre-sputtering and sputtering by DC voltage measuring equipment. In this study, two Ta targets with a purity of 99.999% were prepared, and a mixture of Ar and O_2 was used as a process gas. The Ar partial pressure was kept at 0.50 Pa.

2.2.2 Modeling of reactive sputtering

In this subsection, the dependences of deposition rate and oxygen composition in Ta oxide films on oxygen gas flow rates during reactive sputtering were analyzed based on Berg's model [1, 2]. The details of the model are described in Appendix A.

Figure 2.2 shows the relationship between the O_2 partial pressure in the main chamber and the oxygen gas flow rate. The parameters required for the calculation according to Berg's model were determined based on the experimental values in Fig. 2.2, as shown in Table 2.1. Similarly, Fig. 2.3 shows the relationship between the rate of Ta oxide deposition and the oxygen gas flow rate. The experimental values are roughly consistent with the calculated values by Berg's model in Fig. 2.2 and Fig. 2.3, indicating that the reactive sputtering of Ta oxide in this study can be explained using Berg's model. In the range of oxygen gas flow rates up to 1.4 sccm, the oxygen partial pressure is constant at zero. In this sputtering mode, which is called a metal mode because the surface of the target is metallic, all introduced oxygen is consumed by the oxidation reaction on the substrate. In contrast, at oxygen gas flow rates above 1.6 sccm, the oxygen partial pressure increases with the oxygen gas flow rate. This sputtering mode is called the oxide mode because the surface of the target is oxide. The range of the oxygen gas flow rate from 1.4 sccm to 1.6 sccm is called the transition mode. Since various conditions are unstable in the transition mode, oxides are generally deposited in the metal mode or the oxide mode. Thus, in reactive sputtering, there are two deposition modes based on the target surface. The deposition rate decreases at the transition from the metal mode to the oxide mode because the sputtering rate drastically decreases when the target surface changes from metal to oxide.

Moreover, the dependence of the oxygen composition ratio (O/Ta) in Ta oxides on the oxygen gas flow rate was calculated by Berg's model, as shown in Fig. 2.4. In the metal mode, the oxygen composition is proportional to the oxygen gas flow rate, while the oxygen composition is constant at 2.5, which is a value of the oxygen composition in the stoichiometric Ta oxide, in the oxide mode. Later in Section 2.3, the author experimentally characterized the oxygen composition of the Ta oxide film to investigate the controllability

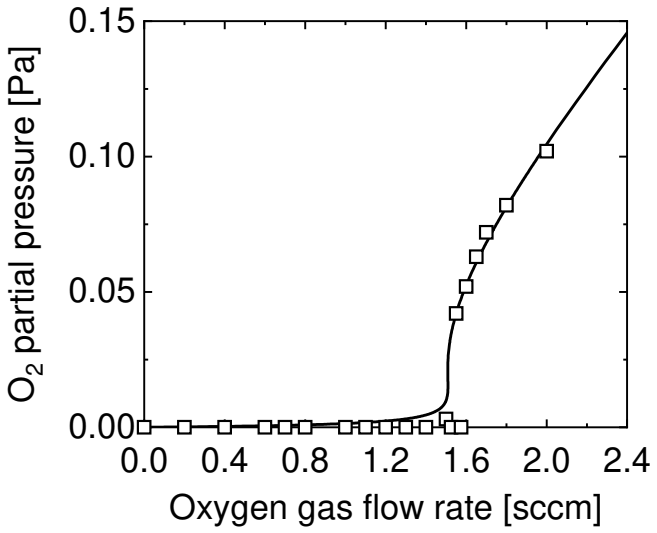

Figure 2.2: The relationship between the O_2 partial pressure in the main chamber and the oxygen gas flow rate during Ta oxide sputtering.

Table 2.1: Values of parameters used in a calculation according to Berg's model.

target size A_t	4.7 cm^2
collector size A_c	900 cm^2
sticking coefficient for target α_t	0.3
sticking coefficient for collector α_c	0.3
sputtering yield of compound Y_c	0.03
sputtering yield of metal Y_m	0.15
exhausting speed S	0.022 m^3/s
ion current density J	0.072 A/cm^2

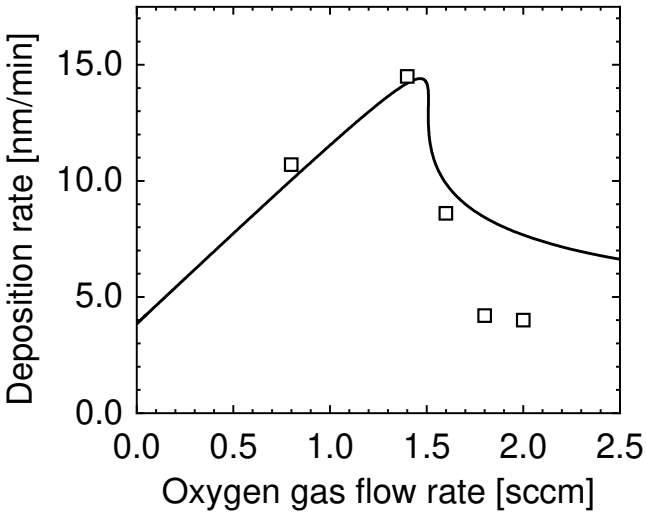

Figure 2.3: The relationship between the rate of Ta oxide deposition and the oxygen gas flow rate during Ta oxide sputtering.

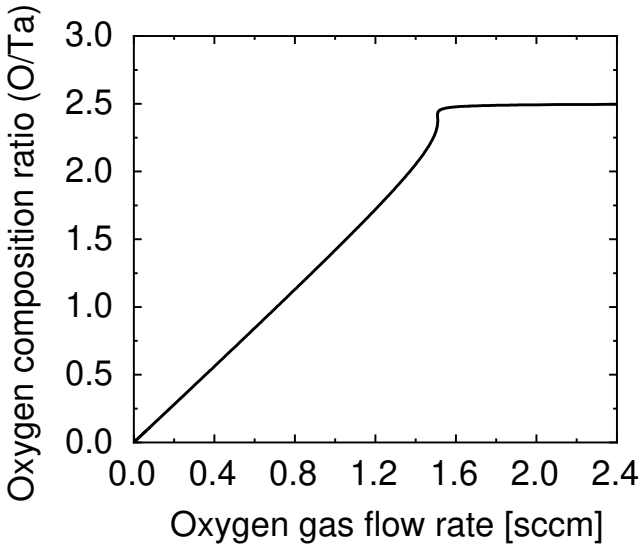

Figure 2.4: Dependence of the oxygen composition ratio (O/Ta) in Ta oxides on the oxygen gas flow rate during Ta oxide sputtering.

of the oxygen composition ratio by the oxygen gas flow rate during sputtering.

2.2.3 Fabrication processes of tantalum-oxide-based resistive switching cells

In this section, the main RS cell structures and the fabrication processes in this thesis were described in detail. The author fabricated RS cells with a structure of Ta oxide layers sandwiched between Pt top and bottom electrodes (Pt/Ta-oxides/Pt). Platinum is the most frequently adopted as an inert electrode [3–9]. First, a Pt layer was deposited by DC sputtering as a bottom electrode (BE) on a SiO_2/Si substrate. Second, Ta oxide layers were deposited by reactive radio-frequency (RF) sputtering at room temperature, as described in Sections 2.2.2 and 2.2.3. Finally, Pt top electrodes (TEs) with a diameter of 100–500 μm were deposited by electron-beam evaporation. The fabricated RS cells can be classified into two types by the structure of the Ta oxide layer: one with a single of TaO_y deposited in the oxide mode, and the other with a bilayer of TaO_x/TaO_y, where the TaO_x and TaO_y layers were deposited without exposing to the atmosphere in the metal and oxide mode, respectively. Figure 2.5 shows schematic illustrations of these cell structures. Here, the electrical potential spread is negligible because the scales in the film thickness direction and perpendicular to the film thickness direction are about 10^4 times different. Therefore, the size of such capacitor-type RS cells is determined by the area of the Pt TEs. As a more detailed reference, the author simulated the distributions of electric potential and electric field in Pt/TaO_x/Ta_2O_5/Pt cells in Appendix B.

2.3 Characterization of tantalum-oxide films

In this section, the author experimentally characterized properties such as oxygen composition, density, and crystallinity of Ta oxides deposited using the reactive sputtering system described above.

2.3.1 Crystallinity of tantalum-oxide films

Two samples with a 50-nm-thick Ta oxide film deposited on a Pt(60 nm)/SiO_2/Si substrates at oxygen gas flow rates of 0.8 sccm (metal mode) or 2.0 sccm (oxide mode) were prepared. The crystallinity of the Ta oxide layer in these samples was characterized by X-ray diffraction, cross-sectional transmission electron microscopy (TEM), and electron diffraction.

X-ray diffraction

The crystalline structure of Pt is a face-centered cubic (fcc) with a lattice constant of 3.923 Å. Previous studies revealed that Pt thin films deposited by DC sputtering exhibit columnar polycrystalline structures oriented to the [111] direction [10, 11]. To reduce the

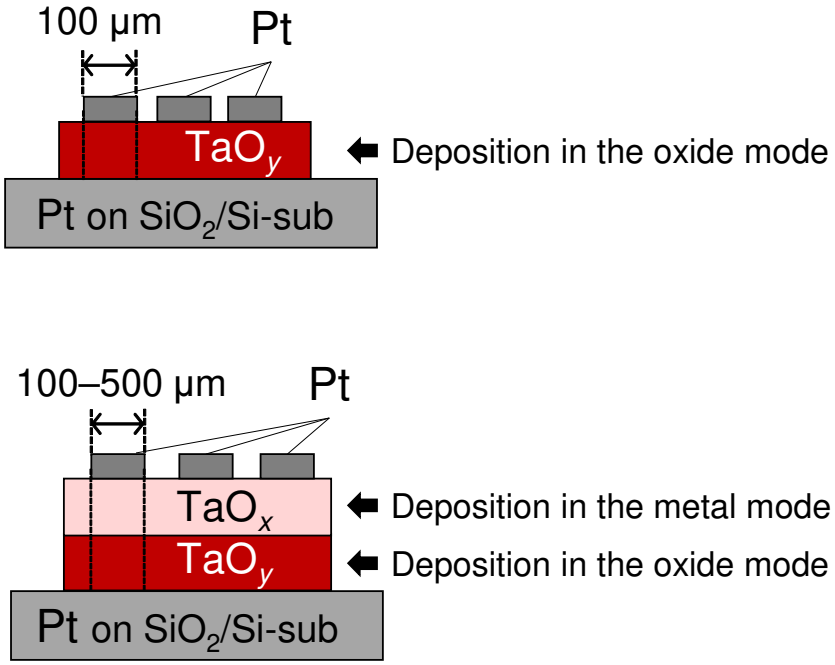

Figure 2.5: Schematic illustrations of the main RS cell structure fabricated in this thesis.

peak intensity derived from the crystalline structure of the Pt BE, in-plane X-ray diffraction measurements, which can characterize lattice planes perpendicular to the surface of a thin film, were performed by irradiating both samples with X-ray at a small incident angle of 0.1° for the sample surface. Figure 2.6 shows XRD curves in the cases where the oxygen gas flow rates during Ta oxide deposition are 0.8 sccm (metal mode) and 2.0 sccm (oxide mode). The narrow peak at a diffraction angle of 67° originates from a Pt(220) plane. Other broad peaks could be derived from the Ta oxide films, suggesting that the Ta oxide films deposited in this study are microcrystalline close to amorphous. While the broad peak at about 35 degrees in the case of 0.8 sccm is difficult to identify, the broad peaks in the case of 2.0 sccm may originate from orthorhombic Ta_2O_5 because the peak diffraction angle obtained in this study is similar to that obtained in powder samples of orthorhombic Ta_2O_5.

Cross-sectional transmission electron microscopy

Cross-sectional TEM observations were also performed on the samples used for XRD measurements. Figure 2.7 shows cross-sectional TEM images of the prepared samples in the cases where the oxygen gas flow rates during Ta oxide deposition are 0.8 sccm (metal mode) and 2.0 sccm (oxide mode). As reported in previous studies [10, 11], Pt BE layers exhibit a columnar polycrystalline structure with a grain diameter of tens of nanometers. In contrast, there is no significant difference in brightness in the Ta oxide film in the case of 2.0 sccm, indicating that the Ta oxide film is almost homogeneous and amorphous. There is a little difference in brightness on different regions in the Ta oxide film in the case of 0.8 sccm.

Electron diffraction

Irradiating the region presented by white dashed lines in Fig. 2.7 with an electron beam, the crystalline structures of the Ta oxide films were examined from the diffraction patterns, as shown in Fig. 2.8. Two electron diffraction patterns in the case of 0.8 sccm were almost identical and consisted of broad concentric rings, indicating that the Ta oxide film is almost homogeneous and amorphous also in the case of 0.8 sccm. Moreover, comparing the electron diffraction patterns in the cases of 0.8 sccm and 2.0 sccm, the radius of the concentric rings is larger in the case of 0.8 sccm than in the case of 2.0 sccm. Since the radius of the concentric rings in the electron diffraction pattern corresponds to the distance between lattice planes in reciprocal lattice space, the distance between lattice planes in real space is smaller for microcrystal grains of Ta oxide in the case of 0.8 sccm than in the case of 2.0 sccm.

2.3.2 Chemical composition of tantalum-oxide films

Ta oxide films with a thickness of more than 200 nm were deposited by reactive sputtering on Pt(60 nm)/SiO_2/Si substrates at various oxygen gas flow rates. The chemical compositions of these Ta oxide films were characterized by Rutherford back-scattering spectrometry

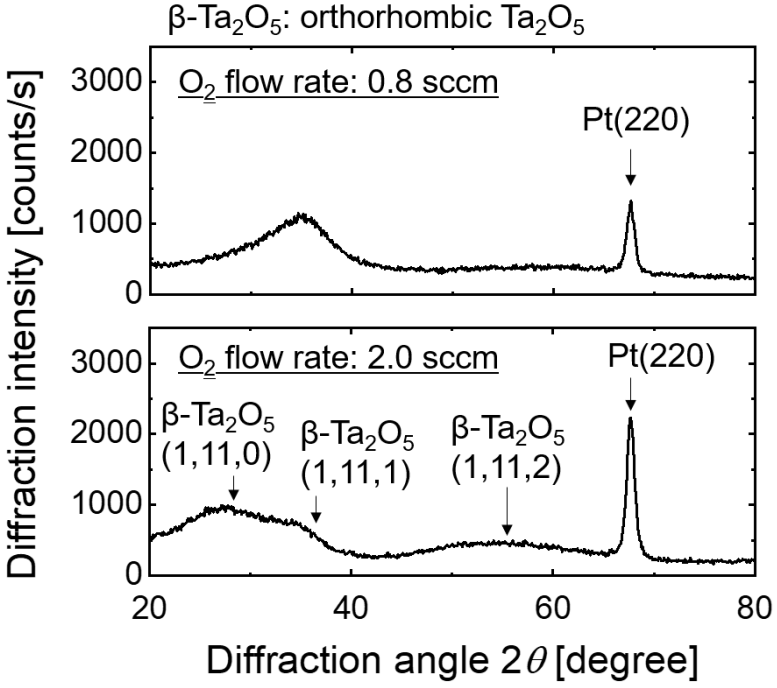

Figure 2.6: X-ray diffraction (XRD) curves in cases that the oxygen gas flow rates during Ta oxide deposition are 0.8 sccm (metal mode) and 2.0 sccm (oxide mode).

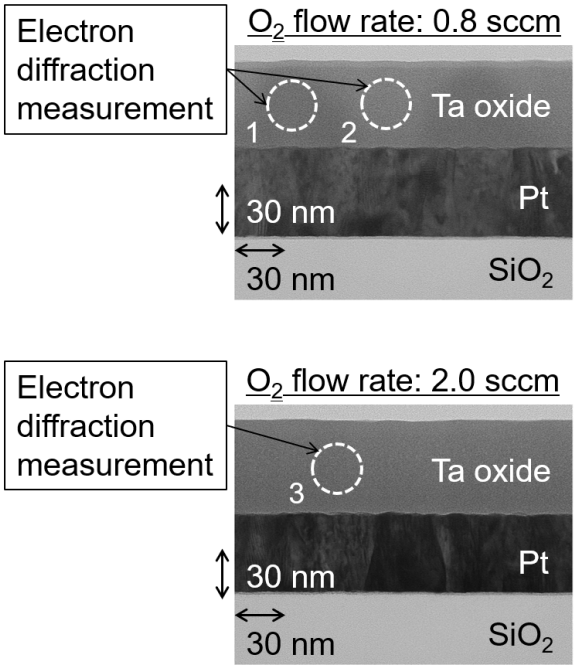

Figure 2.7: Cross-sectional TEM images of the prepared samples in the cases that the oxygen gas flow rates during Ta oxide deposition are 0.8 sccm (metal mode) and 2.0 sccm (oxide mode). White dashed lines show the region irradiated with an electron beam in electron diffraction measurement.

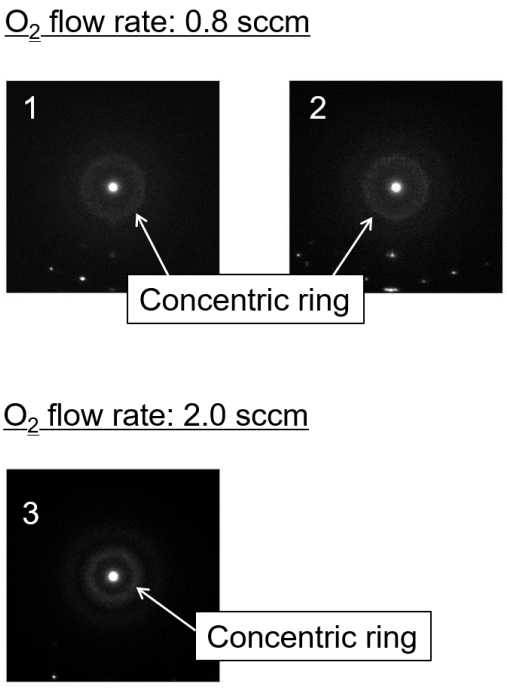

Figure 2.8: Electron diffraction patterns obtained by irradiating the region presented by white dashed lines in the cross-sectional TEM images with an electron beam.

(RBS). Figure 2.9 shows experimental values obtained by RBS and theoretical values calculated by Berg's model for the dependence of composition ratios of O and Ar to Ta on oxygen gas flow rates during the Ta oxide deposition. Both the experimental and theoretical values show a similar tendency that the oxygen composition ratio is proportional to the oxygen gas flow rate in the metal mode and is roughly constant at 2.5 (stoichiometric Ta oxide) in the oxide mode. These results revealed that the oxygen composition of the deposited Ta oxide film can be controlled by the oxygen gas flow rate during the Ta oxide deposition.

Next, the composition ratio of Ar increase with the oxygen gas flow rate. Since Ar is used as the carrier gas for the glow discharge in reactive sputtering, contamination of the Ta oxide films caused by Ar atoms/ions recoiling when argon ions hit the target surface is inevitable. The energy of the recoiled Ar atoms/ions is considered to depend on the atomic weight or molecular weight of the target surface material to be sputtered.Even though the Ar partial pressure is constant, the energy of recoil Ar is larger in the oxide mode, where the target surface is oxide, than in the metal mode. Therefore, as the oxygen gas flow rate during the Ta oxide deposition increases, the energy of recoil Ar increases and so the amount of Ar contamination in the Ta oxide films also increases, as shown in Fig. 2.9. Although Ar atoms are considered to be electrically inert in the Ta oxide films, large amounts of Ar contamination could affect the internal stress of the thin film. Here, the XRD results for the Ta oxide with higher Ar contamination in the case of the oxygen gas flow rate of 2.0 sccm, as shown in Fig. 2.6, show that the peak diffraction angles are slightly shifted from that obtained in powder samples of orthorhombic Ta_2O_5 to the lower angle. From Bragg's law of diffraction, a shift of the diffraction angle to a lower angle means applying tensile stress to the Ta oxide films in in-plane XRD measurement. However, any problems such as peeling or cracking didn't occur in the Ta oxide films deposited in this study, indicating that the effect of the tensile stress is considered to be sufficiently small. From the above, the impact of the Ar contamination was ignored in the following Chapters.

In addition, the author also examined the controllability of oxygen composition in TaO_x/TaO_y/Pt stacking samples as shown in Fig. 2.5. Compositional distribution in the thickness direction was investigated by high-resolution RBS for the TaO_x/TaO_y/Pt samples, where a 6-nm-thick TaO_y layer and a 12-nm-thick TaO_x layer were deposited on a Pt(5 nm)/SiO_2/Si substrate at oxygen gas flow rates of 2.0 sccm (oxide mode) and 0.8 sccm (metal mode), respectively, without exposure to the air. Here, in the high-resolution RBS, the energy resolution can be improved by using a deflection-magnetic-field-type energy analyzer, not the conventional semiconductor detector, enabling characterization of the composition distribution of ultrathin films in the thickness direction. Figure 2.10 shows the compositional distribution obtained by the high-resolution RBS. The oxygen composition ratios of the TaO_x and TaO_y layers were 1.5 and 2.5, respectively. Moreover, the high-resolution RBS was performed for two TaO_x(12 nm)/TaO_y(6 nm)/Pt samples with the TaO_x layers deposited at different oxygen gas flow rates of 1.0 sccm and 1.2 sccm. In both samples, the TaO_y layers were deposited at the oxygen gas flow rate of 2.0 sccm.

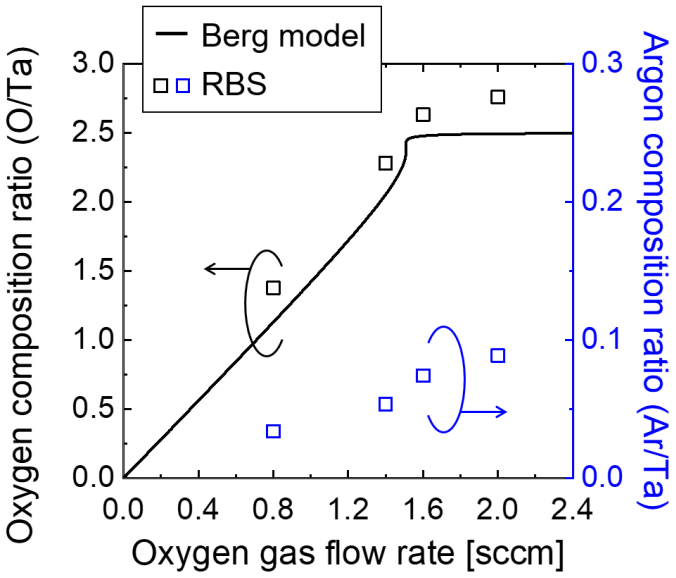

Figure 2.9: Experimental values obtained by RBS and theoretical values calculated by Berg's model for dependence of composition ratios of O and Ar to Ta on oxygen gas flow rates during the Ta oxide deposition.

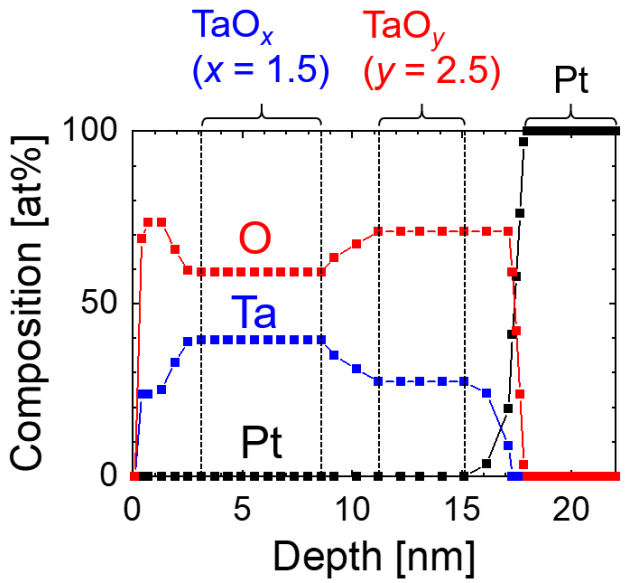

Figure 2.10: Compositional distribution in the thickness direction by high-resolution RBS for the $TaO_x/TaO_y/Pt$ samples, where a 6-nm-thick TaO_y layer and a 12-nm-thick TaO_x layer were deposited at oxygen flow rates of 2.0 sccm (oxide mode) and 0.8 sccm (metal mode), respectively, without exposure to the air.

Therefore, the oxygen composition ratio of the TaO_y layer is 2.5, which is the value of the stoichiometric Ta_2O_5. Figure 2.11 shows the dependence of the oxygen composition ratio in the TaO_x layer on the oxygen gas flow rates during the TaO_x deposition. The oxygen composition ratio in the TaO_x layer is proportional to the oxygen gas flow rate during the TaO_x deposition, which tends to be similar to the relationship calculated from Berg's model between the oxygen composition and the oxygen gas flow rate, as presented in Fig. 2.11. Thus, also in TaO_x/TaO_y/Pt stacking samples, the oxygen compositions of the deposited Ta oxide films can be precisely controlled by the oxygen gas flow rate during the Ta oxide deposition.

2.3.3 Discussion

In this section, the author discusses that consistent results have been obtained for the density of Ta oxide in various experimental characterizations and the calculation based on Berg's model. First, Fig. 2.12 shows experimental values obtained by RBS and theoretical values calculated by Berg's model for dependence of the density of the Ta oxide on the oxygen gas flow rates during the Ta oxide deposition. As well as the oxygen compositions in Fig. 2.9, both the experimental and theoretical values show a similar tendency that the density of the Ta oxide linearly decreases with an increase in the oxygen gas flow rate in the metal mode and saturates at 8.73 g/cm^3 (the density of stoichiometric Ta_2O_5) in the oxide mode. Reflecting the oxygen gas flow dependence of the density of the Ta oxide, as shown in Fig. 2.6, the peak intensities derived from the Pt(220) plane in the XRD curves differ significantly in the cases where the oxygen gas flow rates during the Ta oxide deposition are 0.8 sccm and 2.0 sccm. The Ta oxide deposited at the oxygen gas flow rate of 0.8 sccm has a higher density than 2.0 sccm, which results in a smaller penetration depth of X-ray and a smaller intensity of X-ray reaching the Pt bottom layer. Furthermore, from the electron diffraction patterns in Fig. 2.8, the distance between lattice planes in real space is smaller for microcrystal grains of the Ta oxide in the case of 0.8 sccm than in the case of 2.0 sccm, suggesting that the density is higher in the case of 0.8 sccm.

2.4 Summary

After the fabrication processes of resistive switching cells, especially the deposition of Ta oxide by reactive sputtering were described in detail, the author worked on modeling the reactive sputtering, based on experimental characterization of the deposited Ta oxide films. First, a simplified theoretical model (Berg's model) was used to calculate the relationship between the oxygen gas flow rate during deposition and the composition and density of the Ta oxide films. Second, the composition and density of Ta oxide films fabricated with different oxygen gas flow rates during deposition were evaluated by Rutherford backscattering spectroscopy. As a result, the experimental values were consistent with the calculated

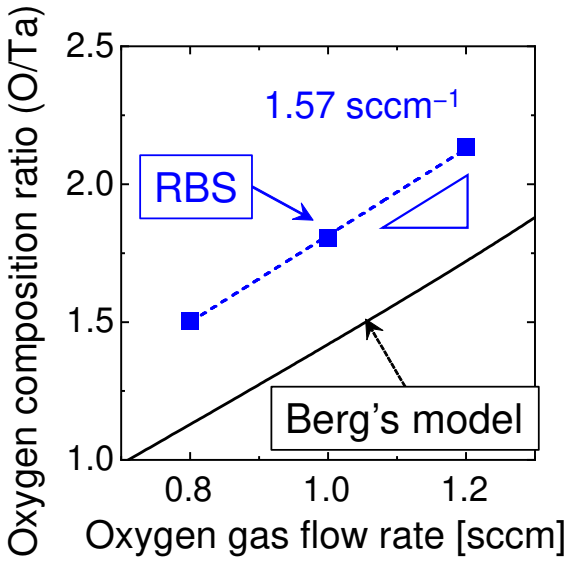

Figure 2.11: Dependence of the oxygen composition in the TaO_x layer on the oxygen gas flow rate during the TaO_x deposition.

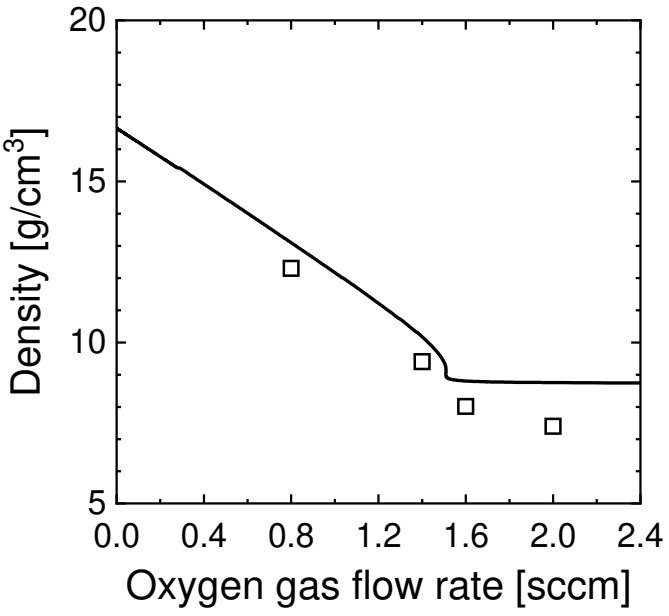

Figure 2.12: Experimental values obtained by RBS and theoretical values calculated by Berg's model for dependence of the density of the Ta oxide on the oxygen gas flow rates during the Ta oxide deposition.

values. Third, the results of X-ray diffraction, cross-sectional transmission electron microscopy, and electron diffraction revealed that the Ta oxide films are microcrystalline close to amorphous. Finally, the high-resolution RBS for the $TaO_x/TaO_y/Pt$ stacking samples, where the TaO_y and TaO_x layers were deposited at oxygen gas flow rates of 2.0 sccm (oxide mode) and 0.8–1.2 sccm (metal mode), respectively, revealed that the oxygen composition ratio in the TaO_x layer linearly increases from 1.51 to 2.13 with the oxygen gas flow rate during the TaO_x deposition and that the oxygen composition ratio of the TaO_y layer is 2.5 (stoichiometry). Based on these results, the oxygen composition of the Ta oxide deposited by reactive sputtering was precisely controlled by the oxygen gas flow rate.

References

[1] S. Berg, H. Blom, T. Larsson, and C. Nender, *Journal of Vacuum Science & Technology A: Vacuum, Surfaces, and Films* **5**, 202 (1987).

[2] S. Berg and T. Nyberg, *Thin Solid Films* **476**, 215 (2005).

[3] S. Seo, M. J. Lee, D. H. Seo, E. J. Jeoung, D.-S. Suh, Y. S. Joung, I. K. Yoo, I. R. Hwang, S. H. Kim, I. S. Byun, J.-S. Kim, J. S. Choi, and B. H. Park, *Applied Physics Letters* **85**, 5655 (2004).

[4] B. J. Choi, D. S. Jeong, S. K. Kim, C. Rohde, S. Choi, J. H. Oh, H. J. Kim, C. S. Hwang, K. Szot, R. Waser, B. Reichenberg, and S. Tiedke, *Journal of Applied Physics* **98**, 033715 (2005).

[5] H. Shima, F. Takano, H. Akinaga, Y. Tamai, I. H. Inoue, and H. Takagi, *Applied Physics Letters* **91**, 012901 (2007).

[6] J. J. Yang, M. D. Pickett, X. Li, D. A. Ohlberg, D. R. Stewart, and R. S. Williams, *Nature Nanotechnology* **3**, 429 (2008).

[7] W. Kim, S. Menzel, D. J. Wouters, Y. Guo, J. Robertson, B. Roesgen, R. Waser, and V. Rana, *Nanoscale* **8**, 17774 (2016).

[8] S. Petzold, E. Miranda, S. U. Sharath, J. Muñoz-Gorriz, T. Vogel, E. Piros, N. Kaiser, R. Eilhardt, A. Zintler, L. Molina-Luna, J. Suñé, and L. Alff, *Journal of Applied Physics* **125**, 234503 (2019).

[9] P. Y. Wu, T. C. Chang, M. C. Chen, C. C. Yang, H. X. Zheng, P. H. Chen, W. C. Chen, Y. C. Zhang, S. K. Lin, J. J. Chen, H. C. Huang, T. M. Tsai, and S. M. Sze, *IEEE Transactions on Electron Devices* **68**, 541 (2021).

[10] Y. Nishi and T. Kimoto, *Journal of Applied Physics* **120**, 115308 (2016).

[11] T. Iwata, Y. Nishi, and T. Kimoto, *Thin Solid Films* **709**, 138203 (2020).

Chapter 3

Impacts of Introducing a Ta-rich TaO_x Layer on Initial Characteristics in Pt/Ta_2O_5/Pt Cells

3.1 Introduction

Previous studies have reported that stacking metal-rich oxide and stoichiometric oxide as the oxide layer of resistive switching (RS) cells improves some performances, such as endurance and retention [1–6]. Although the metal-rich layer is considered to act as an oxygen-vacancy-reservoir that supplies oxygen vacancies (V_O) to the stoichiometric oxide layer when a voltage is applied [7, 8], the physical effects of stacking metal-rich layers have not been completely clarified because experimental observation of V_O transport in an ultra-thin oxide film (a thickness of several tens of nanometers) and in a localized region (a diameter of several nanometers) in which the growth and dissolution of a conductive filament (CF) occur is difficult. In this chapter, the effect of stacking a TaO_x layer on a Ta_2O_5 layer was investigated, focusing on the electrical characteristics in the initial state.

3.2 Experimental methods

RS cells with two types of stacking structures, Pt/Ta_2O_5/Pt/Ti and Pt/TaO_x/Ta_2O_5/Pt, were fabricated on SiO_2/Si substrates, as shown in Fig. 3.1. The 60-nm-thick Pt and 5-nm-thick Ti layers as a bottom electrode (BE) and an adhesion layer were deposited by DC sputtering, respectively. Note that the presence or absence of the Ti adhesion layer has little effect on electrical characteristics.TaO_x and Ta_2O_5 layers with various thicknesses were deposited by reactive radio-frequency sputtering. The oxygen gas flow rate during the Ta_2O_5 deposition was adjusted to 1.7 sccm and 2.0 sccm, which are the conditions of the oxide mode in the reactive sputtering of Ta from the results in Chap. 2 On the other hand, the oxygen gas flow rate during the TaO_x deposition was adjusted between 0.8 sccm and 1.2

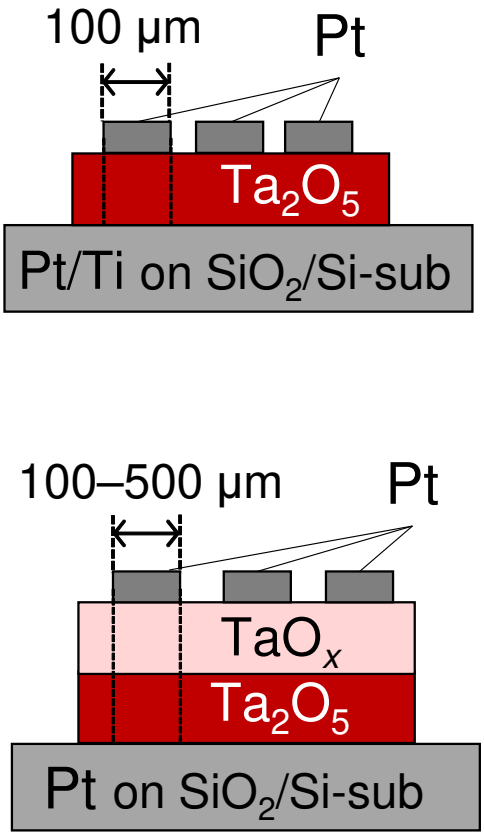

Figure 3.1: Two types of stacking structures of the fabricated RS cells. The size of such capacitor-type RS cells is determined by the area of the Pt top electrode (TE).

sccm, which are the conditions of the metal mode. The oxygen composition x in the TaO_x layer was controlled by adjusting the oxygen gas flow rate, as shown in Fig. 2.11 in Chap. 2. As top electrodes (TEs), a 25-nm-thick Pt layer was formed by electron beam evaporation. The diameters of TEs ranged from 100 to 500 μm. The size of such capacitor-type RS cells is determined by the area of the Pt TEs, as discussed in Chap. 2 and Appendix B. Table 3.1, Table 3.2, and Table 3.3 show sample names and the corresponding conditions, such as thickness and oxygen composition of the Ta_2O_5 and/or TaO_x layers, for samples of S1–S4, D1–D3, and E1–E5.

DC and/or AC characteristics of the samples listed in Table 3.2 and Table 3.3 were measured. In the DC measurements, initial electrical characteristics were investigated for all samples. Moreover, temperature dependence of DC conductance in an initial state ($G_{\rm ini}$) at 0.1 V was evaluated from 80 to 380 K for the samples of D1–D3 and E1–E3. During the AC measurements, frequency-dependent AC admittance was assessed at zero bias with a voltage amplitude of 300 mV from 40 Hz to 1 MHz by using an HP 4294A impedance analyzer in the temperature range of 189–300 K. In a parallel circuit model, AC admittance Y can be expressed by $Y = G_{\rm tot} + j\omega C$, where $G_{\rm tot}$, C, and ω are a real part of the admittance corresponding to the conductance, capacitance, and angular frequency, respectively. During these measurements, BEs were grounded.

3.3 Initial electrical characteristics

3.3.1 $Pt/Ta_2O_5/Pt$ cells

Figure 3.2 shows current–voltage (I–V) and resistance–voltage (R–V) characteristics in the initial state of Pt/Ta_2O_5(5 nm)/Pt cells (sample S1) when the oxygen gas flow rate during Ta_2O_5 deposition is 2.0 sccm. $Pt/Ta_2O_5/Pt$ cells exhibited a large device to device variation. Figure 3.3 shows the relationship between forming voltage ($V_{\rm form}$) and initial resistance ($R_{\rm ini}$) in $Pt/Ta_2O_5/Pt$ cells (sample S1–S4) when the oxygen gas flow rate during Ta_2O_5 deposition is 2.0 sccm. The values of $V_{\rm form}$ decrease to about 2.5 V when the Ta_2O_5 thickness decreases, and the variation in $V_{\rm form}$ also decreases when the Ta_2O_5 thickness decreases. On the other hand, $R_{\rm ini}$ is about 10^{11} Ω in most Pt/Ta_2O_5(25 nm)/Pt cells (sample S4). When the Ta_2O_5 thickness increases, some $Pt/Ta_2O_5/Pt$ cells exhibit lower $R_{\rm ini}$ down to 10^6 Ω.

Next, Fig. 3.4 shows the normalized frequency of initial resistance in Pt/Ta_2O_5(10 nm)/Pt cells when the Ta_2O_5 layer was deposited at oxygen gas flow rates of 1.7 sccm (sample S2-2) and 2.0 sccm (sample S2). The variation in initial resistance in $Pt/Ta_2O_5/Pt$ cells decreases when the oxygen gas flow rate during the Ta_2O_5 deposition increases. The oxygen gas flow rate of 2.0 sccm, at which the variation in $R_{\rm ini}$ is relatively small, was used for the fabrication of $Pt/TaO_x/Ta_2O_5/Pt$ cells.

Table 3.1: Thickness and oxygen gas flow rate during the Ta_2O_5 deposition for samples of S1–S4 with the structure of Pt/Ta_2O_5/Pt.

Sample name	S1	S2	S2-2	S3	S4
Ta_2O_5 thickness	5 nm	10 nm	10 nm	15 nm	25 nm
Oxygen gas flow rate	2.0 sccm	2.0 sccm	1.7 sccm	2.0 sccm	2.0 sccm

Table 3.2: Thickness of the oxide layers for samples of D1, D2, and D3 in case that the oxygen composition of the TaO_x layer is 1.5.

Sample name	D1	D2	D3
Ta_2O_5	5 nm	10 nm	5 nm
$TaO_{1.5}$	5 nm	10 nm	10 nm

Table 3.3: The oxygen composition of the TaO_x layer for samples of E1–E5 with the structure of Pt/TaO_x/Ta_2O_5/Pt.

Ta_2O_5: 10 nm, TaO_x: 25 nm					
Sample name	E1	E2	E3	E4	E5
Oxygen composition x in TaO_x	1.51	1.66	1.81	1.97	2.13

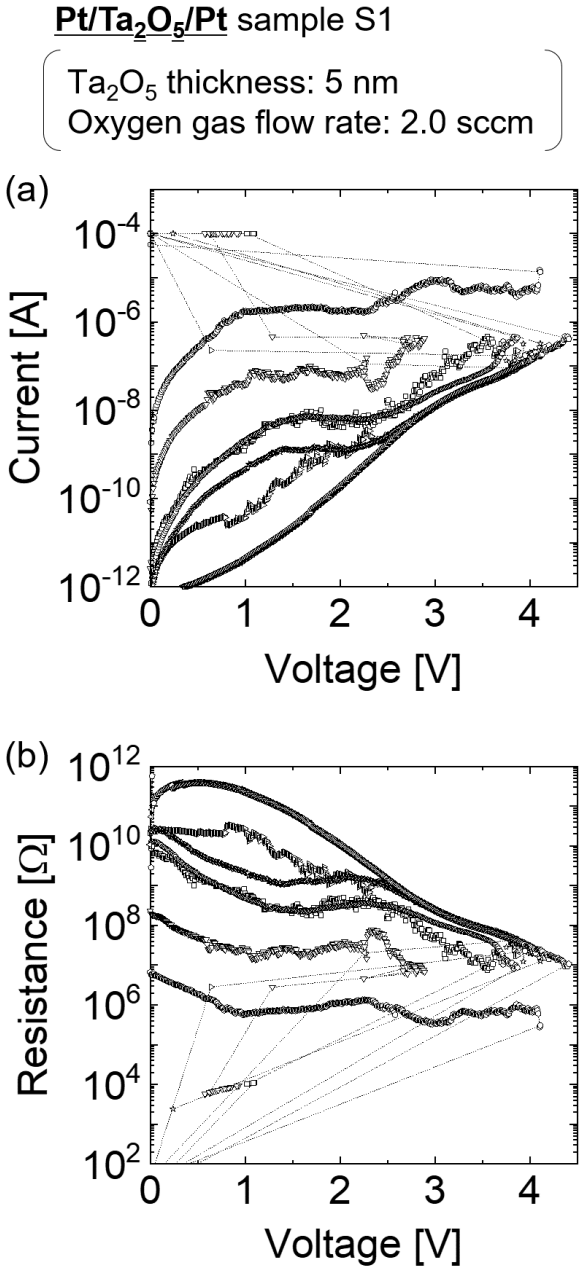

Figure 3.2: Current-voltage and resistance-voltage characteristics in an initial state of Pt/Ta_2O_5(5 nm)/Pt cells (sample S1) when oxygen gas flow rate during Ta_2O_5 deposition is 2.0 sccm.

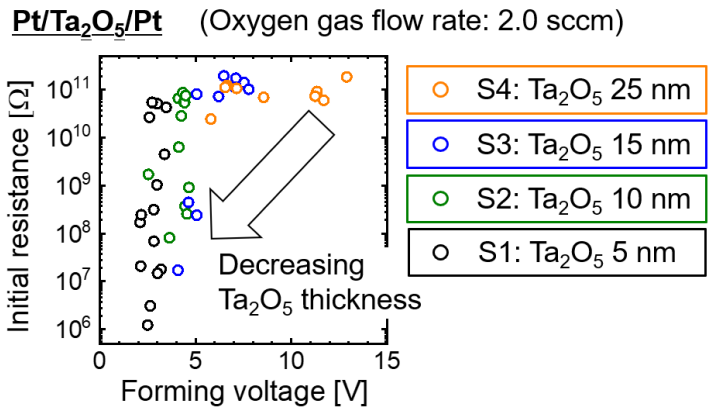

Figure 3.3: The relationship between initial resistance and forming voltage in $Pt/Ta_2O_5/Pt$ cells with various Ta_2O_5 thickness (sample S1–S4) when oxygen gas flow rate during Ta_2O_5 deposition is 2.0 sccm.

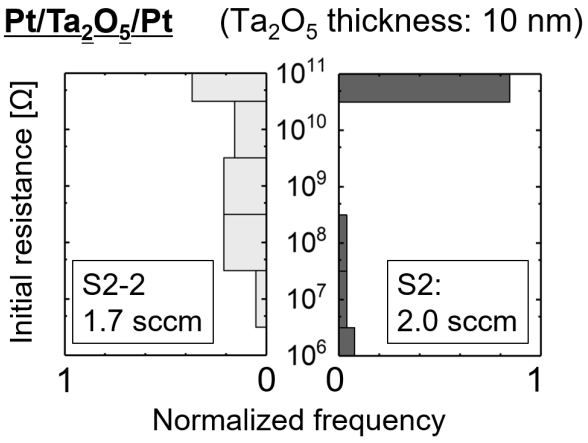

Figure 3.4: Normalized frequency of initial resistance in Pt/Ta_2O_5(10 nm)/Pt cells when the Ta_2O_5 layer was deposited at oxygen gas flow rates of 1.7 sccm (sample S2-2) and 2.0 sccm (sample S2).

3.3.2 Pt/TaO$_x$/Ta$_2$O$_5$/Pt cells

Figure 3.5 shows I–V and R–V characteristics in the initial state of Pt/Ta$_2$O$_5$(5 nm)/Pt cells (sample S1) and Pt/TaO$_x$(5 nm)/Ta$_2$O$_5$(5 nm)/Pt cells (sample D1). Although Pt/Ta$_2$O$_5$/Pt cells exhibited a large variation in the I–V characteristics as mentioned in Sec. 3.3.1, the variation in I–V characteristics drastically decreases in Pt/TaO$_x$/Ta$_2$O$_5$/Pt cells. Moreover, R_{ini} in Pt/TaO$_x$/Ta$_2$O$_5$/Pt cells was lower than that in Pt/Ta$_2$O$_5$/Pt cells and constant up to about 3 V for the applied voltage.

Figure 3.6 shows I–V characteristics in the initial state of Pt/TaO$_x$(25 nm)/Ta$_2$O$_5$(10 nm)/Pt cells with various oxygen compositions x (sample E1, E3, and E5). In all samples, the cell resistance is constant for the applied voltage up to about 4V. Figure 3.7 shows dependence of the cell resistance constant for the applied voltage (R_{ini}) on the oxygen composition of the TaO$_x$ layer in Pt/TaO$_x$(25 nm)/Ta$_2$O$_5$(10 nm)/Pt cells (sample E1–E5). Here, the oxygen composition on the upper axis was converted using the relationship between oxygen gas flow rate and oxygen composition obtained from the results of high-resolution Rutherford back-scattering spectrometry (HRRBS). As the oxygen composition in the TaO$_x$ layer increases, R_{ini} increases exponentially from about 3 kΩ to about 1 GΩ.

3.3.3 Discussion

The variation in V_{form} of Pt/Ta$_2$O$_5$/Pt cells reflects that in the intensity of forming electric field (E_{form}) translated by the Ta$_2$O$_5$ thickness. Figure 3.8 shows the dependence of V_{form} and E_{form} on the Ta$_2$O$_5$ thickness, indicating that E_{form} tends to increase with the Ta$_2$O$_5$ thickness and that the variation in E_{form} is independent of the Ta$_2$O$_5$ thickness. The variation in R_{ini} of Pt/Ta$_2$O$_5$/Pt cells in Fig. 3.4 could be attributed to the increase in V$_{\mathrm{O}}$s in the Ta$_2$O$_5$ layer due to the decrease in the oxygen gas flow rate during the Ta$_2$O$_5$ deposition in Pt/Ta$_2$O$_5$/Pt cells. The increase in V$_{\mathrm{O}}$s facilitates the presence of conductive paths connecting the top and bottom electrodes. As a result, some Pt/Ta$_2$O$_5$/Pt cells are more likely to exhibit small R_{ini}. Similarly, the Ta$_2$O$_5$ thickness dependence of the variation in R_{ini} in Fig. 3.3 suggests that the conductive paths originating from V$_{\mathrm{O}}$s are more likely to connect the top and bottom electrodes when the Ta$_2$O$_5$ thickness is thinner.

In the following sections, the author investigated the impacts of introducing the TaO$_x$ layer, focusing on the Pt/TaO$_x$/Ta$_2$O$_5$/Pt cells, where the variation in I–V characteristics is significantly reduced.

3.4 Temperature dependence of initial conductance in Pt/TaO$_x$/Ta$_2$O$_5$/Pt cells

In TaO$_x$-based RS cells, various conduction mechanisms of CFs were proposed for each resistance state, such as nearest neighbor hopping (NNH) [4, 9], Mott's variable range hopping

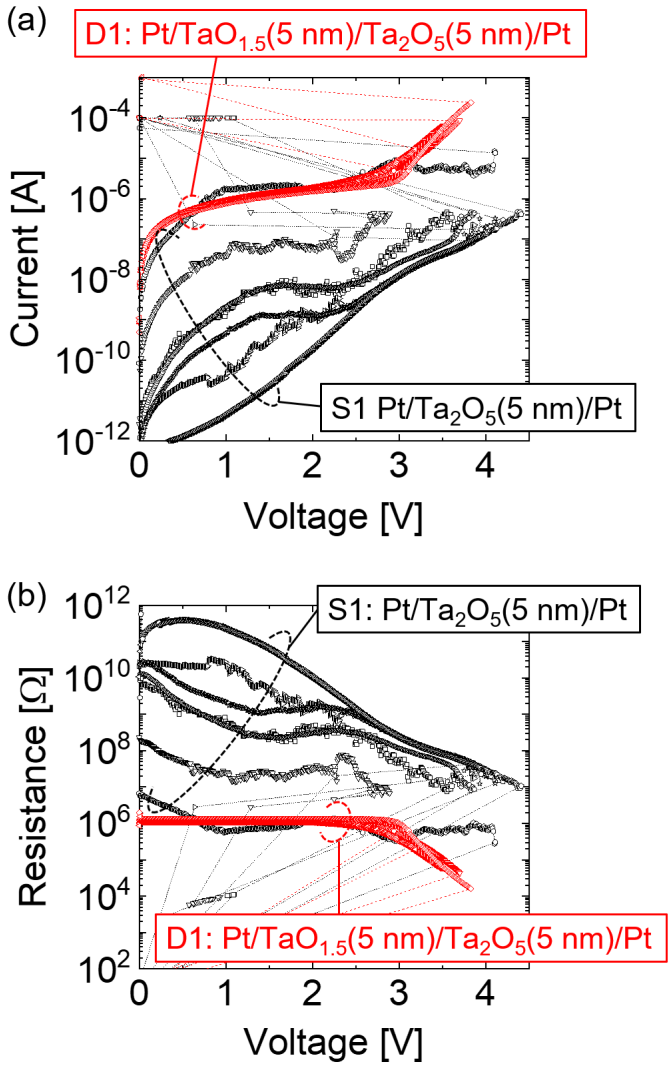

Figure 3.5: Current-voltage and resistance-voltage characteristics in the initial state of Pt/Ta_2O_5(5 nm)/Pt cells (sample S1) and Pt/TaO_x(5 nm)/Ta_2O_5(5 nm)/Pt cells (sample D1).

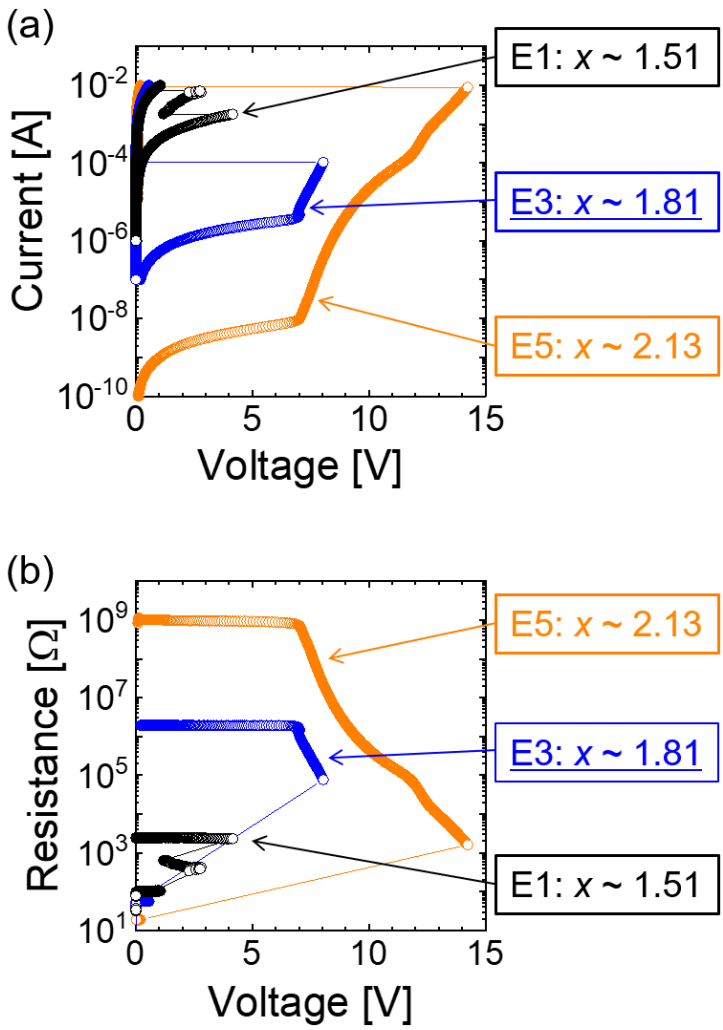

Figure 3.6: Current-voltage and resistance-voltage characteristics in the initial state of Pt/TaO_x(25 nm)/Ta_2O_5(10 nm)/Pt cells with various oxygen composition x (sample E1, E3, and E5).

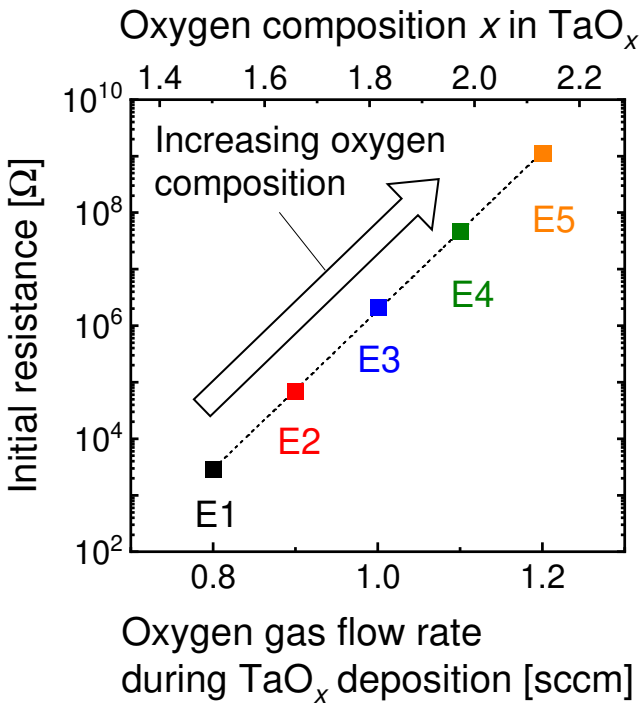

Figure 3.7: Dependence of initial resistance (R_{ini}) on oxygen composition of the TaO_x layer in Pt/TaO_x(25 nm)/Ta_2O_5(10 nm)/Pt cells (sample E1–E5).

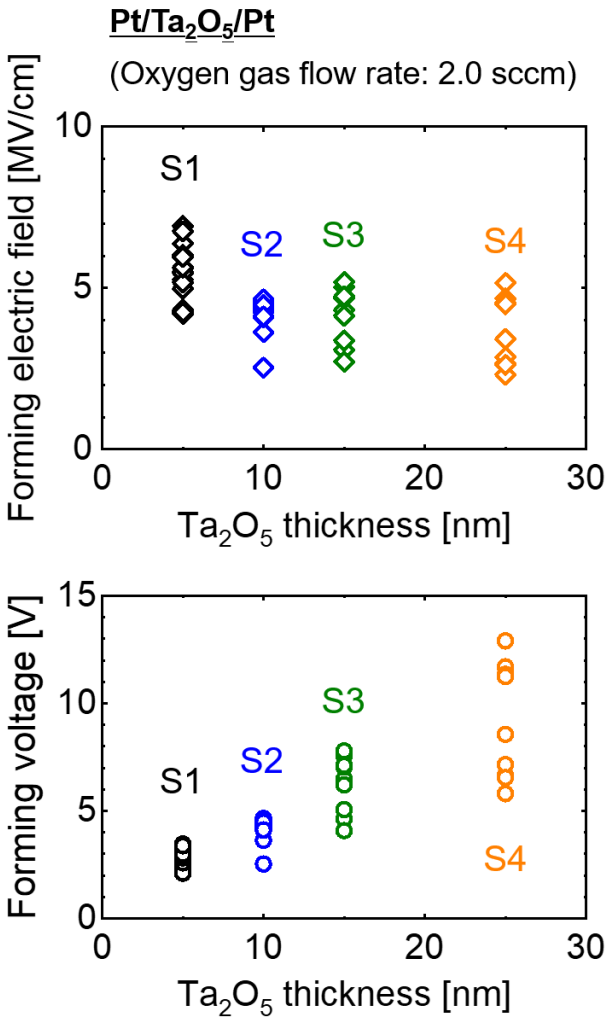

Figure 3.8: Dependence of forming voltage (V_{form}) and the intensity of forming electric field on the Ta_2O_5 thickness in $Pt/Ta_2O_5/Pt$ cells.

(VRH) [4], Efros-Shklovskii's VRH [10], and Schottky emission [11]. However, few studies were performed on initial states before applying electrical stress. As shown in Fig. 3.5, the introduction of the TaO_x layer has significant impacts on electrical characteristics in the initial states of Pt/TaO_x/Ta_2O_5/Pt cells. For investigation of the impacts of introducing the TaO_x layer, it is very important to clarify the electrical conduction mechanisms in the initial state of Pt/TaO_x/Ta_2O_5/Pt cells, where the variation in I–V characteristics is small. Therefore, the author semi-quantitatively investigated the conduction mechanisms of Pt/TaO_x/Ta_2O_5/Pt cells in the initial state by AC and DC measurements.

3.4.1 DC measurement

Dominant conduction mechanisms

Figure 3.9 exhibits temperature dependence of G_{ini} for the samples of D1, D2, and D3 in a semi-logarithmic plot with the horizontal axis representing the $-1/4$ power of temperature T. The linear characteristics in the low-temperature region below 200 K are attributed to Mott's VRH conduction [12]. In Mott's VRH, carriers possibly tunnel between localized states with small energy differences. The VRH conduction generally dominates conductivity in a low-temperature region, and the conductivity is represented by [12]

$$\sigma_{\mathrm{VRH}} = \sigma_0 \exp\left[-\left(\frac{T_0}{T}\right)\right], \tag{3.1}$$

$$T_0 = \frac{24\alpha^3}{\pi k_{\mathrm{B}} N_{\mathrm{F}}}. \tag{3.2}$$

Here, N_{F}, σ_0, α, and k_{B} are the density of states near the Fermi level, the conductivity limit at higher N_{F}, a decay parameter of wave functions of localized states, and the Boltzmann constant, respectively. Assuming that α is 0.86 nm^{-1}, which is valid in disordered film [13], N_{F} was calculated from the slope in the low-temperature region below 200 K in Fig. 3.9, as shown in Table 3.4. The VRH conduction contributed to the DC conductance even around room temperature and the linear characteristics due to VRH conduction obtained from the low-temperature region in Fig. 3.9 could be extended toward the high-temperature side. To elucidate the mechanism of the increase of the G_{ini} at a higher temperature, the contribution of Mott's VRH (G_{VRH}) was subtracted from the G_{ini}. Here, temperature-dependent G_{VRH} can be determined from Eq. (3.1), Eq. (3.2), and Table 3.4. Figure 3.10 shows the temperature dependence of G_{ini} and $G_{\mathrm{ini}} - G_{\mathrm{VRH}}$ in the sample of D2. As shown in Fig. 3.10, $G_{\mathrm{ini}} - G_{\mathrm{VRH}}$ increases exponentially from 200 to 380 K with an activation energy E_{a} of 180 meV. This result reveals that band conduction with the thermally activated temperature dependence of conductivity is dominant in parallel with Mott's VRH. The activation energy in the samples of D1 and D3 was also calculated by the same process, as denoted in Table 3.4. Figure 3.11 shows the temperature dependence of G_{ini} in Pt/TaO_x(25 nm)/Ta_2O_5(10 nm)/Pt cells with various oxygen compositions x (sample E1–E3). Similarly, N_{F} and E_{a} were calculated from the temperature dependence in Fig. 3.11, as shown in

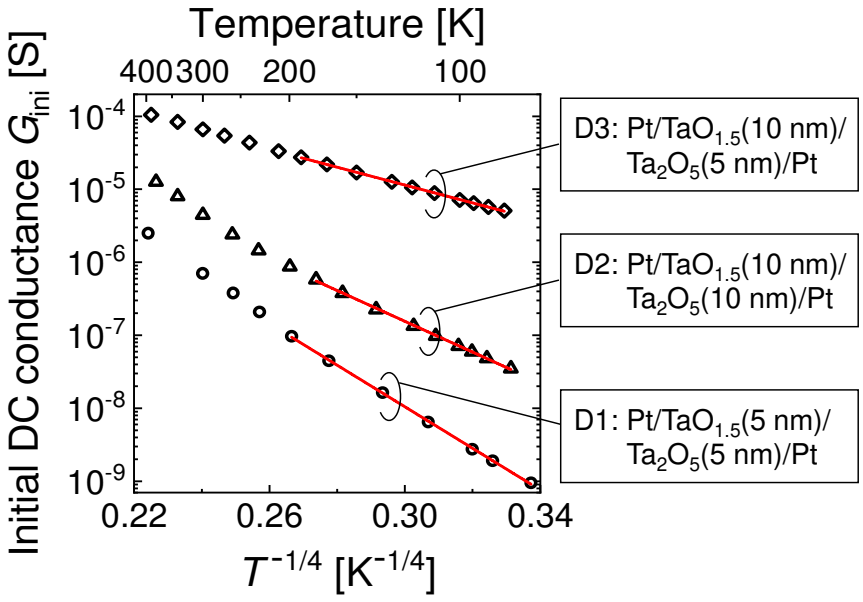

Figure 3.9: Temperature dependence of DC conductance at 0.1 V in initial states ($G_{\rm ini}$) of the samples of D1, D2 and D3 in a semi-logarithmic plot with the horizontal axis representing the $-1/4$ power of temperature.

Table 3.4: Physical parameters of Mott's VRH derived from Eq. (3.1), Eq. (3.2), and the slope of temperature dependence in Fig. 3.9 and Fig. 3.11. It was assumed that the value of α in Eq. (3.2) is 0.86 $\rm nm^{-1}$. The activation energy $E_{\rm a}$ in each sample was calculated from the slope of an Arrhenius plot of a conductance component obtained by $G_{\rm ini}$ minus $G_{\rm VRH}$, as shown in Fig. 3.10.

sample name	T_0[K]	$N_{\rm F}$ [$\rm cm^{-3}eV^{-1}$]	$E_{\rm a}$ [meV]
D1	1.8×10^{7}	3.1×10^{18}	190
D2	5.6×10^{6}	1.0×10^{19}	180
D3	6.3×10^{5}	9.0×10^{19}	110
E1	1.3×10^{5}	4.4×10^{20}	—
E2	7.9×10^{6}	7.1×10^{18}	100
E3	6.8×10^{7}	8.3×10^{17}	220

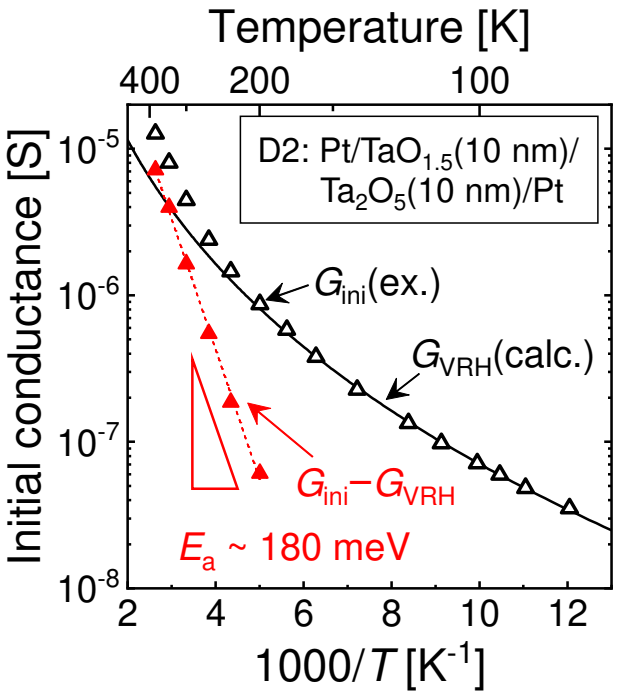

Figure 3.10: Temperature dependence of DC conductance $G_{\rm ini}$ and $G_{\rm ini}$ $-G_{\rm VRH}$ in a Pt/TaO_x (10 nm)/Ta_2O_5 (10 nm)/Pt cell (sample D2). $G_{\rm VRH}$ is a component of DC conductance contributed by Mott's VRH conduction.

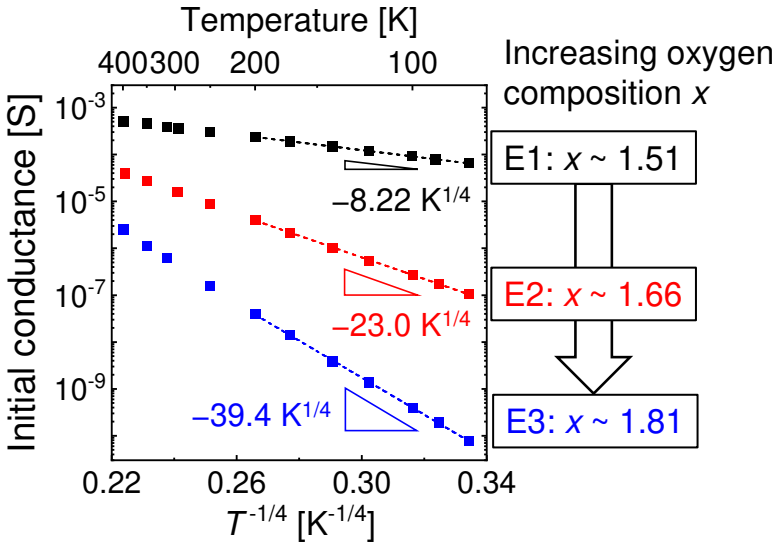

Figure 3.11: Temperature dependence of $G_{\rm ini}$ in Pt/TaO_x(25 nm)/Ta_2O_5(10 nm)/Pt cells with various oxygen composition x (sample E1–E3).

Table 3.4. Thus, the analyses of the temperature dependence of G_{ini} for the samples of D1–D3 and E1–E3 provide a positive correlation between G_{ini} and N_{F}, as shown in Fig. 3.12.

Discussion on the origin of localized states

As shown in Table 3.4 and Fig. 3.12, N_{F} depends mainly on the thickness and oxygen composition x of the TaO_x layer. In addition, Mott's VRH conduction, which is conduction through the localized states, is dominant in Pt/TaO_x/Ta_2O_5/Pt cells with the TaO_x layer. These results suggest that the localized states in the Ta_2O_5 layer are attributed to stacking the TaO_x layer. Moreover, the results of RBS in Chapter 2 suggest that oxygen migration from the stoichiometric layer to the Ta-rich TaO_x layer occurs throughout the TaO_x/Ta_2O_5 interface, not at a local spot, even in the as-deposited Pt/TaO_x/Ta_2O_5/Pt cells before the voltage is applied. The author, therefore, considered that the origin of the localized states could be V_Os in the Ta_2O_5 layer caused by the oxygen migration from the Ta_2O_5 layer to the TaO_x layer.

Discussion on activation energy

The activation energy E_{a} tends to decrease with an increase in N_{F}. Similar relation between activation energy and impurity concentration, which is ascribed to the overlap of Coulomb potentials, is well-known in other semiconductor materials [14, 15]. The activation energy $E_{\mathrm{a}}(c)$ dependent on impurity concentration c is represented by

$$E_{\mathrm{a}}(c) = E_{\mathrm{a0}} - ac^{\frac{1}{3}}, \tag{3.3}$$

where c, a, and E_{a0} are impurity concentration, coefficient, and activation energy at sufficiently low impurity concentration. The lowering term of activation energy is inversely proportional to the average distance between ionized impurities, thus proportional to the 1/3-power of the impurity concentration. Previous studies have revealed that V_Os are stable in positively charged states in the Ta_2O_5 layer [16]. Assuming that the V_O density is equal to 0.1 eV·N_{F}, the relationship between the cube root of the V_O density, i.e., the inverse of the average distance between V_Os, and the activation energy E_{a} was obtained as shown in Fig. 3.13. The Coulomb potentials of neighboring V_Os overlap when the V_O density is high, approximately over 10^{18} cm^{-3}, resulting in lowering E_{a}.

3.4.2 AC measurement

The AC conductance G_{tot} can be separated into a DC conductance component G_{ini} and a component dependent on frequency $G(\omega)$ [17]. The author analyzed frequency dependence of $G(\omega)$ [18]. G_{ini} was defined as the saturation value of G_{tot} at the minimum angular frequency of 240 rad/s. Figure 3.14 shows the frequency dependence of each conductance of G_{tot} and $G(\omega)$ with a log-log plot in the samples of S2 and D2 at 300 K. Here, for the

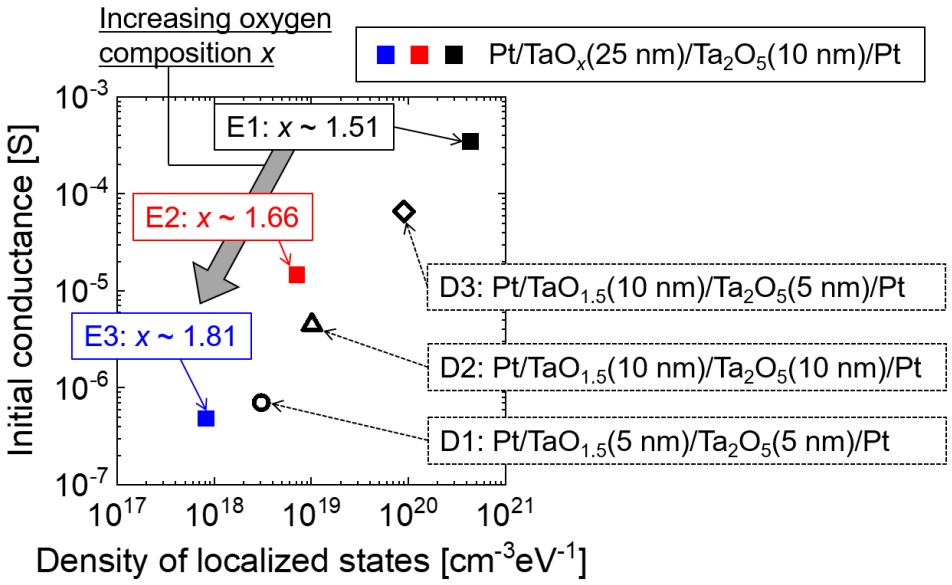

Figure 3.12: The relationship between G_{ini} and N_{F} in $\mathrm{Pt/TaO}_x\mathrm{/Ta_2O_5/Pt}$ cells (sample D1–D3 and E1–E3).

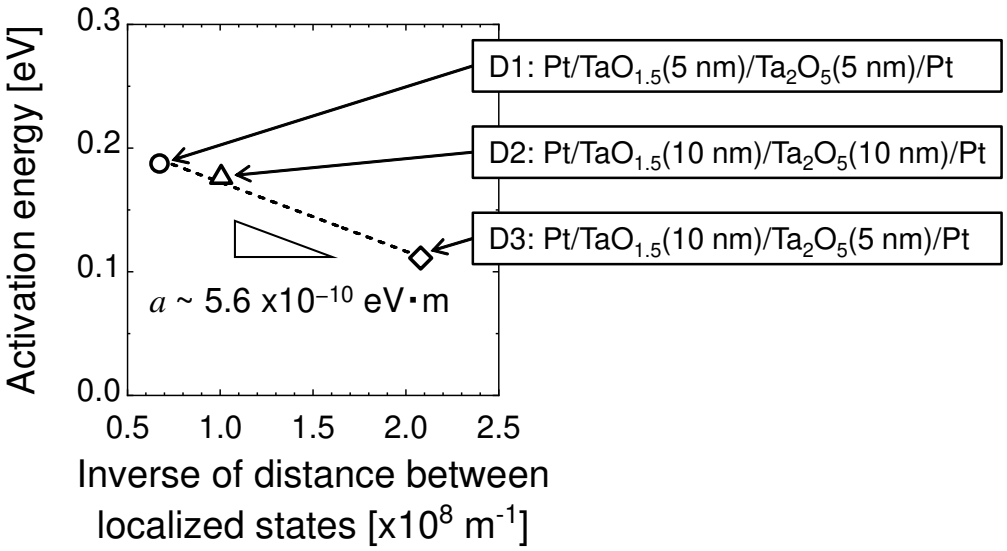

Figure 3.13: The relationship between the cube root of the $\mathrm{V_O}$ density, i.e., the inverse of the average distance between $\mathrm{V_O}$s, and the activation energy E_{a} under the assumption that the $\mathrm{V_O}$ density is equal to 0.1 eV·N_{F}. The activation energy dependent on impurity concentration $E_{\mathrm{a}}(c)$ is represented by $E_{\mathrm{a}}(c) = E_{\mathrm{a0}} - ac^{\frac{1}{3}}$, where c, a, and E_{a0} are impurity concentration, coefficient, and activation energy at sufficiently low impurity concentration.

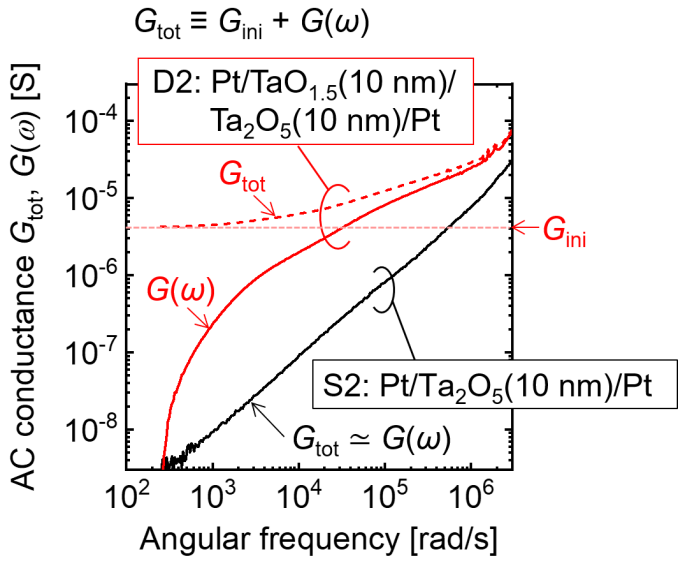

Figure 3.14: Frequency characteristics of AC conductance $G_{\rm tot}$ and its frequency dependent component $G(\omega)$ in Pt/Ta$_2$O$_5$(10 nm)/Pt and Pt/TaO$_x$(10 nm)/Ta$_2$O$_5$(10 nm)/Pt cells. $G(\omega)$ is obtained by subtracting DC conductance component saturated at extremely low frequency from $G_{\rm tot}$.

sample of S2 with a large variation of DC characteristics, the AC characteristics of a cell that shows $R_{\rm ini}$ of about $10^1 1\Omega$ were presented.

The introduction of the TaO_x layer changed $G(\omega)$ characteristics significantly. Figure 3.15 shows the frequency characteristics of $G(\omega)$ at different temperatures in the sample of D2. This frequency dependence from 10^3 to 10^6 rad/s is expressed as

$$G(\omega) = A\omega^s, \tag{3.4}$$

where A is a constant. The slope s at a fixed frequency in the log$G(\omega)$-logω plots exhibits weak temperature dependence. The inset in Fig. 3.15 shows the temperature dependence of the s value at 100 krad/s, indicating that the s value satisfies $\partial s/\partial T > 0$. The positive temperature dependence of the s value can be understood by the Small Polaron Tunneling (SPT) model [17], which is relaxation of small polarons formed by carrier hopping between a pair of localized states near the Fermi level. The relaxation time τ and the s value in the SPT model is expressed by [17, 18]

$$\tau = \tau_{0\rm p} \exp\left(2\alpha R\right) \exp\left(\frac{W_{\rm H}}{k_{\rm B}T}\right), \tag{3.5}$$

$$s = 1 + \frac{4}{\ln(\omega\tau_{0\rm p}) + \frac{W_{\rm H}}{k_{\rm B}T}} \tag{3.6}$$

where $\tau_{0\rm p}$, R, and $W_{\rm H}$ are a relaxation time limit between neighboring states at high temperature, distance between the states, and an activation energy of small polarons, respectively. The dashed lines in Fig. 3.15 indicate fitting curves of log$G(\omega)$–logω characteristics by the SPT model. The fitting parameters $\tau_{0\rm p}$ and $W_{\rm H}$ are $1 \times 10^{13} s^{-1}$ and 80 meV independent of temperature, respectively. The order of $\tau_{0\rm p}$ is reasonable as it agrees with the inverse of the optical phonon frequency [17, 18]. Note that the angular frequency ranges above 200 krad/s should be excluded from the fitting range because $G(\omega)$ includes parasitic impedance. Similarly, the angular frequency ranges below 3 krad/s should be excluded from the fitting range because the relaxation time τ is finite [19].

As a result, AC conductance $G_{\rm tot}$ in the low-frequency region below 1 krad/s as well as DC conductance $G_{\rm ini}$, are dominated by Mott's VRH and band conduction. However, $G_{\rm tot}$ in the high-frequency region above 100 krad/s, which is nearly equal to $G(\omega)$, is dominated by SPT, as shown in Table 3.5. Note that both Mott's VRH and SPT are transport mechanisms of carriers trapped in localized states. Since the localized states are generated by the introduction of the TaO_x layer, the origin of the localized states seems to be V_Os in the Ta_2O_5 layer, as described in Section 3.4.1.

3.4.3 Discussion

Figure 3.16 shows the cell size dependence of $G_{\rm tot}$ at 240 rad/s and 600 krad/s at 300 K in the diameter range of 100–500 μm in the sample of D2. AC conductance $G_{\rm tot}$ is proportional to the cell size in the high-frequency region around 600 krad/s, in which transport of

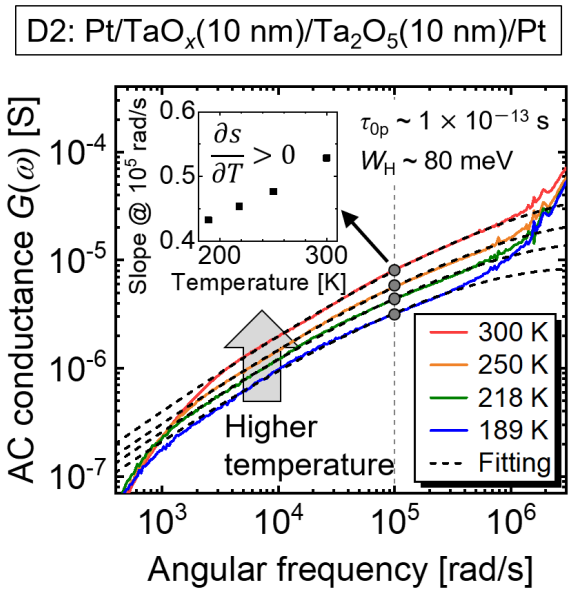

Figure 3.15: Frequency characteristics $G(\omega)$ and fitting curves in a Pt/TaO$_x$(10 nm)/Ta$_2$O$_5$(10 nm)/Pt cell at different temperatures. The inset is temperature dependence of s value at 10^5 rad/s, revealing that $\partial s/\partial T$ is positive.

Table 3.5: Dominant conduction mechanism contributing to electrical conductivity.

	Low frequency (DC)	High frequency above 100 krad/s
200–400 K	Band‖VRH	SPT
80–200 K	VRH	—

(VRH: Mott's variable range hopping, SPT: small polaron tunneling)

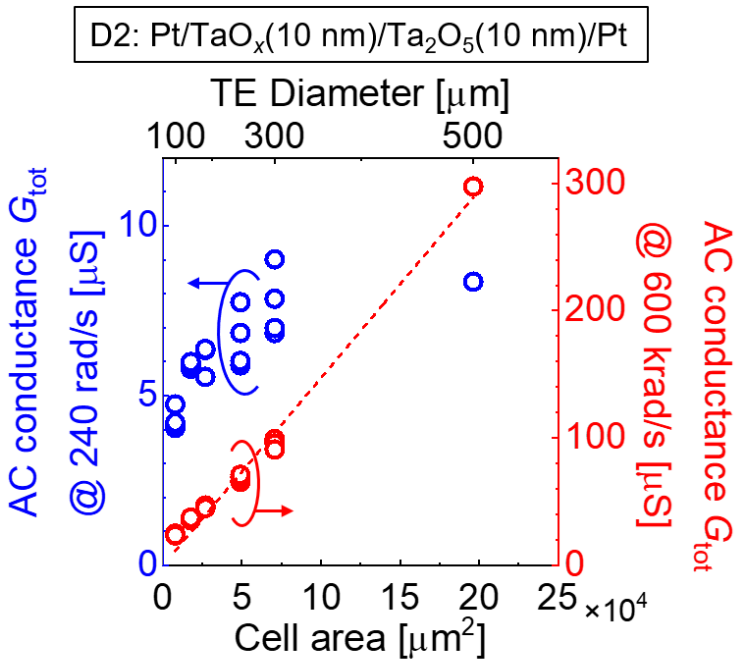

Figure 3.16: Cell area dependence of AC conductance G_{tot} in Pt/TaO_x (10 nm)/Ta_2O_5 (10 nm)/Pt cells at different frequencies. The AC conductance G_{tot} at 600 krad/s is proportional to the cell size. In contrast, G_{tot} at 240 rad/s exhibits a large dispersion and positive correlation with the cell size.

small polarons between a pair of states with a fast relaxation time, which means smaller τ, dominates the conductivity. The result implies that high-density V_Os are almost uniformly distributed in the TaO_x side of the Ta_2O_5 layer by the redox reaction because the fast relaxation time suggests a small distance between the states according to Eq. (3.4). In contrast, at the low frequency of 240 rad/s (almost DC), the cell size dependence of G_{tot} exhibits a large dispersion and is not proportional to the cell size. Similarly, Fig. 3.17 shows the cell size dependence of G_{ini}, which is dominated by Mott's VRH and band conduction, in the samples of D2, E3, and E5. These cell size dependences in the low-frequency region indicate that local conductive paths are non-uniformly distributed in the Ta_2O_5 layer. Based on the result, it can be speculated that the introduction of the TaO_x layer causes the formation of local conductive paths in the as-deposited cells by the V_O migration without applying voltage, as schematically illustrated in Fig. 3.18. The cell size dependences of G_{tot} in different frequency regions reflect the difference of V_O distribution in the Ta_2O_5 layer and dominant conduction mechanisms in the cells. Furthermore, the author demonstrated forming-free RS characteristics, which means that the cell resistance values in the initial state and the high-resistance state (HRS) are comparable [1, 5, 20–22], in $Pt/TaO_x/Ta_2O_5/Pt$ cells by the introduction of the TaO_x layer, as shown in Fig. 3.19. Fig. 3.19 presents typical I–V characteristics of bipolar RS in the sample of D3, which revealed the similarity of the characteristics in the initial state and HRS. To investigate temperature dependence of conductance in the HRS G_{HRS}, forming and then sufficient reset processes were performed in a cell of sample D3, as shown in Fig. 3.20. The cell resistance increases up to R_{ini} due to a reset process when applying a negative voltage, which means that R_{HRS} is equal to R_{ini}. Fig. 3.21 shows the temperature dependence of G_{HRS} ($= 1/R_{\mathrm{HRS}}$) in the cell, indicating that it is similar to the temperature dependence of G_{ini}, as shown in Fig. 3.10. These results mean that the HRS is almost equivalent to the initial state after sufficient reset processes. The initial resistance dependent on the dominant conduction mechanisms determines the cell resistance in the HRS.

3.5 Oxygen migration between TaO_x and Ta_2O_5 layers

In this section, the author experimentally characterized the oxygen migration from the Ta_2O_5 layer to the TaO_x layer in the as-deposited $Pt/TaO_x/Ta_2O_5/Pt$ cells.

3.5.1 Characterization methods using oxygen isotopes

To investigate oxygen exchange between the TaO_x and Ta_2O_5 layers, $Ta^{16}O_x/Ta_2{}^{18}O_5/Pt$ and $Ta^{16}O_x/Ta_2{}^{16}O_5/Pt$ samples were prepared by using isotope $^{16}O_2$ and $^{18}O_2$ gases as the reactive oxygen gas during the RF sputtering deposition. The purities of $^{16}O_2$ and $^{18}O_2$

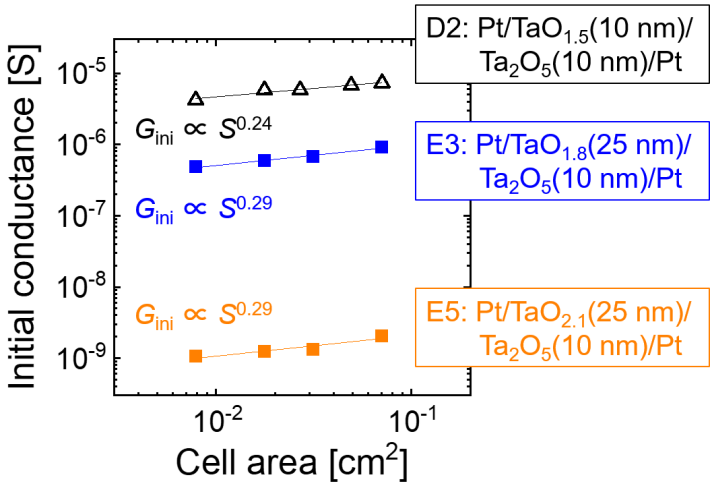

Figure 3.17: Cell area dependence of DC conductance G_{ini} in the samples of D2, E3, and E5, indicating positive correlation with the cell size.

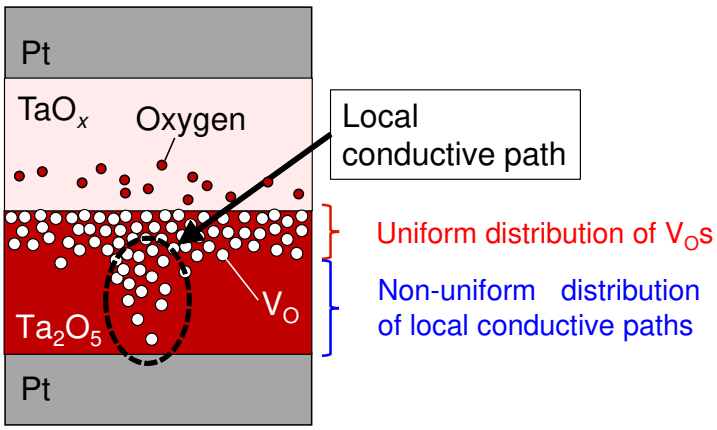

Figure 3.18: Schematic illustration of distribution of oxygen vacancies (V_Os) in a $Pt/TaO_x/Ta_2O_5/Pt$ cell. From the linear relationship of G_{tot} in the high frequency region, V_Os are almost uniformly distributed. Filamentary conductive paths are non-uniformly formed in a Ta_2O_5 layer even in the initial state as speculated from the dispersion and the positive correlation of G_{tot} in the low frequency region.

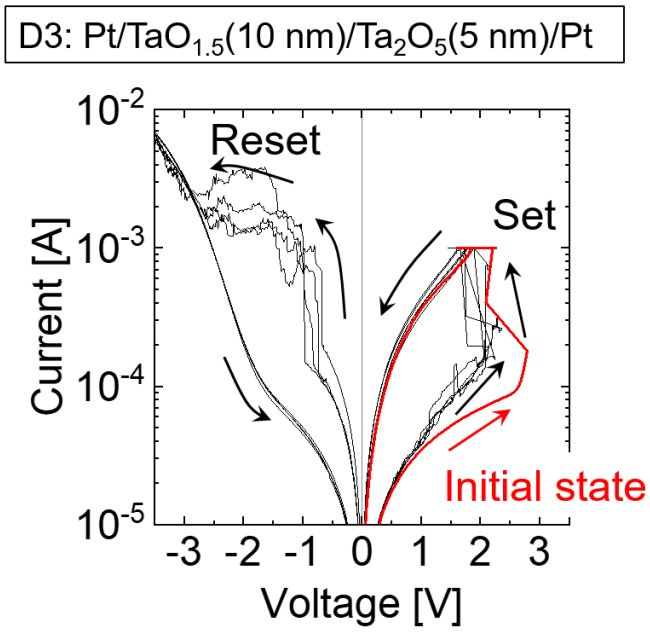

Figure 3.19: Typical resistive switching characteristics in the sample of D3. The initial conductance G_{ini} was almost equal to the resistance after reset processes.

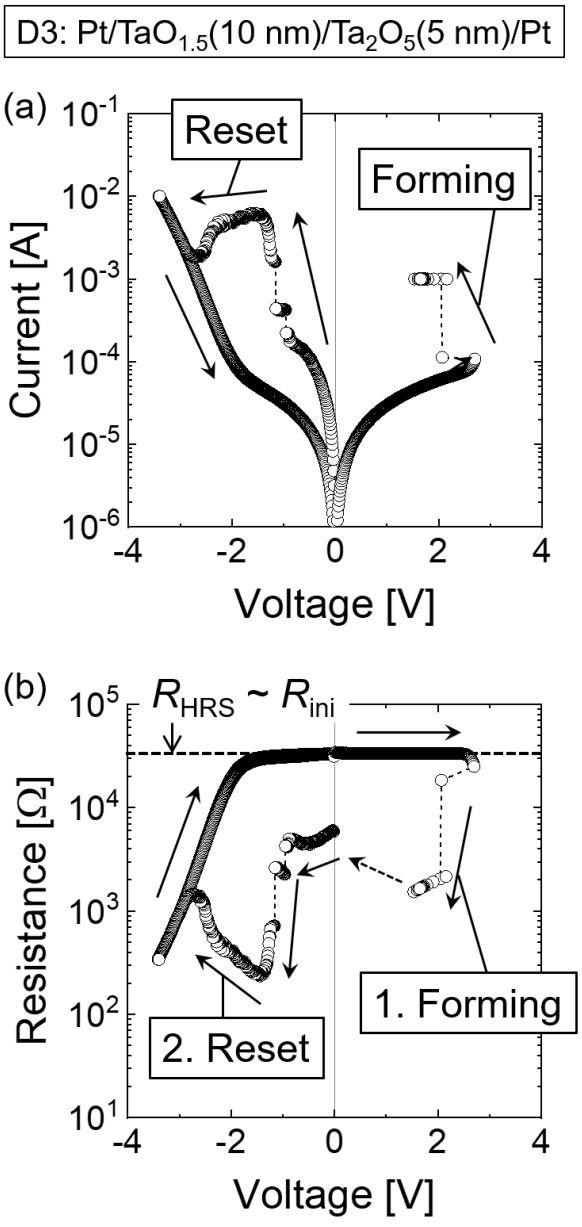

Figure 3.20: Current–voltage and Resistance–voltage characteristics when forming and then sufficient reset processes were performed in a cell of sample D3. The cell resistance increases up to the initial resistance R_{ini} due to a reset process when applying a negative voltage, which means that the resistance in the high-resistance state (R_{HRS}) is equal to R_{ini}.

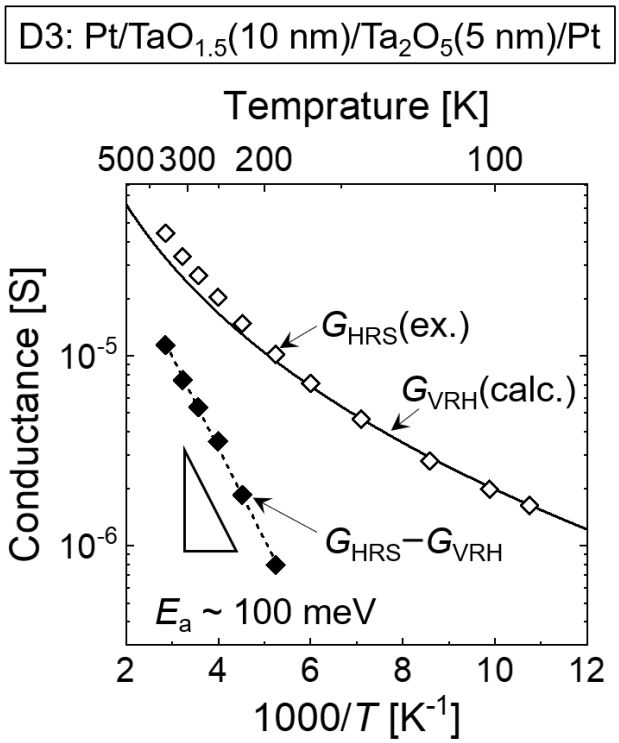

Figure 3.21: The temperature dependence of G_{HRS} $(= 1/R_{\mathrm{HRS}})$ in the cell after the sufficient reset process presented in Fig. 3.20.

gases are 99.99995% and 98%, respectively. Note that these samples were not exposed to the atmosphere between the deposition of the Ta_2O_5 and TaO_x layers. Moreover, in order to discharge the residual $^{18}O_2$ gas, evacuation up to 2×10^{-5} Pa and injection of $^{16}O_2$ gas were repeated 5 times after the deposition of $Ta_2{}^{18}O_5$. To prevent the mixture of ^{16}O and ^{18}O on a Ta target, different Ta targets were used for the deposition of $Ta^{16}O_x$ and $Ta_2{}^{18}O_5$.

3.5.2 ^{18}O and ^{16}O atom profiles in TaO_x and Ta_2O_5 layers

Figure 3.22 shows secondary-ion mass spectrometry (SIMS) profiles for $Ta^{16}O_x/Ta_2{}^{18}O_5/Pt$ and $Ta^{16}O_x/Ta_2{}^{16}O_5/Pt$ samples. The ^{18}O intensity in the depth profile for the $Ta^{16}O_x/Ta_2{}^{16}O_5/Pt$ structure is derived from $^{18}O_2$ molecules in the high-purity $^{16}O_2$ gas. The ^{18}O intensity in the $Ta^{16}O_x$ layer for the $Ta^{16}O_x/Ta_2{}^{18}O_5/Pt$ structure is four times greater than that in the $Ta^{16}O_x$ layer for the $Ta^{16}O_x/Ta_2{}^{16}O_5/Pt$ structure. This result reveals that ^{18}O was supplied from the $Ta_2{}^{18}O_5$ layer to the $Ta^{16}O_x$ layer. Because of the low purity of the $^{18}O_2$ gas in contrast to the high-purity $^{16}O_2$ gas, the ^{16}O intensity in the $Ta_2{}^{18}O_5$ layer for the $Ta^{16}O_x/Ta_2{}^{18}O_5/Pt$ structure is considered to originate from $^{16}O_2$ molecules in the $^{18}O_2$ gas. Although the migration of ^{16}O from the $Ta^{16}O_x$ layer to the $Ta_2{}^{18}O_5$ layer occurs in the $Ta^{16}O_x/Ta_2{}^{18}O_5/Pt$ structure, the oxygen migration mainly occurs from the Ta_2O_5 layer to the TaO_x layer. Since the SIMS was performed for the as-deposited $TaO_x/Ta_2O_5/Pt$ structure, V_Os are supplied from the TaO_x layer to the stoichiometric Ta_2O_5 layer even in the absence of an applied voltage. Thus, the Ta-rich TaO_x layer with a resistance typically less than 100 Ω acts as a V_O reservoir layer.

3.6 Discussion

In this section, based on the above results, the author discusses the effects of the Ta-rich TaO_x layer. The results of SIMS in Fig. 3.22 revealed that just stacking the TaO_x layer on the Ta_2O_5 layer causes the V_O supply from the TaO_x layer to the Ta_2O_5 layer. The supplied V_O forms localized states in the Ta_2O_5 layer. As shown in Fig. 3.12, the density of localized states in the Ta_2O_5 layer, corresponding to the V_O density, depends on the oxygen composition x and thickness of the TaO_x layer. Fig. 3.23 schematically illustrates the relationship between the density of the supplied V_O and the oxygen composition x and thickness of the TaO_x layer. When the oxygen composition x of the TaO_x layer increases under the constant thickness, the TaO_x layer is less likely to incorporate oxygen and the V_O supply to the Ta_2O_5 layer is suppressed. On the other hand, when the thickness of the TaO_x layer increases under the constant x, the TaO_x layer can incorporate more oxygen and more V_Os are supplied to the Ta_2O_5 layer. Thus, the density of the supplied V_O can be controlled by the oxygen composition x and thickness in the TaO_x layer.

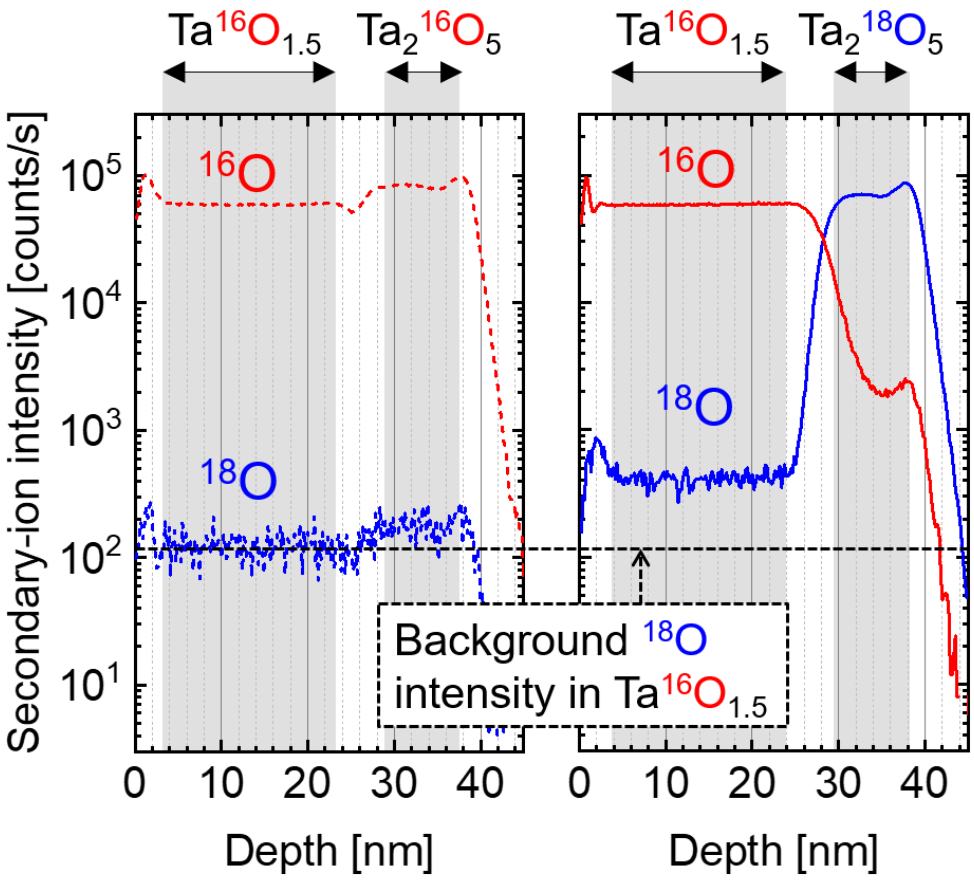

Figure 3.22: Secondary-ion mass spectrometry (SIMS) profiles for $Ta^{16}O_x/Ta_2^{18}O_5/Pt$ and $Ta^{16}O_x/Ta_2^{16}O_5/Pt$ samples.

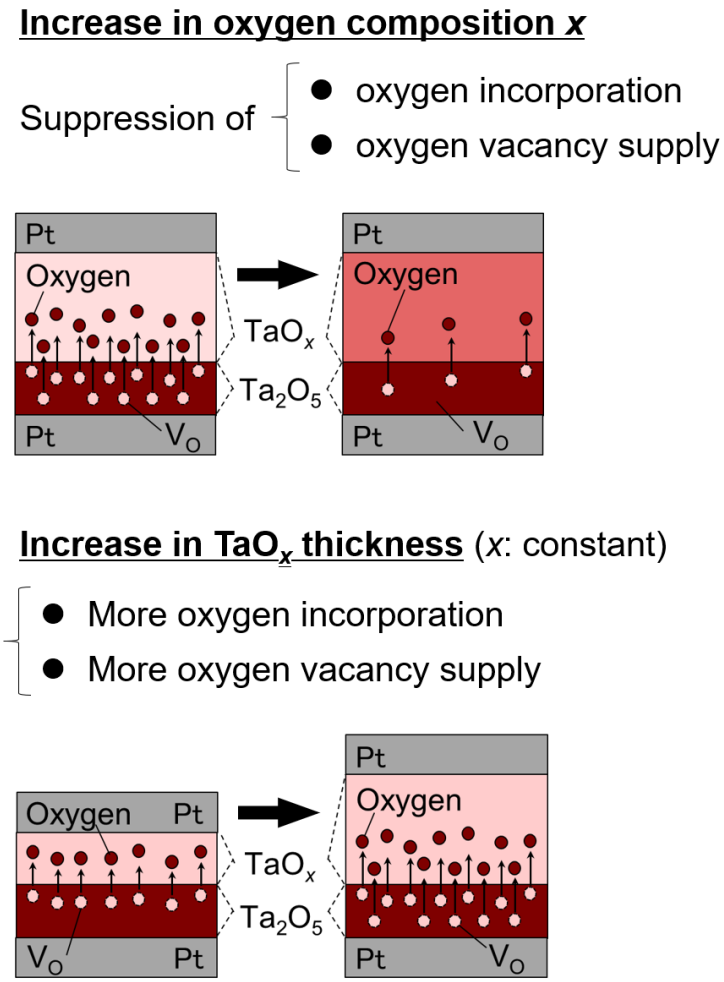

Figure 3.23: Schematic illustration of the relationship between the density of the supplied V_O and the oxygen composition x and thickness of the TaO_x layer.

3.7 Summary

The impacts of introducing a Ta-rich TaO_x layer on initial characteristics in $Pt/Ta_2O_5/Pt$ cells were investigated. First, comparing the initial electrical characteristics in $Pt/Ta_2O_5/Pt$ cells and $Pt/TaO_x/Ta_2O_5/Pt$ cells, where the diameter of the Pt top electrode is 100 μm, stacking the TaO_x layer significantly reduces the device-to-device variation. Second, in $Pt/TaO_x/Ta_2O_5/Pt$ cells, the temperature dependence of initial conductance with the small device-to-device variation was characterized in the wide temperature and frequency ranges to clarify the dominant conduction mechanism. The temperature dependence of DC conductance revealed that Mott's variable range hopping (VRH) conduction is dominant in the low-temperature region below 200 K, and that both VRH conduction and band conduction contribute to the DC conductance in parallel from 200 K to 400 K. In contrast, the frequency characteristics of AC conductance at different temperatures indicated that the relaxation of small polarons formed by carriers in the localized states contributed to AC conductance at high frequency. Moreover, the cell size dependence of AC conductance suggested that the introduction of a TaO_x layer formed filamentary conductive paths without applying voltage. Third, the results of secondary ion mass spectrometry for two samples prepared using oxygen isotopes as markers revealed that oxygen migration occurs from the Ta_2O_5 layer to the TaO_x layer, indicating that the origin of the localized states in the Ta_2O_5 layer could be oxygen vacancies supplied from the TaO_x layer. Finally, by using the VRH conduction equation, the density of V_Os in the Ta_2O_5 layer, corresponding to the localized states, was estimated from the temperature dependence of the initial resistance in $Pt/TaO_x/Ta_2O_5/Pt$ cells with different oxygen compositions of the TaO_x layer. It was quantitatively revealed that the density of V_Os supplied from the TaO_x layer to the Ta_2O_5 layer can be controlled by the oxygen composition (1.5–2.1) and thickness in the TaO_x layer.

References

[1] Y. S. Chen, H. Y. Lee, P. S. Chen, T. Y. Wu, C. C. Wang, P. J. Tzeng, F. Chen, M. J. Tsai, and C. Lien, *IEEE Electron Device Letters* **31**, 1473 (2010).

[2] M. J. Lee, C. B. Lee, D. Lee, S. R. Lee, M. Chang, J. H. Hur, Y. B. Kim, C. J. Kim, D. H. Seo, S. Seo, U. I. Chung, I. K. Yoo, and K. Kim, *Nature Materials* **10**, 625 (2011).

[3] B. Govoreanu, G. S. Kar, Y. Y. Chen, V. Paraschiv, S. Kubicek, A. Fantini, I. P. Radu, L. Goux, S. Clima, R. Degraeve, N. Jossart, O. Richard, T. Vandeweyer, K. Seo, P. Hendrickx, G. Pourtois, H. Bender, L. Altimime, D. J. Wouters, J. A. Kittl, and M. Jurczak, *Technical Digest - International Electron Devices Meeting 2008 (San Francisco, 2008)*, 729 (2011).

[4] Z. Wei, T. Takagi, Y. Kanzawa, Y. Katoh, T. Ninomiya, K. Kawai, S. Muraoka, S. Mitani, K. Katayama, S. Fujii, R. Miyanaga, Y. Kawashima, T. Mikawa, K. Shimakawa, and K. Aono, *Technical Digest - International Electron Devices Meeting 2011 (Washington DC, 2011)*, 721 (2011).

[5] J. P. Strachan, J. J. Yang, L. A. Montoro, C. A. Ospina, A. J. Ramirez, A. L. Kilcoyne, G. Medeiros-Ribeiro, and R. S. Williams, *Beilstein Journal of Nanotechnology* **4**, 467 (2013).

[6] G. S. Park, Y. B. Kim, S. Y. Park, X. S. Li, S. Heo, M. J. Lee, M. Chang, J. H. Kwon, M. Kim, U. I. Chung, R. Dittmann, R. Waser, and K. Kim, *Nature Communications* **4**, 2382 (2013).

[7] F. Miao, J. P. Strachan, J. J. Yang, M. X. Zhang, I. Goldfarb, A. C. Torrezan, P. Eschbach, R. D. Kelley, G. Medeiros-Ribeiro, and R. S. Williams, *Advanced Materials* **23**, 5633 (2011).

[8] W. Kim, S. Menzel, D. J. Wouters, Y. Guo, J. Robertson, B. Roesgen, R. Waser, and V. Rana, *Nanoscale* **8**, 17774 (2016).

[9] Y. Zhang, N. Deng, H. Wu, Z. Yu, J. Zhang, and H. Qian, *Applied Physics Letters* **105**, 063508 (2014).

[10] C. M. Rosário, B. Thöner, A. Schönhals, S. Menzel, M. Wuttig, R. Waser, N. A. Sobolev, and D. J. Wouters, *Applied Physics Letters* **112**, 213504 (2018).

[11] C. E. Graves, N. Dávila, E. J. Merced-Grafals, S. T. Lam, J. P. Strachan, and R. S. Williams, *Applied Physics Letters* **110**, 123501 (2017).

[12] N. F. Mott and E. A. Davis, *Electronic Processes in Non-Crystalline Materials*, 2nd, Clarendon, Oxford, 32 (1979).

[13] I. Goldfarb, F. Miao, J. J. Yang, W. Yi, J. P. Strachan, M. X. Zhang, M. D. Pickett, G. Medeiros-Ribeiro, and R. S. Williams, *Applied Physics A: Materials Science and Processing* **107**, 1 (2012).

[14] G. L. Pearson and J. Bardeen, *Physical Review* **75**, 865 (1949).

[15] P. P. Debye and E. M. Conwell, *Physical Review* **93**, 693 (1954).

[16] J. Lee, W. D. Lu, and E. Kioupakis, *Nanoscale* **9**, 1120 (2017).

[17] A. R. Long, *Advances in Physics* **31**, 553 (1982).

[18] S. R. Elliott, *Advances in Physics* **36**, 135 (1987).

[19] G. E. Pike, *Physical Review B* **6**, 1572 (1972).

[20] Z. Fang, H. Y. Yu, X. Li, N. Singh, G. Q. Lo, and D. L. Kwong, *IEEE Electron Device Letters* **32**, 566 (2011).

[21] F. Kurnia, C. Liu, C. U. Jung, and B. W. Lee, *Applied Physics Letters* **102**, 152902 (2013).

[22] Z. Wan, R. B. Darling, A. Majumdar, and M. P. Anantram, *Applied Physics Letters* **111**, 041601 (2017).

Chapter 4

Semi-forming Phenomenon and Analog Resistive Switching in $Pt/TaO_x/Ta_2O_5/Pt$ Cells

4.1 Introduction

Numerous studies have reported gradual reset processes in binary transition metal oxide-based resistive switching (RS) cells [1–7]. In contrast, gradual set processes are often difficult to achieve [2, 7–11]. The lack of the gradual set processes might be caused by positive feedback between the filament growth and the rise in Joule heating within the conductive filament [4, 5]. The authors of some previous studies have demonstrated multi-level control of the cell resistance by suppressing the positive feedback with compliance currents, which induce undesired external circuits [5, 6]. Brivio *etal.* suggested that the positive feedback could be alleviated by the competition between set and reset processes [12]. Here, the author focused on the complementary RS, in which set and subsequent reset processes occur at both positive and negative voltages [13–15]. In the complementary RS, the growth and dissolution of a conductive filament could compete with and suppress each other. Figure 4.1 shows typical current–voltage (I–V) characteristics of complementary resistive switching (RS) and the qualitative model of the growth and dissolution of conductive filaments in the complementary RS [16]. In general, the complementary RS characteristics can be obtained in two bipolar RS cells connected anti-serially as shown in the schematic of Fig. 4.1 [16]. In these cells, the growth and dissolution of the conductive filaments occur in each spatially separated cell. Therefore, the growth and dissolution of the conductive filaments are less likely to interfere with each other. In contrast, in complementary RS operations in a single RS cell, the growth and dissolution of the conductive filament could compete with and suppress each other. Various RS operation modes, including the complementary RS mode, have been reported in some RS cells, such as those based on HfO_x and TaO_x [12, 14, 17]. However, experimental methods for controlling the various RS operation modes in a single

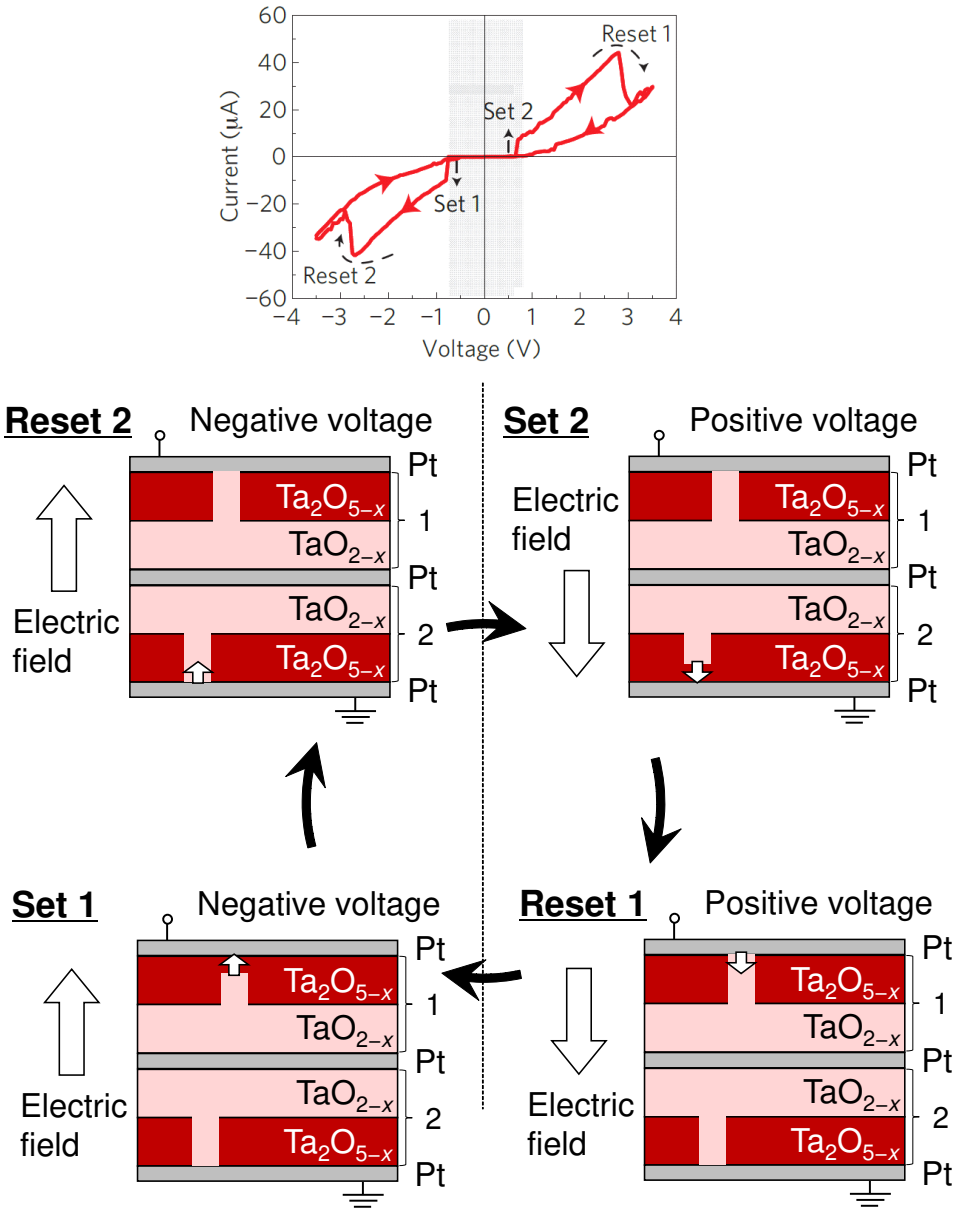

Figure 4.1: Typical current–voltage (I–V) characteristics of complementary resistive switching (RS) and the qualitative model of the growth and dissolution of conductive filaments [16].

RS cell have not been established.

In this section, forming and resistive switching characteristics were investigated in the $Pt/TaO_x/Ta_2O_5/Pt$ cells when the oxygen composition and thickness of the TaO_x layer were varied systematically, based on the results in Chap. 3. The purpose of this section is to demonstrate analog RS characteristics in the complementary RS operations.

4.2 Experimental methods

Pt(25 nm)/TaO_x/Ta_2O_5 (10 nm)/Pt(60 nm) cells were fabricated on a SiO_2/Si substrate, as shown in Fig. 4.2. The 60-nm-thick Pt layer as a bottom electrode (BE) was deposited by DC sputtering. The TaO_x layer with various thicknesses and the 10-nm-thick Ta_2O_5 layer were deposited by reactive radio-frequency sputtering. The oxygen compositions in the TaO_x and Ta_2O_5 layers were controlled by adjusting the oxygen gas flow rate at 0.8–1.2 sccm and 2.0 sccm, respectively, under an Ar gas flow at 5.0 sccm. Finally, Pt top electrodes (TEs) with a diameter of 100 μm were deposited by electron-beam evaporation. Forming and RS characteristics were evaluated for the $Pt/TaO_x/Ta_2O_5/Pt$ cells at room temperature using a Keithley 4200 semiconductor parameter analyzer with the BE grounded. These measurements were performed using voltage sweeps at a ramp rate of about 0.2 V/s.

4.3 Semi-forming phenomenon

Figure 4.3 shows typical I–V and resistance–voltage (R–V) characteristics in as-deposited $Pt/TaO_x/Ta_2O_5/Pt$ cells with a 25-nm-thick TaO_x layer deposited at an oxygen gas flow rate of 0.8 sccm, at which the oxygen composition of the TaO_x layer is about 1.5. Two modes of forming phenomena occur; the conventional forming phenomenon, which transits to a low resistance state less than 100 Ω, and the unique forming phenomenon in $Pt/TaO_x/Ta_2O_5/Pt$ cells, which transits to a higher resistance state more than 1 kΩ. Figure 4.4 shows typical RS characteristics after the conventional forming. The reset characteristics are symmetric irrespective of voltage polarity, which are called nonpolar RS, and are often observed in the RS cells with a symmetric stack structure such as $Pt/Ta_2O_5/Pt$. In the following section, the author investigated the unique forming phenomenon in $Pt/TaO_x/Ta_2O_5/Pt$ cells with the TaO_x layer as a V_O-reservoir, which is defined as "semi-forming", and subsequent RS characteristics.

4.3.1 Oxygen composition dependence in TaO_x

Fig. 4.5 shows the dependence of the initial resistance (R_{ini}) and the cell resistance after semi-forming (R_{semi}) on the oxygen composition x of the TaO_x layer when the oxygen gas flow rate was controlled between 0.8 sccm and 1.2 sccm by 0.1 sccm. The initial resistance R_{ini} exponentially increases with x from about 3 kΩ to about 1 GΩ, while R_{semi}

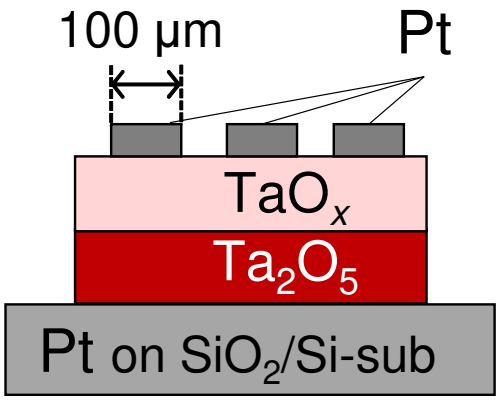

Figure 4.2: Stacking structures of the fabricated RS cells. The size of such capacitor-type RS cells is determined by the area of the Pt top electrode (TE).

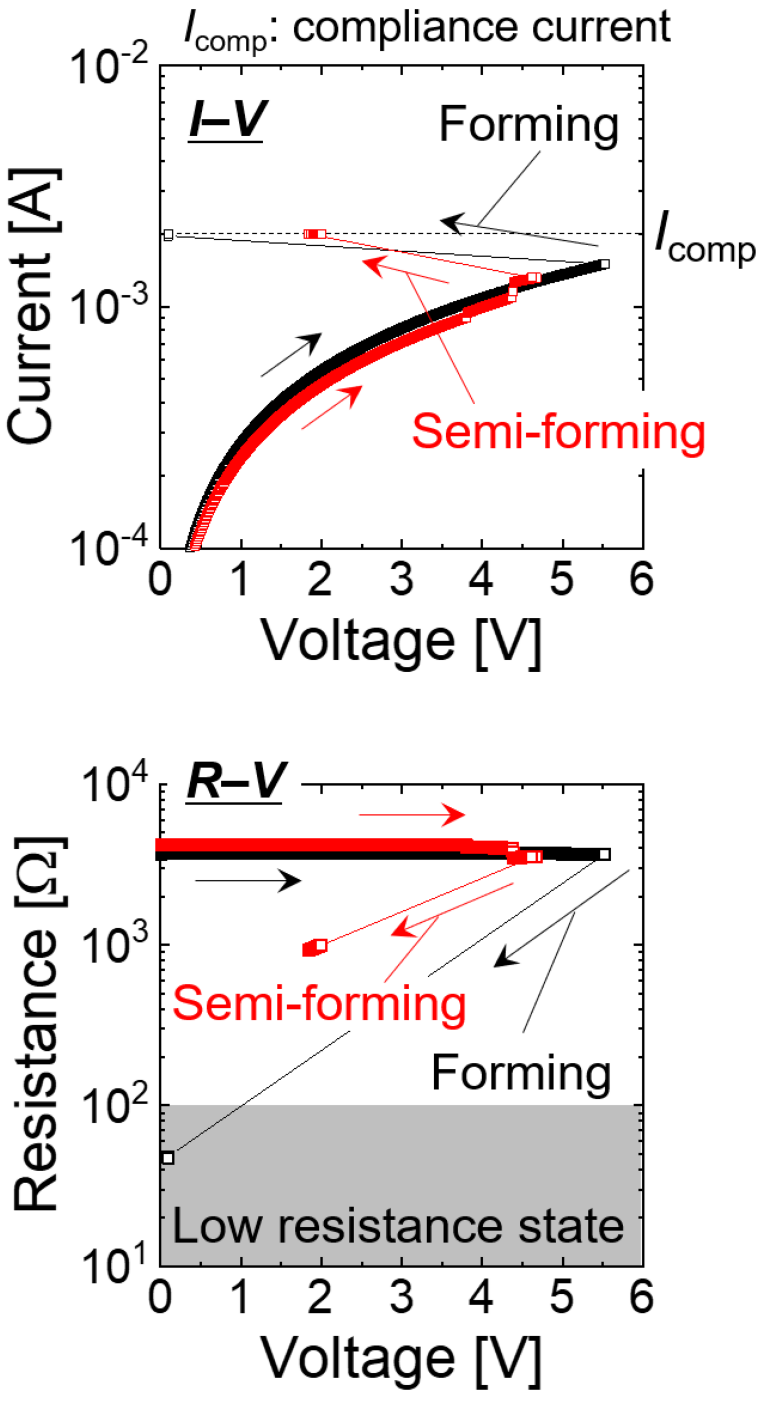

Figure 4.3: Typical I–V and resistance–voltage (R–V) characteristics in as-deposited Pt/TaO_x/Ta_2O_5/Pt cells with a 25-nm-thick TaO_x layer deposited at an oxygen gas flow rate of 0.8 sccm, at which the oxygen composition of the TaO_x layer is about 1.5.

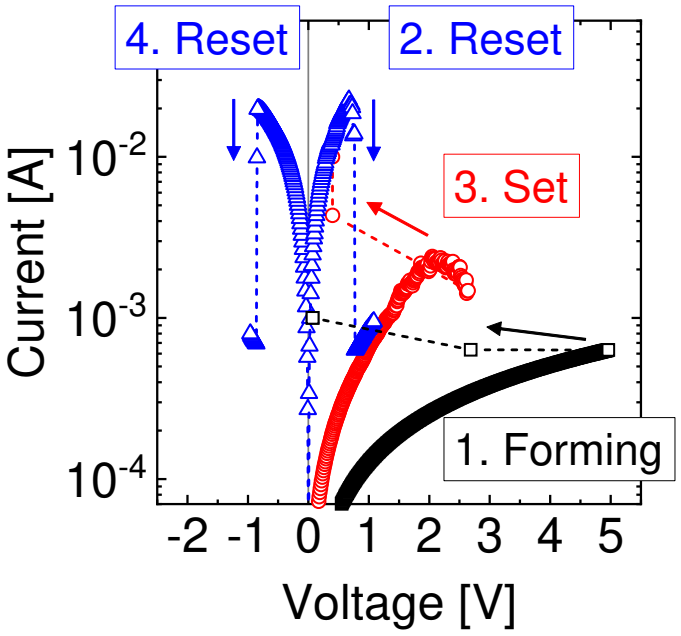

Figure 4.4: Nonpolar resistive switching (RS) characteristics after the conventional forming phenomenon.

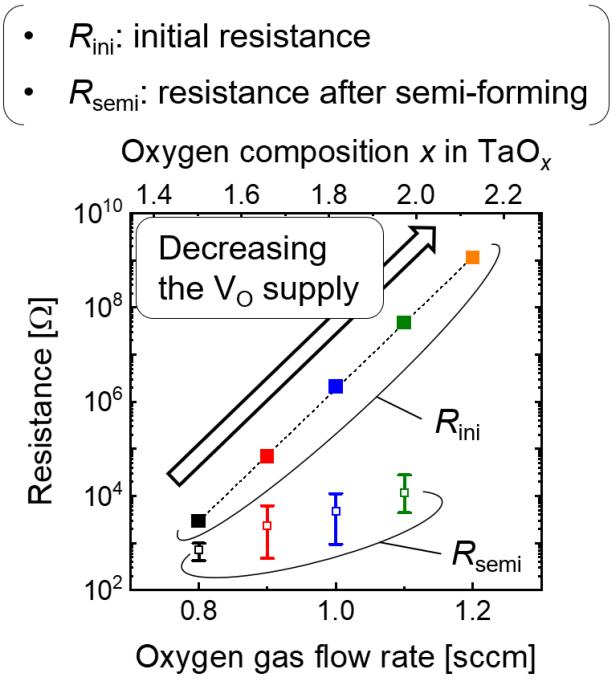

Figure 4.5: Oxygen composition x dependence of the initial resistance (R_{ini}) and the cell resistance after the semi-forming (R_{semi}) in Pt/TaO_x/Ta_2O_5/Pt cells.

also tends to increase. Fig. 4.6 shows the oxygen composition dependence of the relative occurrence frequency of the semi-forming phenomenon (F_{semi}) when forming characteristics were investigated for 20 cells at each oxygen gas flow rate. As the oxygen composition x increases, R_{ini} and R_{semi} increase while F_{semi} tends to decrease, which means the conventional forming phenomenon is more likely to occur. The frequency of semi-forming deteriorates due to the suppression of the V_O supply, based on the results in Chap. 3.

4.3.2 TaO_x thickness dependence

Fig. 4.7 shows the TaO_x thickness dependence of R_{ini} and F_{semi} when the oxygen composition x is 1.51, 1.81, and 2.13. As the TaO_x thickness increases, R_{ini} decreases and the decrease in R_{ini} tends to saturate. As described in Chap. 3, an increase in the TaO_x thickness causes more V_O supply to the Ta_2O_5 layer. The results in Fig. 4.7 indicate that the number of V_Os supplied from the TaO_x layer saturates for the TaO_x thickness. In contrast, F_{semi} tends to increase toward 1 as the TaO_x thickness increases. When the oxygen composition x is 2.13, even though the TaO_x thickness increases, F_{semi} hardly increases and the conventional forming occurs, suggesting that the saturated number of the supplied V_O from the TaO_x layer is not sufficient for semi-forming to occur.

4.3.3 Discussion

In this section, the author discusses the mechanism of the semi-forming phenomenon. As mentioned in Chap. 3, the supplied V_O from the TaO_x layer is expected to be distributed non-uniformly in the Ta_2O_5 layer. The non-uniformity in the V_O supply causes current concentration and accompanying local Joule heating when a positive voltage is applied to the top electrode (TE), as schematically shown in the left diagram of Fig. 4.8. The local Joule heating facilitates the growth of a conductive filament only at the local spot, which is referred to as the semi-forming phenomenon. As a result, a resistance of a filament gap above the partially formed filament contributes to the cell resistance after semi-forming, as shown in the right diagram of Fig. 4.8. The resistance of the filament gap depends roughly on the density of the supplied V_O. Owing to more insufficient V_O supply in the case of larger x, R_{semi} tends to increase with x. In contrast, F_{semi} tends to decrease with x because the current concentration and accompanying local Joule heating, as shown in Fig. 4.8, are less likely to occur due to the insufficient V_O supply, and thus, the conventional forming phenomenon is more likely to occur.

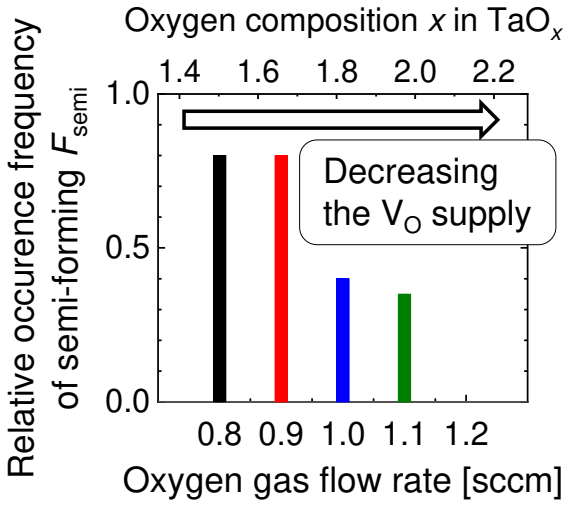

Figure 4.6: Oxygen composition x dependence of the relative occurrence frequency of semi-forming phenomenon (F_{semi}) when forming characteristics were investigated for 20 $\mathrm{Pt/TaO}_x\mathrm{/Ta_2O_5/Pt}$ cells.

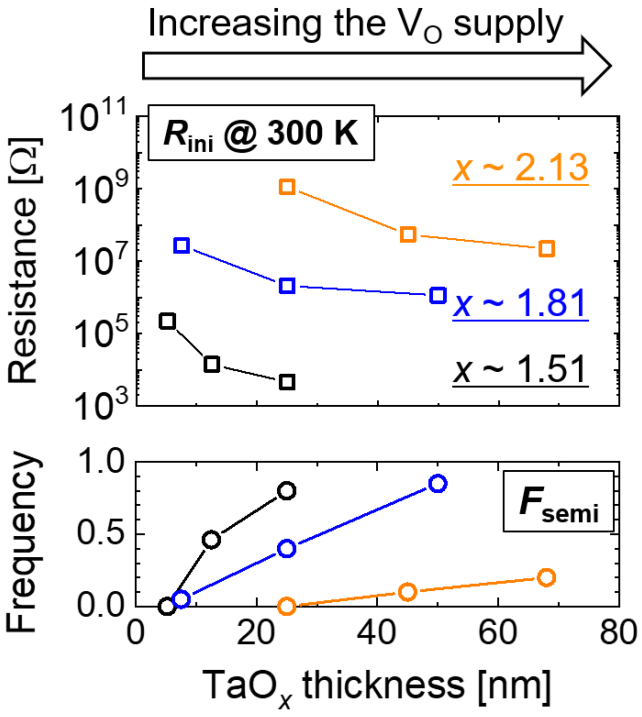

Figure 4.7: The TaO_x thickness dependence of R_{ini} and F_{semi} when the oxygen composition x is 1.51, 1.81, and 2.13.

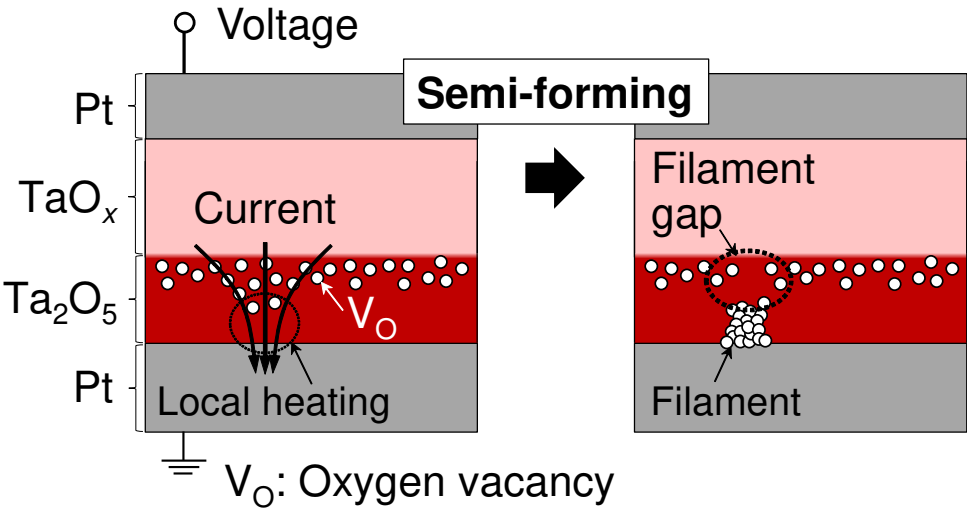

Figure 4.8: Schematic illustration of the mechanism of semi-forming.

4.4 Resistive switching characteristics after semi-forming phenomenon

Fig. 4.9 presents typical RS characteristics when a negative voltage is applied to the TE after semi-forming in Pt/$TaO_{1.5}$(25 nm)/Ta_2O_5(10 nm)/Pt cells. When a negative voltage sweep down to −4 V was performed, the cell resistance abruptly decreases at about −1 V (a set process) and subsequently increases over − 1 V (a reset process). On the other hand, when a positive voltage is applied to the TE after semi-forming, unipolar set and subsequent reset processes occur. Fig. 4.10 shows the typical unipolar RS characteristics after semi-forming in Pt/$TaO_{1.5}$(10 nm)/Ta_2O_5(10 nm)/Pt cells. In this thesis, the author focused on the RS characteristics in Fig. 4.9 because such RS characteristics have not been reported previously.

4.4.1 Control of resistive switching operation modes

Figure 4.11 shows various modes of RS characteristics when the range of voltage sweep is adjusted from the maximum magnitude of the negatively applied voltage (V_{nmax}) to +1.5 V. Panels (a)–(d) in Fig. 4.11 show a series of RS characteristics in different modes when V_{nmax} increases from −1.0 V [panel (a)] to −2.5 V [panel (d)] in increments of 0.5 V. Panels (i) and (ii) show the corresponding I–V and R–V characteristics, respectively. Set processes induced by a negative voltage (negative set), and reset processes induced by a positive voltage (positive reset), occur when V_{nmax} is −1.0 V, as shown in Panel (a) of Fig. 4.11. This RS operation mode is referred to as "counterclockwise RS" because the direction of the trace in the R–V plot is counterclockwise [18, 19]. Note that the resistance changes in the voltage sweep from −0.6 V to +1.5 V reflect the nonlinearity of the I–V characteristics with no accompanying transitions of the resistance state. In the clockwise RS mode, the dissolution and growth of the conductive filament occur near the TaO_x/Ta_2O_5 interface. Since the TaO_x/Ta_2O_5 interface forms an ohmic contact [17], the cell resistance in the 8-wise RS mode is dominated by the resistance of the conductive filament, resulting in the symmetry of the R–V characteristics with respect to the applied voltage from −0.6 V to +0.6 V. On the other hand, the direction of the trace of the R–V characteristics is clockwise when V_{nmax} is +2.5 V, as shown in Panel (d) of Fig. 4.11. This RS operation mode is referred to as "clockwise RS" [18, 19]. The cell resistance reaches approximately 3 kΩ at zero bias through the negative reset processes. The resistance changes in the voltage sweep from −2.0 V to +0.6 V reflect the nonlinearity of the I–Vcharacteristics in the clockwise RS mode. In the clockwise RS mode, the dissolution and growth of the conductive filament occur near the Ta_2O_5/Pt Schottky interface [20]. Therefore, the R–Vcharacteristics are asymmetric with respect to the applied voltage from −0.6 V to +0.6 V in the high resistance states due to the Schottky barrier at the Ta_2O_5/Pt interface. In the middle range of the applied voltage between the two aforementioned operation modes, when

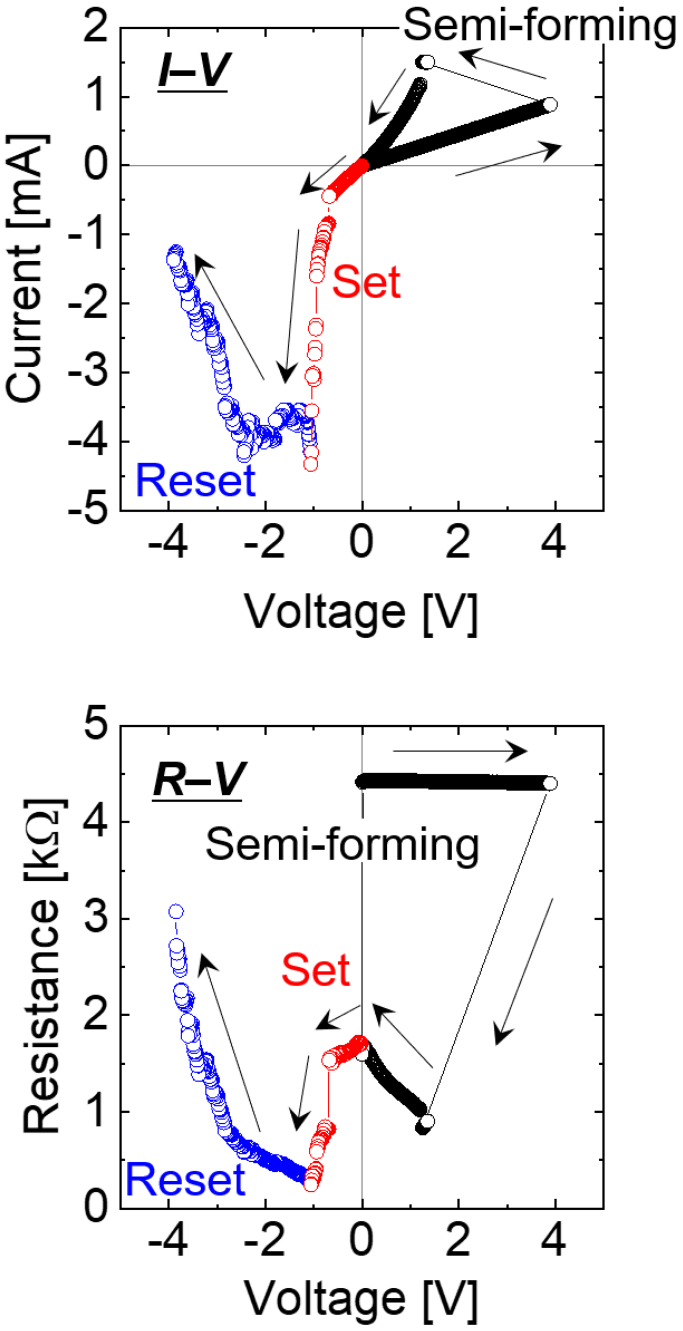

Figure 4.9: Typical RS characteristics when a negative voltage is applied to the top electrode (TE) after semi-forming in Pt/$TaO_{1.5}$(25 nm)/Ta_2O_5(10 nm)/Pt cells.

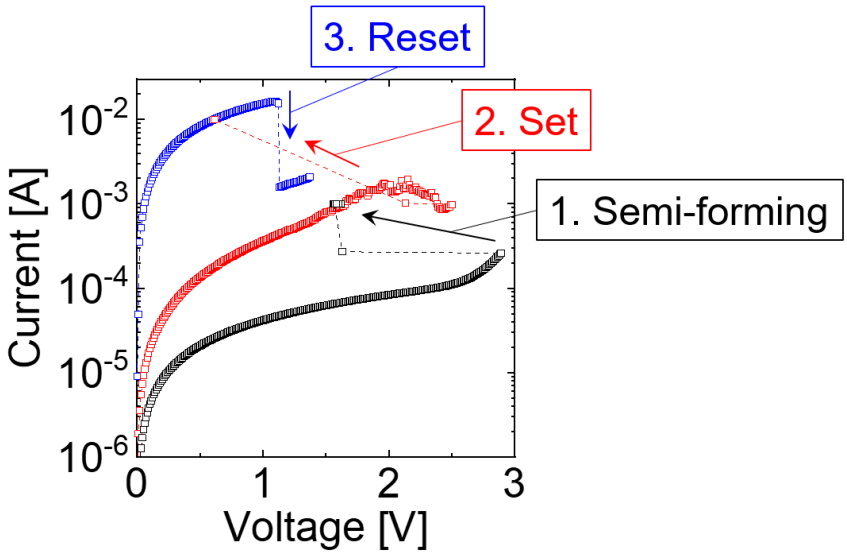

Figure 4.10: Typical unipolar RS characteristics when a positive voltage is applied to the TE after semi-forming in Pt/$TaO_{1.5}$(10 nm)/Ta_2O_5(10 nm)/Pt cells.

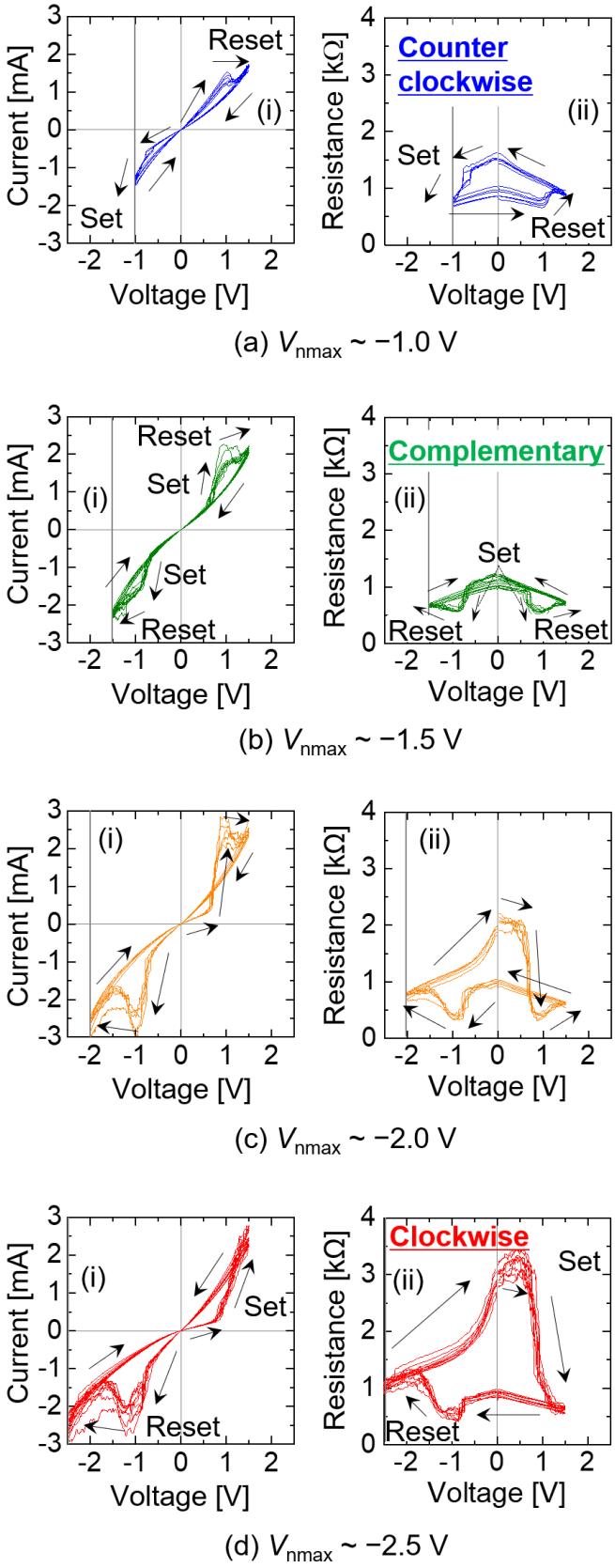

Figure 4.11: Various modes of RS characteristics in the range of voltage sweep from the maximum magnitude of the negatively applied voltage (V_{nmax}) to +1.5 V when V_{nmax} increases from −1.0 V panel (a) to −2.5 V panel (d) in increments of 0.5 V.

V_{nmax} is +1.5 V [Panel (b)], the complementary RS characteristics are obtained. Although the cell resistance decreases from 1.0 kΩ to 0.6 kΩ at approximately ±0.8 V because of the set processes, the subsequent reset processes from ±1.0 V to ±1.5 V result in an increase in the cell resistance up to a value similar to that before the previous set processes. The RS operation mode in the voltage range from −1.5 to +2.0 V [Panel (c)] is an intermediate mode between the complementary RS and the clockwise RS. Thus, the increase in V_{nmax} causes the increase in the cell resistance after applying a negative voltage in each RS mode from 0.8 kΩ to 3.0 kΩ, resulting in a change in the RS operation mode from the counterclockwise RS mode through the complementary RS mode to the clockwise RS mode. Although the values of V_{nmax} required for these principal RS operation modes slightly differ among the Pt/TaO_x/Ta_2O_5/Pt cells, it could be confirmed that the modification of the RS operation modes occurs in other cells as well. Moreover, in the case of the cells with a 10-nm-thick TaO_x layer after the semi-forming, similar RS characteristics to those in Fig. 4.11 could be observed. This systematic transition among the RS operation modes has not been reported in other related studies [21–25]. Notably, a particular mode of RS operations can be selectively obtained by controlling the applied-voltage range in the same cell.

4.4.2 Analog resistive switching

Here, the author discusses typical symmetric analog RS characteristics in the complementary RS mode, as shown in Panel (a) of Fig. 4.12. The positive set, the negative reset, the negative set, and the positive reset processes in the complementary RS mode are labeled as (b), (c), (e), and (d), respectively, in Panel (a). These RS characteristics can be individually obtained in the same cell. The maximum magnitude of the voltage sweep was gradually increased by ΔV_+ or ΔV_- each time a positive or negative voltage was swept, respectively. The cell resistance gradually changed with each voltage sweep at not only the reset processes but also the positive and negative set processes. The analog RS characteristics are more prominent in the complementary RS mode than in the counterclockwise and clockwise RS modes shown in Panels (a) and (d). Thus, analog RS irrespective of bias polarity was demonstrated in the complementary RS mode. Fig. 4.13 shows retention characteristics in 7 resistance states between 100 Ω and 1 kΩ when applying a voltage of +0.1 V at room temperature, indicating that little fluctuation of resistance was observed for about 1000 seconds in any resistance states.

An abrupt transition in the set processes is explained by a positive thermal feedback effect [4, 5]. Therefore, a pulse voltage or compliance current has been used to suppress Joule heating in many previous studies [6, 9, 12, 15, 24]. By contrast, the analog RS characteristics in the present study can be obtained during the DC voltage sweep, indicating that the competition between the growth and dissolution of a conductive filament is beneficial for analog RS even under the effect of Joule heating. Herein, because the V_Os are positively charged, they are assumed to move in the same direction as the electric field. Figure 4.14

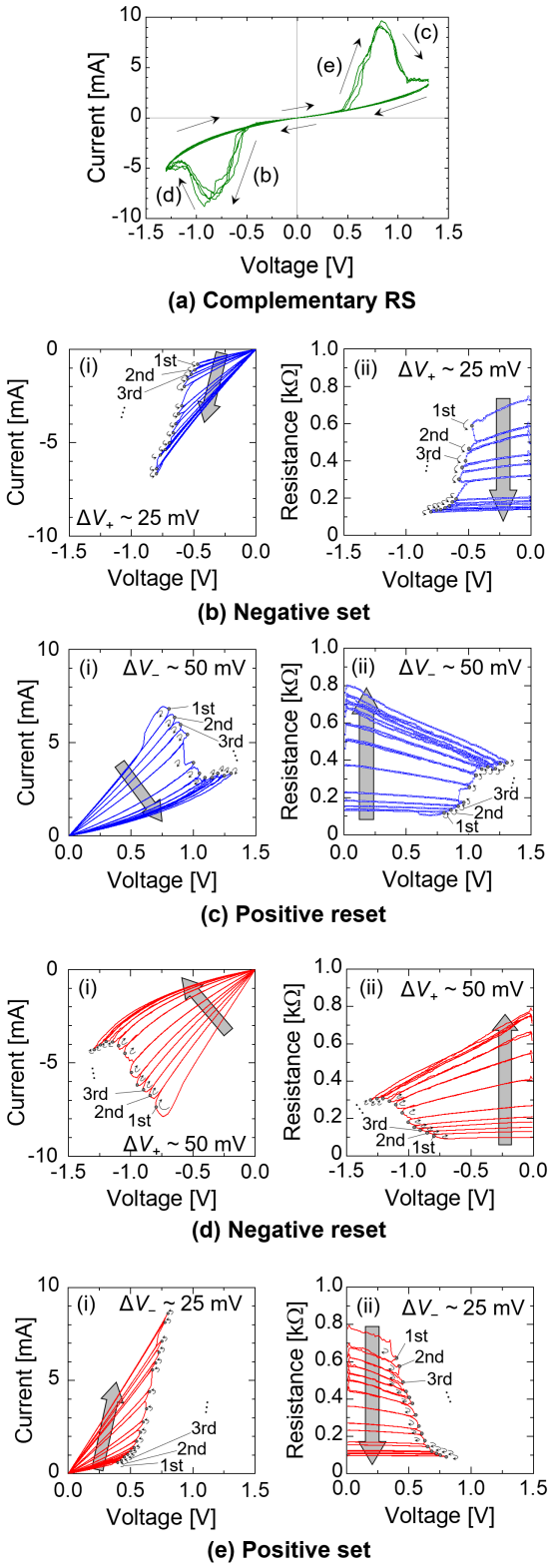

Figure 4.12: Symmetric analog RS characteristics in the complementary RS mode. The negative set, the positive reset, the positive set, and the negative reset processes in the complementary RS mode are labeled as (b), (c), (e), and (d), respectively, in Panel (a). The maximum magnitude of the voltage sweep was gradually increased by ΔV_+ or ΔV_- each time a positive or negative voltage was swept, respectively.

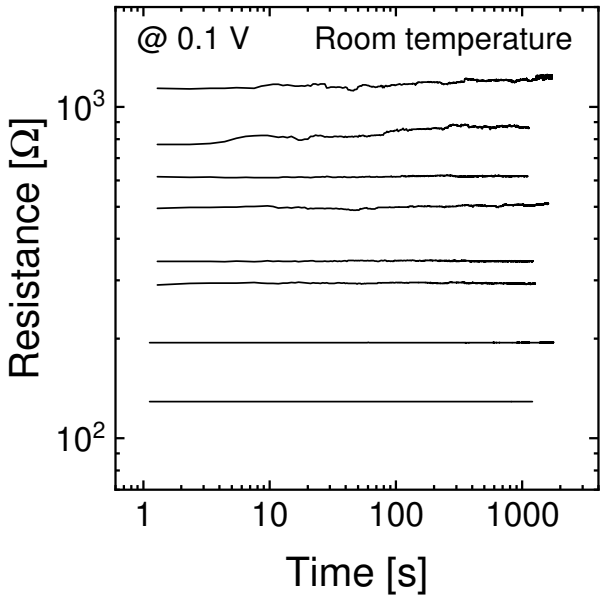

Figure 4.13: Retention characteristics in 7 resistance states between 100 Ωand 1 kΩwhen applying a voltage of +0.1 V at room temperature.

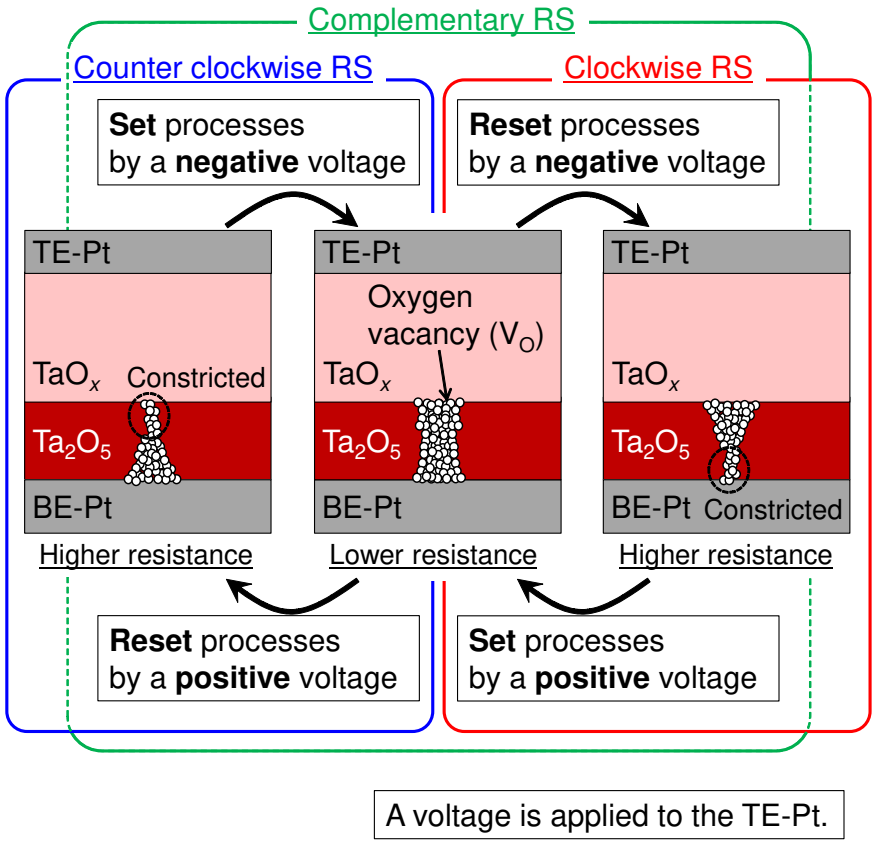

Figure 4.14: Schematics of a conductive filament in various RS operation modes.

shows schematics of a conductive filament in these RS operation modes. The positive set and the negative reset in the counterclockwise RS mode indicate the growth and dissolution of a conductive filament near the TaO_x layer, as shown in the left diagram in Fig. 4.14. Here, a conductive filament can be dissolved near the V_O reservoir layer for a negative reset because of a limited supply of V_Os to the Ta_2O_5 layer; this behavior is attributed to the TaO_x ($x \sim 1.5$) thin layer acting as a moderate V_O reservoir layer, [26] and not as an infinite V_O reservoir layer [27]. Furthermore, several recent studies have reported that oxygen exchange can occur between the Pt electrode and the oxide layer under an applied voltage [20, 28, 29]. Interestingly, the complementary RS characteristics are approximately symmetric with respect to the polarity of the applied voltage despite the asymmetric stacked structure, as shown in Panel (a) of Fig. 4.12. The symmetry of the RS characteristics may originate from the V_O supply by an oxygen exchange process between the Pt electrode and the Ta_2O_5 layer. The cell resistance after reset processes is lower than the inverse of the quantized conductance (12.9 kΩ) [30, 31], indicating that a conductive filament is not completely ruptured but constricted, as shown in the left diagram in Fig. 4.14. The negative reset and the positive set in the clockwise RS mode can be explained by the growth and dissolution of the conductive filament near the Pt BE, as shown in the right diagram in Fig. 4.14. The cycle of the negative set, the negative reset, the positive set, and the positive reset observed in the complementary RS mode suggests that reversible changes occur in the constricted region of the conductive filament in Fig. 4.14. The increase in V_{nmax} indicates that the constricted region moves from near the TaO_x layer toward the Pt BE, followed by further dissolution of the constricted filament near the Pt BE.

4.4.3 Reduction of operation current in analog resistive switching

Light blue lines in Fig. 4.15 show R–V characteristics of analog RS operations after the semi-forming when the oxygen composition and the thickness in the TaO_x layer are 1.81 and 50 nm, respectively. As shown by the blue lines in Fig. 4.15, when the magnitude of V_{nmax} increases to −3 V, a transition to a higher resistance state occurs. After the transition, analog RS operations in a higher resistance range can be obtained. Figure 4.16 shows R–V characteristics of analog RS operations in different resistance ranges when V_{nmax} is −2 V, −3 V, and −4 V. The resistance range of the analog RS operations depends on V_{nmax}. The increase in V_{nmax} could lead to a decrease in the density of V_Os constituting the conductive filaments because V_Os are driven to the TaO_x layer due to the electric field. Even though the negative applied voltage increased further, the cell resistance does not exceed R_{ini} because R_{ini} is contributed by the current in the entire area of the cell from the cell size dependence in Fig. 3.17 in Chap. 3. Therefore, a higher R_{ini} is preferable in terms of analog RS operations in a higher resistance range. Although R_{ini} and F_{semi} exhibit a trade-off relationship for the oxygen composition in the TaO_x layer, the trade-off

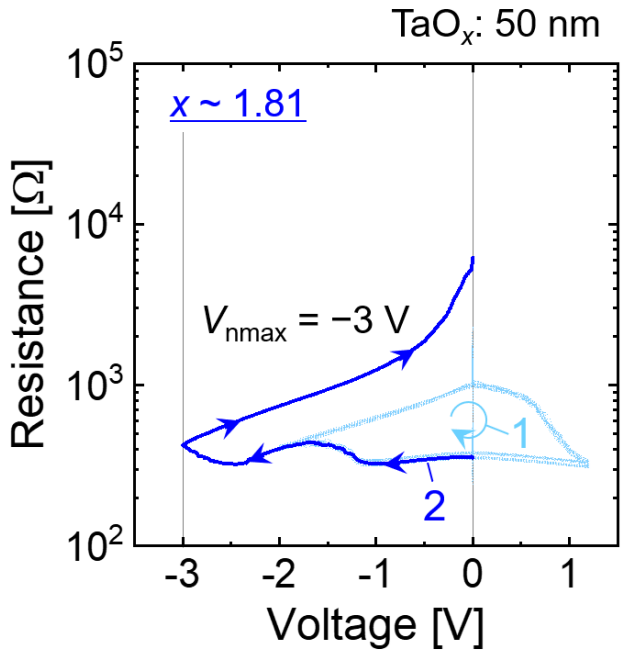

Figure 4.15: p

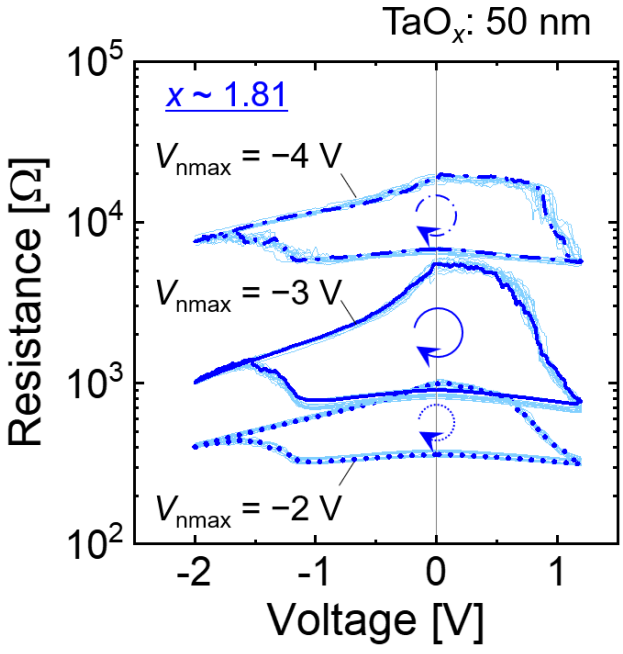

Figure 4.16: p

relationship can be improved by increasing the TaO_x thickness. The optimal conditions in this thesis to keep both R_{ini} and F_{semi} high values are the oxygen composition x of 1.81 and the TaO_x thickness of 50 nm. Compared to the resistance range of the analog RS operations at the oxygen composition x of 1.51 between 100 Ω and 1 kΩ in Fig. 4.12, the resistance range of the analog RS operations at the oxygen composition x of 1.81 is higher between 5 kΩ and 20 kΩ. These results demonstrated that operation currents in analog RS can be reduced to about 1/20 by controlling the oxygen composition x, the TaO_x thickness, and V_{nmax}.

4.5 Summary

Forming and resistive switching characteristics were investigated in detail for demonstration of analog RS characteristics in $Pt/TaO_x/Ta_2O_5/Pt$ cells. First, the author found a unique forming phenomenon (semi-forming) that transitions to a high-resistance state of several kilo-ohms. The dependence of semi-forming properties on the density of oxygen vacancies supplied from the TaO_x layer to the Ta_2O_5 layer was investigated, revealing that the semi-forming phenomenon is more likely to occur when more oxygen vacancies are supplied to the Ta_2O_5 layer. Based on these results, the mechanism of semi-forming was proposed. Second, the author also found that in $Pt/TaO_x/Ta_2O_5/Pt$ cells after semi-forming, set and subsequent reset processes occur when the negative applied voltage increases. Moreover, various operation modes of resistive switching can be controlled by adjusting the magnitude of the negative applied voltage: counterclockwise, complementary, and clockwise resistive switching. In particular, analog control of the cell resistance can be demonstrated even in set processes in the complementary resistive switching of $Pt/TaO_x/Ta_2O_5/Pt$cells. The author proposed a qualitative model for the origin of the analog resistive switching that the growth and dissolution in the identical filament in the Ta_2O_5 layer could suppress each other. Finally, by appropriately adjusting the oxygen composition x and thickness of the TaO_x layer, both the initial resistance and the relative occurrence frequency of the semi-forming were successfully controlled to relatively high values of 1 MΩ and 0.9,respectively, leading to establishing the method to reduce operation currents in analog resistive switching.

References

[1] A. Prakash, J. Park, J. Song, J. Woo, E. J. Cha, and H. Hwang, *IEEE Electron Device Letters* **36**, 32 (2015).

[2] D. Ielmini, *Semiconductor Science and Technology* **31**, 063002 (2016).

[3] W. Wu, H. Wu, B. Gao, N. Deng, S. Yu, and H. Qian, *IEEE Electron Device Letters* **38**, 1019 (2017).

[4] S. Yu, *Proceedings of the IEEE* **106**, 260 (2018).

[5] W. Zhang, B. Gao, J. Tang, X. Li, W. Wu, H. Qian, and H. Wu, *Physica Status Solidi - Rapid Research Letters* **13**, 1 (2019).

[6] J. Chen, C. Y. Lin, Y. Li, C. Qin, K. Lu, J. M. Wang, C. K. Chen, Y. H. He, T. C. Chang, S. M. Sze, and X. S. Miao, *IEEE Electron Device Letters* **40**, 542 (2019).

[7] S.-j. Li, B.-y. Dong, B. Wang, Y. Li, H.-j. Sun, Y.-h. He, N. Xu, and X.-s. Miao, *IEEE Transactions on Electron Devices* **66**, 810 (2019).

[8] S. Yu, Y. Wu, R. Jeyasingh, D. Kuzum, and H. S. Wong, *IEEE Transactions on Electron Devices* **58**, 2729 (2011).

[9] S. Ambrogio, S. Balatti, S. Choi, and D. Ielmini, *Advanced Materials* **26**, 3885 (2014).

[10] Y. Nishi, H. Sasakura, and T. Kimoto, *Journal of Applied Physics* **124**, 152134 (2018).

[11] T. Iwata, Y. Nishi, and T. Kimoto, *Thin Solid Films* **709**, 138203 (2020).

[12] S. Brivio, E. Covi, A. Serb, T. Prodromakis, M. Fanciulli, and S. Spiga, *Applied Physics Letters* **109**, 133504 (2016).

[13] E. Linn, R. Rosezin, C. Kügeler, and R. Waser, *Nature Materials* **9**, 403 (2010).

[14] Y. Yang, P. Sheridan, and W. Lu, *Applied Physics Letters* **100**, 203112 (2012).

[15] F. Nardi, S. Balatti, S. Larentis, D. C. Gilmer, and D. Ielmini, *IEEE Transactions on Electron Devices* **60**, 70 (2013).

[16] M. J. Lee, C. B. Lee, D. Lee, S. R. Lee, M. Chang, J. H. Hur, Y. B. Kim, C. J. Kim, D. H. Seo, S. Seo, U. I. Chung, I. K. Yoo, and K. Kim, *Nature Materials* **10**, 625 (2011).

[17] A. Schonhals, D. Wouters, A. Marchewka, T. Breuer, K. Skaja, V. Rana, S. Menzel, and R. Waser, *2015 IEEE 7th International Memory Workshop, IMW 2015*, 1 (2015).

[18] R. Waser, R. Dittmann, S. Menzel, and T. Noll, *Faraday Discussions* **213**, 11 (2019).

[19] S. Petzold, E. Miranda, S. U. Sharath, J. Muñoz-Gorriz, T. Vogel, E. Piros, N. Kaiser, R. Eilhardt, A. Zintler, L. Molina-Luna, J. Suñé, and L. Alff, *Journal of Applied Physics* **125**, 234503 (2019).

[20] H. Zhang, S. Yoo, S. Menzel, C. Funck, F. Cüppers, D. J. Wouters, C. S. Hwang, R. Waser, and S. Hoffmann-Eifert, *ACS Applied Materials and Interfaces* **10**, 29766 (2018).

[21] S. Balatti, S. Larentis, D. C. Gilmer, and D. Ielmini, *Advanced Materials* **25**, 1474 (2013).

[22] S. Brivio, J. Frascaroli, and S. Spiga, *Applied Physics Letters* **107**, 023504 (2015).

[23] A. Schönhals, J. Mohr, D. J. Wouters, R. Waser, and S. Menzel, *IEEE Electron Device Letters* **38**, 449 (2017).

[24] S. U. Sharath, S. Vogel, L. Molina-Luna, E. Hildebrandt, C. Wenger, J. Kurian, M. Duerrschnabel, T. Niermann, G. Niu, P. Calka, M. Lehmann, H. J. Kleebe, T. Schroeder, and L. Alff, *Advanced Functional Materials* **27**, 1700432 (2017).

[25] C. La Torre, A. F. Zurhelle, T. Breuer, R. Waser, and S. Menzel, *IEEE Transactions on Electron Devices* **66**, 1268 (2019).

[26] S. Kim, S. Choi, and W. Lu, *ACS Nano* **8**, 2369 (2014).

[27] F. Cüppers, S. Menzel, C. Bengel, A. Hardtdegen, M. V. Witzleben, U. Böttger, and R. Waser, *APL Materials* **091105**, 091105 (2020).

[28] A. Schönhals, C. M. Rosário, S. Hoffmann-Eifert, R. Waser, S. Menzel, and D. J. Wouters, *Advanced Electronic Materials* **4**, 1700243 (2018).

[29] D. Cooper, C. Baeumer, N. Bernier, A. Marchewka, C. La Torre, R. E. Dunin-Borkowski, S. Menzel, R. Waser, and R. Dittmann, *Advanced Materials* **29**, 1700212 (2017).

[30] H. Sasakura, Y. Nishi, and T. Kimoto, *Applied Physics Letters* **107**, 2 (2015).

[31] Y. Nishi, H. Sasakura, and T. Kimoto, *Journal of Materials Research* **32**, 2631 (2017).

Chapter 5

Effects of Joule Heating on Oxygen Vacancy Transport in $Pt/TaO_x/Ta_2O_5/Pt$ Cells

5.1 Introduction

As mentioned in Chap. 1, it is difficult to experimentally observe the growth and dissolution processes of conductive filaments (CFs) because the growth and dissolution processes occur in an unpredictable localized spot (a diameter of a few nano-meters) and in ultra-thin oxide films (∼10 nm) [1–3]. Therefore, the mechanism of the growth and dissolution processes of the CFs, in other words, transport properties of oxygen vacancies (V_Os) in the oxide films during resistive switching (RS) operations has not been clarified.

The author focused on Joule heating generated in the filament because its effects on the transport properties of V_Os in $Pt/TaO_x/Ta_2O_5/Pt$ cells can be investigated with both experimental and theoretical approaches. As for the experimental approach, local Joule heating was observed on the surface of $Pt/TaO_x/Ta_2O_5/Pt$ cells during forming and RS operations. As for the theoretical approach, a coupled simulation of electric potential distribution, temperature distribution, and V_O concentration distribution during a reset process in $Pt/TaO_x/Ta_2O_5/Pt$ cells was performed. Since Joule heating is believed to have significant effects on Fick diffusion due to the gradient of V_O concentration, which is considered to be one of the dominant driving forces for V_O transport during the dissolution of the CFs [4–14], in this study, the author especially aimed to elucidate V_O transport properties during analog reset processes.

5.2 Experimental observation of local Joule heating

In this section, the author performed the *in-situ* measurement of temperature distribution on the surface of $Pt/TaO_x/Ta_2O_5/Pt$ cells during RS operations using an infrared detector

to reveal a local position at which Joule heating is generated and transient characteristics of temperature at the local spot.

5.2.1 Experimental methods

First, based on the results in Chap. 4, Pt(15 nm)/TaO_x(40 nm)/Ta_2O_5(10 nm)/Pt(60 nm) cells were fabricated on a SiO_2/Si substrate under the optimal condition that the TaO_x and Ta_2O_5 layers were deposited at the oxygen gas flow rate of 1.0 sccm and 2.0 sccm, respectively, where semi-forming is more likely to occur and initial resistance is higher. Figure 5.1 shows a schematic illustration of the measurement system including an infrared detector. The resolution of this microscope is approximately 3 μm because the system detects infrared wavelengths (3-–5 μm) [15–17]. The sample stage was heated to 50°C to improve the signal-to-noise ratio of the measurement. When a voltage is applied to the Pt top electrode (TE) of the RS cells with the Pt bottom electrode (BE) grounded using a semiconductor parameter analyzer (Agilent 4156C), current flows through CFs in the Ta_2O_5 layer during RS operations, generating Joule heating in the CFs. The Joule heating is transferred to the Pt TE by thermal conduction. The temperature increment at the surface of the Pt TE was measured by detecting infrared radiation using an InSb detector (InfraScope MWIR temperature mapping microscope, Quantum Focus Instruments Co.). The infrared radiation is emitted primarily from the surface of the Pt TE [17]. A ramp rate of voltage sweep is about 0.2 V/s, and compliance current (I_{comp}) in the forming operations was set at 1 mA.

5.2.2 Temperature distribution in forming and resistive switching operations

Figure 5.2 shows current–voltage (I–V) characteristics in semi-forming processes and temperature mapping images for the corresponding RS cells. At the moment of current rise during a forming process, in each RS cell, temperature increment can be locally observed at different spots excluding the edge of the cell. Although the maximum temperatures have several variations, the local maximum temperatures were 50–90°C. These results suggest that a single conductive filament (CF) is locally formed at the semi-forming.

Figure 5.3 (a)–(c) show I–V characteristics in a semi-forming process, a temperature mapping image at the maximum temperature for the corresponding RS cell, and transient characteristics of temperature at the local heated spot and the introduced power. At the semi-forming, the temperature at the local spot rises rapidly, as shown in Fig. 5.3 (c), while the introduced power decreases abruptly. As shown in Fig. 3.17, there is a positive correlation between initial conductance and cell size, indicating that current flows throughout the entire Pt/TaO_x/Ta_2O_5/Pt cell before the semi-forming. In contrast, after the semi-forming, current flows in the local region of the CF. Therefore, as shown in Fig. 5.3, although the

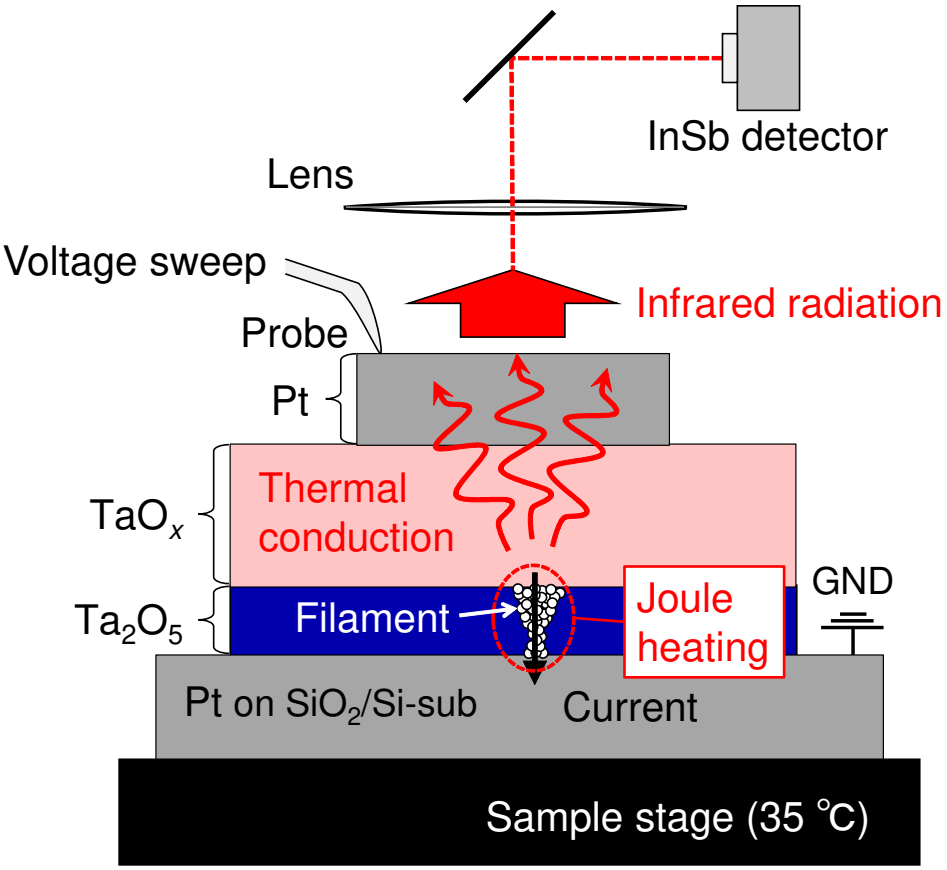

Figure 5.1: A schematic illustration of the *in-situ* measurement system of temperature distribution on the surface of Pt/TaO_x/Ta_2O_5/Pt cells during RS operations using an infrared detector.

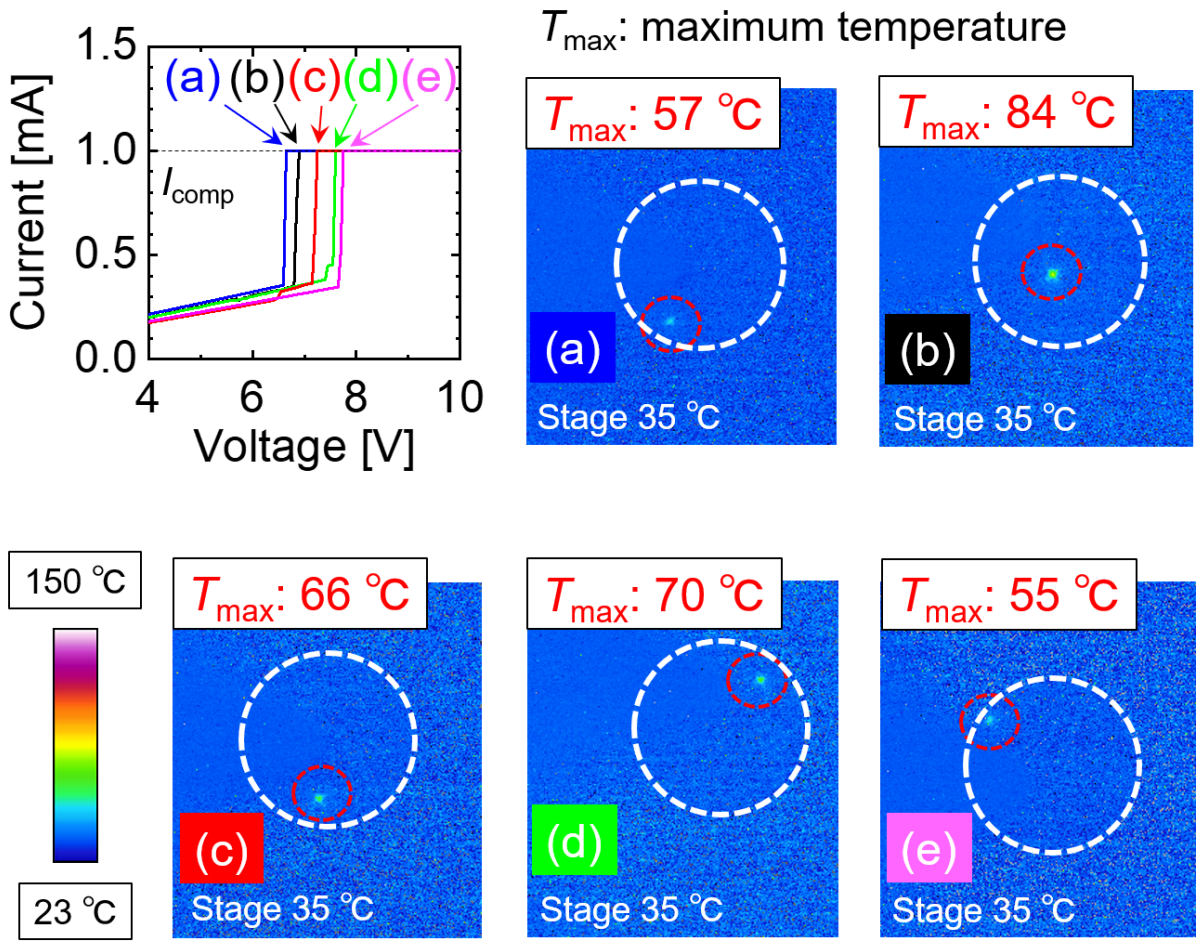

Figure 5.2: Current–voltage (I–V) characteristics in semi-forming processes and temperature mapping images for the corresponding RS cells.

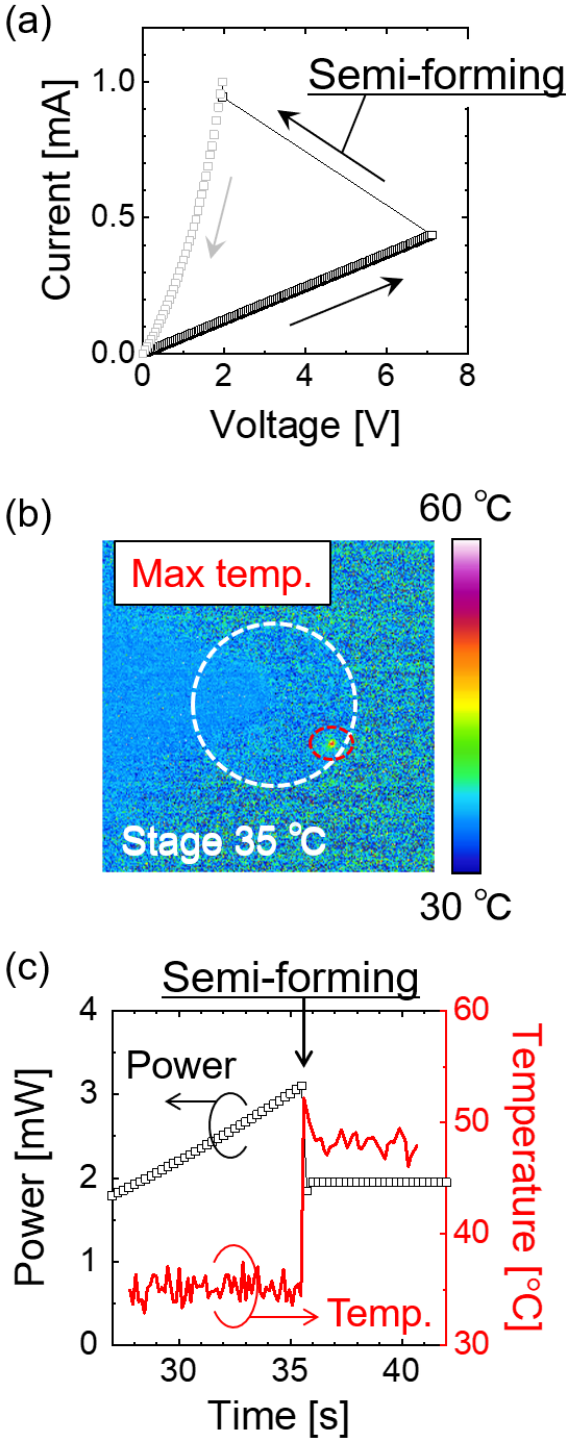

Figure 5.3: (a) I–V characteristics in a semi-forming process. (b) A temperature mapping image at the maximum temperature for the corresponding RS cell. (c) Transient characteristics of temperature at the local heated spot and introducing power.

introduced power decreases at the semi-forming because the applied voltage is reduced due to the decrease in the cell resistance, the introduced power per unit area significantly increases in the local region of the CF formed at the semi-forming. For this reason, in the semi-forming process, the outline of transient characteristics of the local temperature is not consistent with that of the introduced power.

For the same cell shown in Fig. 5.3, transient characteristics during RS operations in various RS modes were evaluated in the same way. Figure 5.4 (a)–(c) show I–V characteristics when applying a negative voltage after the semi-forming process, a temperature mapping image at the maximum temperature, and transient characteristics of the local temperature and the introduced power. The local temperature rose rapidly at the identical spot as at the semi-forming when the cell resistance decreased at about -1 V (4.0 s). Then, when the introduced power reached a maximum at about -3 V (13.5 s), the local temperature also reached the maximum value of 85°C. As the magnitude of the negative applied voltage increased further from -3 V to -6 V, the local temperature fell down with the increase in the cell resistance from 13.5 s to 20 s. Figure 5.5 and Figure 5.6 show I–V characteristics when applying negative and positive voltages in the complementary RS mode, temperature mapping images at the maximum temperature, and transient characteristics of the local temperature and the introduced power. Moreover, Figure 5.7 and Figure 5.8 show I–V characteristics when applying negative and positive voltages in the counterclockwise RS mode, temperature mapping images at the maximum temperature, and transient characteristics of the local temperature and the introduced power. During various RS operations except for the semi-forming process, the outline of transient characteristics of the local temperature is consistent with that of the introduced power, which means that most current flows in the local region of the CF. In addition, interestingly, the local heated spot was identical for various RS modes in the single Pt/TaO_x/Ta_2O_5/Pt cell. Furthermore, when the cell resistance abruptly decreased, the local temperature tended to increase rapidly.

Similarly, transient characteristics during analog RS operations were investigated in another Pt/TaO_x/Ta_2O_5/Pt cell, as shown in Figure 5.9 and Figure 5.10. Also in analog RS operations, the outline of transient characteristics of the local temperature is consistent with that of the introduced power. Both when the cell resistance decreases (set) and increases (reset), the local heated spot was identical in the Pt/TaO_x/Ta_2O_5/Pt cell. During an analog set operation, the local temperature rose gradually, indicating that the rapid temperature rise was successfully suppressed.

5.2.3 Discussion

In this section, the author discusses the growth and dissolution processes of the CF, based on the semi-forming mechanism proposed in Chap. 4 and the experimental results obtained in Chap. 5. As shown in Fig. 4.8, the semi-forming can be understood as a phenomenon that a conductive filament (CF) with a gap formed in the V_O-poor region of the Ta_2O_5 layer

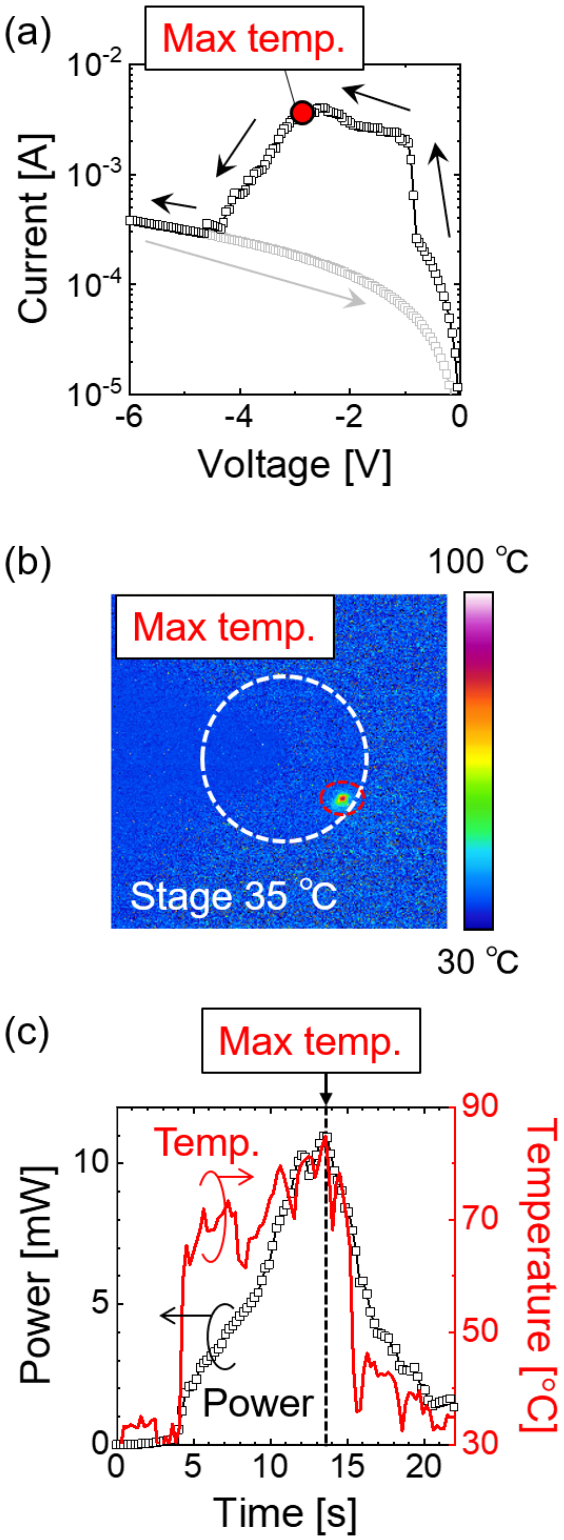

Figure 5.4: (a) I–V characteristics when applying a negative voltage after the semi-forming process. (b) A temperature mapping image at the maximum temperature. (c) Transient characteristics of the local temperature and the introducing power.

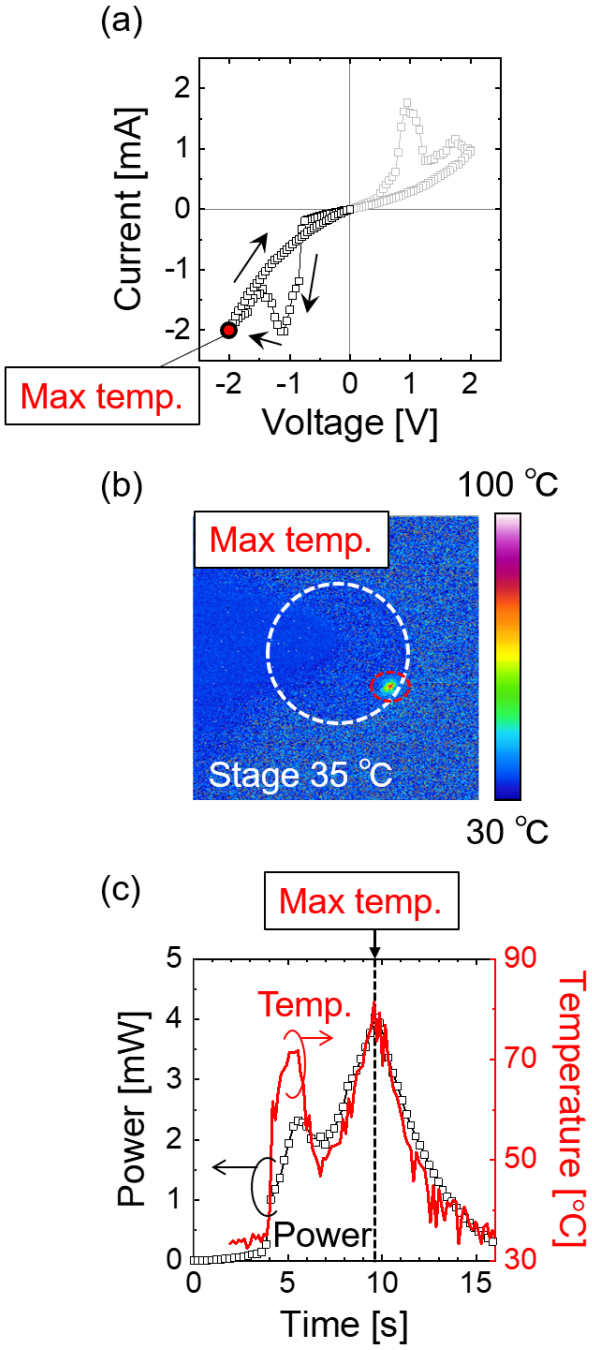

Figure 5.5: (a) I–V characteristics when applying a negative voltage in the complementary RS mode. (b) A temperature mapping image at the maximum temperature. (c) Transient characteristics of the local temperature and the introducing power.

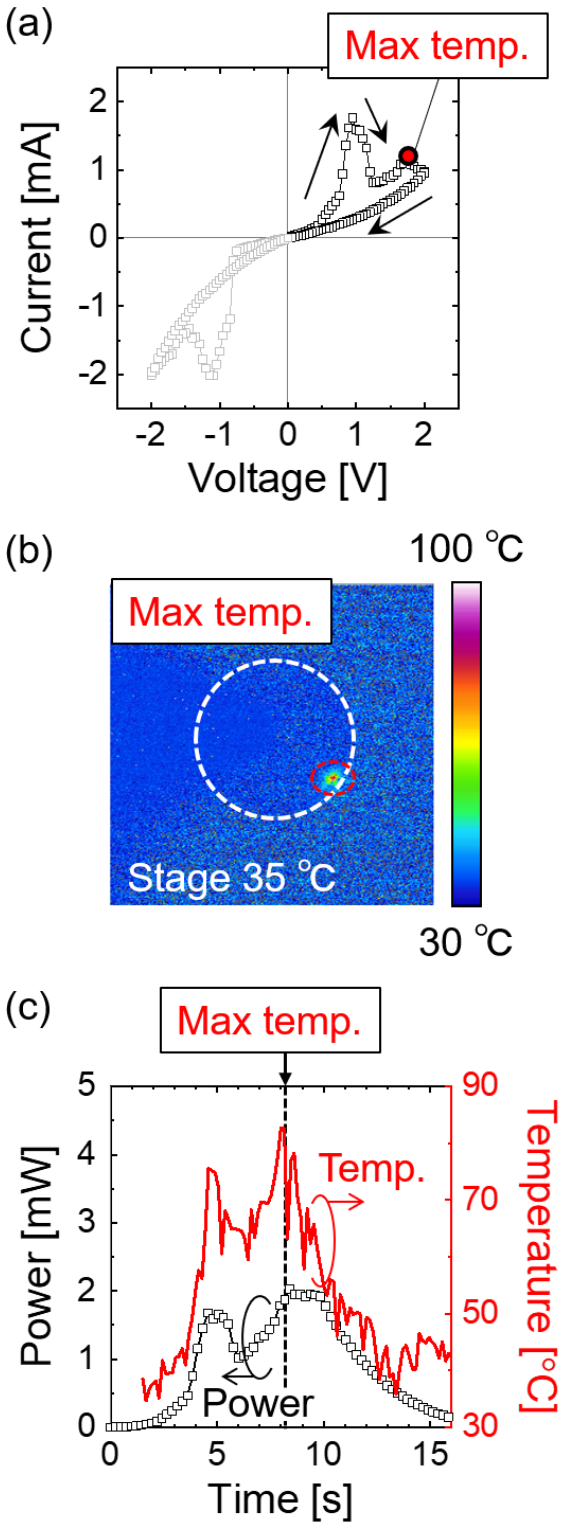

Figure 5.6: (a) I–V characteristics when applying a positive voltage in the complementary RS mode. (b) A temperature mapping image at the maximum temperature. (c) Transient characteristics of the local temperature and the introducing power.

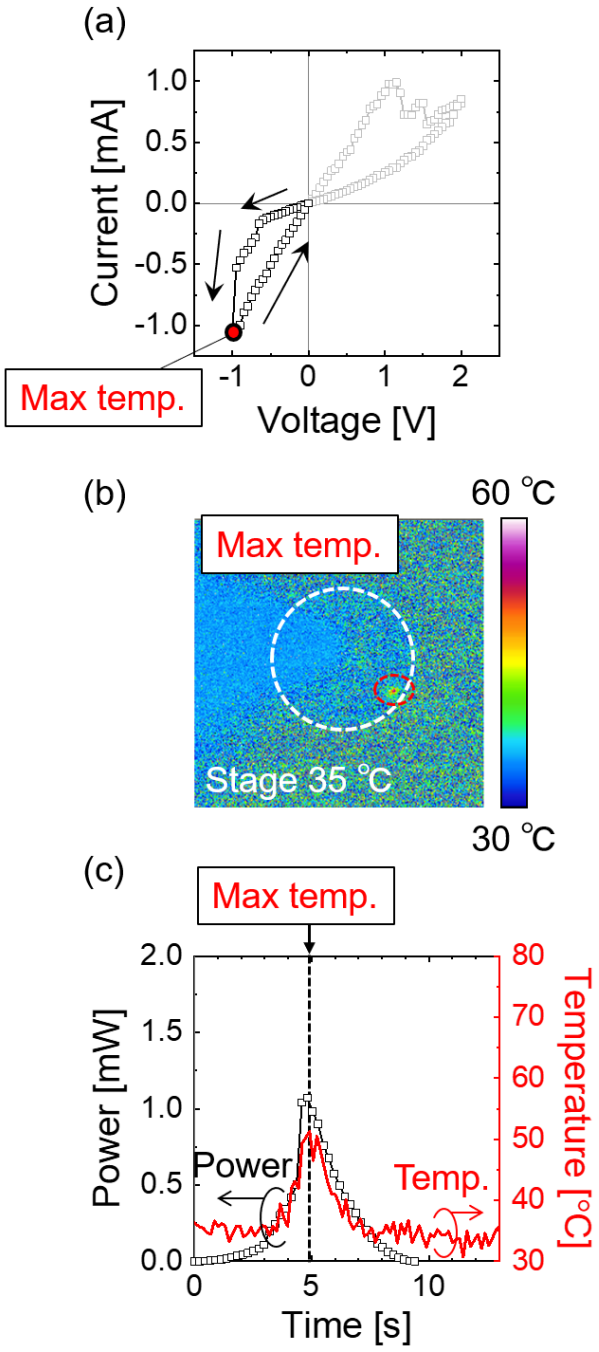

Figure 5.7: (a) I–V characteristics when applying a negative voltage in the counter clockwise RS mode. (b) A temperature mapping image at the maximum temperature. (c) Transient characteristics of the local temperature and the introducing power.

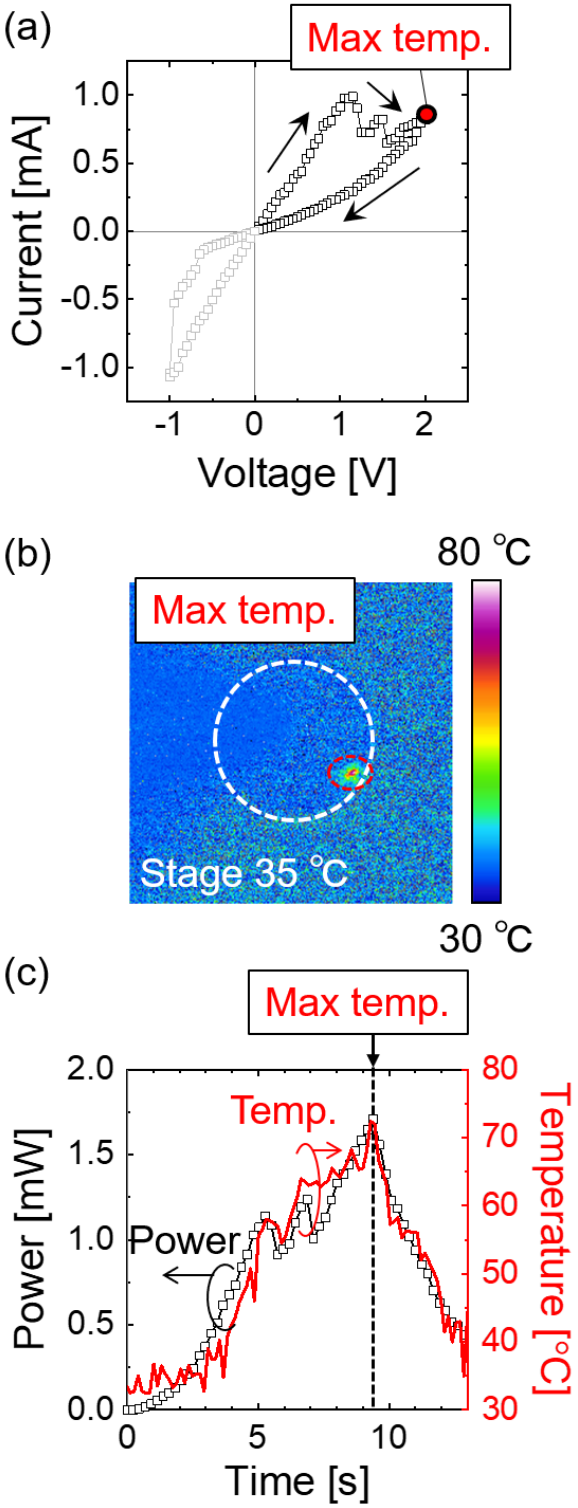

Figure 5.8: (a) I–V characteristics when applying a positive voltage in the counter clockwise RS mode. (b) A temperature mapping image at the maximum temperature. (c) Transient characteristics of the local temperature and the introducing power.

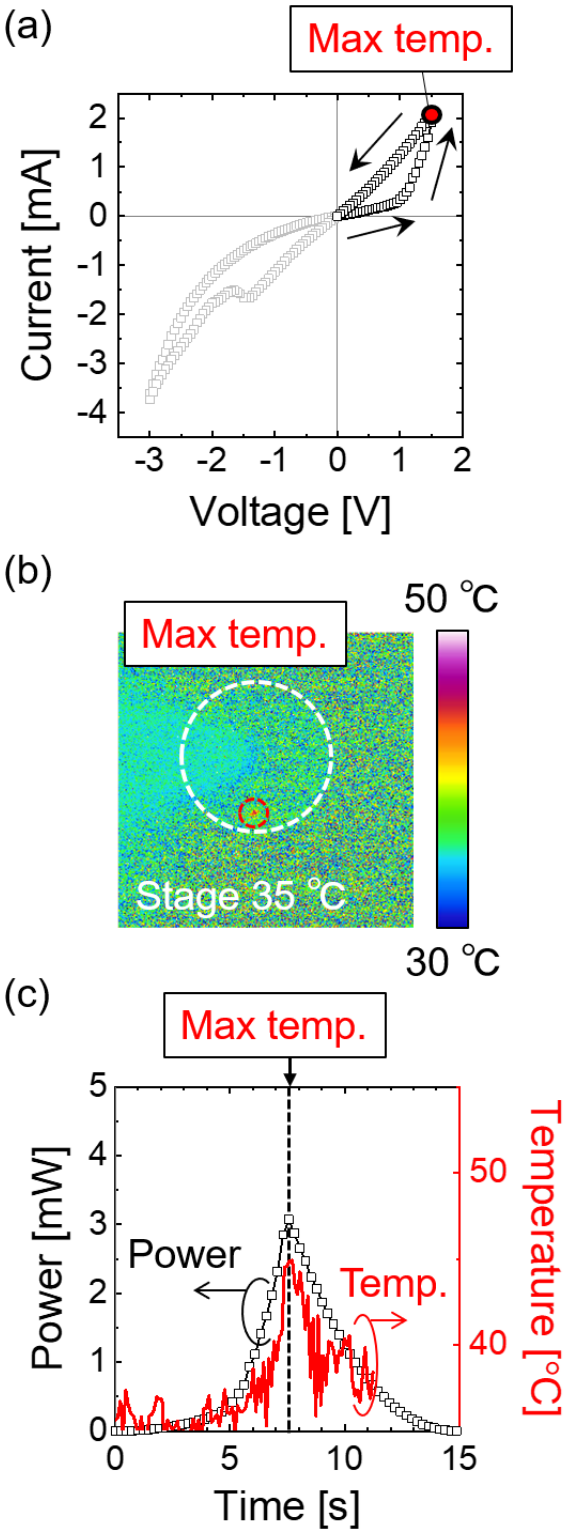

Figure 5.9: (a) I–V characteristics when applying a positive voltage in an analog set process. (b) A temperature mapping image at the maximum temperature. (c) Transient characteristics of the local temperature and the introducing power.

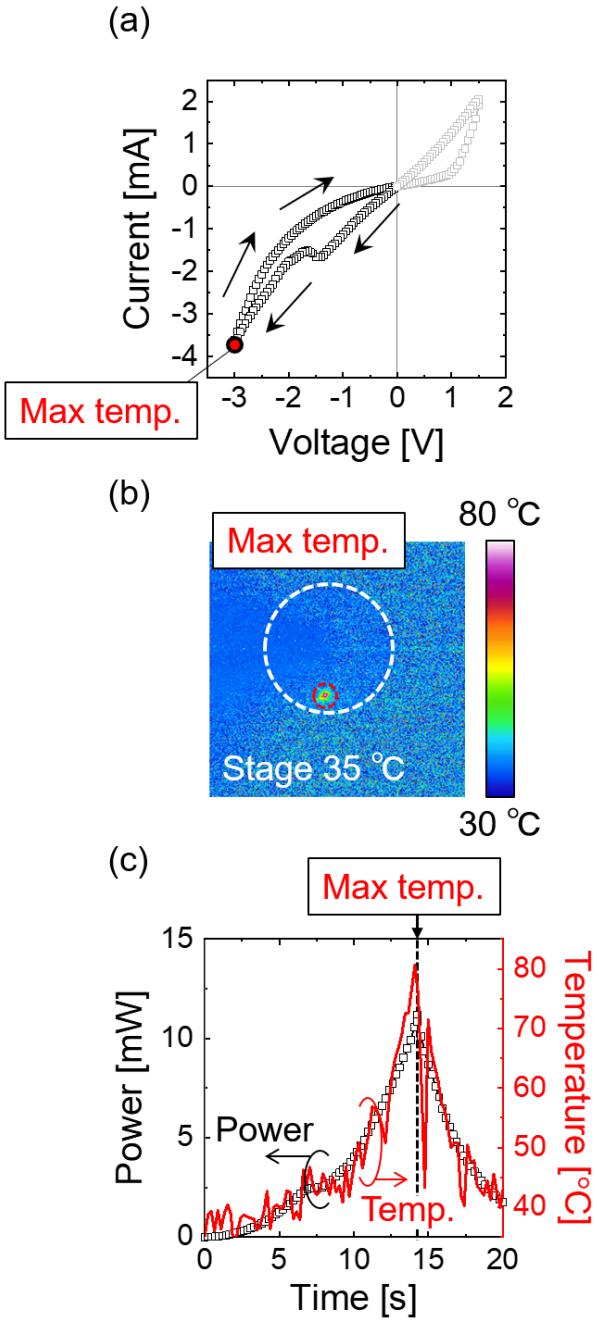

Figure 5.10: (a) I–V characteristics when applying a negative voltage in an analog reset process. (b) A temperature mapping image at the maximum temperature. (c) Transient characteristics of the local temperature and the introducing power.

due to the local Joule heating. This model is consistent with the local temperature rise at a single spot in the semi-forming process, which was experimentally observed in this section.

The result that a local heated spot was identical for various RS modes in a single $Pt/TaO_x/Ta_2O_5/Pt$ cell suggests that the growth and dissolution processes of the CF occur in the identical region of the $Pt/TaO_x/Ta_2O_5/Pt$ cell when a negative voltage applied.

5.3 Theoretical analyses of Joule heating effects on oxygen vacancy transport

In this section, the author performed a coupled simulation of temperature distribution, electric potential distribution, and V_O concentration distribution during a reset process in $Pt/TaO_x/Ta_2O_5/Pt$ cells to elucidate V_O transport properties during analog reset processes.

5.3.1 Simulation details and parameter determination

The growth and dissolution processes of the CFs could be described by self-consistently solving three partial differential equations (PDEs) using the finite element method [18–20]: a Heat equation for thermal conduction,

$$k\nabla^2 T + \sigma|\nabla V|^2 = \rho C_\mathrm{p}\frac{\partial T}{\partial t}, \tag{5.1}$$

a current continuity equation for electrical conduction,

$$\nabla \cdot (\sigma \nabla V) = 0, \tag{5.2}$$

a drift/diffusion equation for V_O transport,

$$\frac{\partial c}{\partial t} = \nabla \cdot (cD_{V_O}S_{\mathrm{Soret}} + c\mu_{V_O}\nabla V + D_{V_O}\nabla c). \tag{5.3}$$

These three PDEs were self-consistently solved using a numerical solver (COMSOL Multiphysics) to calculate distributions of temperature T, electrostatic potential V, and V_O concentration c. In particular, V_Os are driven by the following three factors: thermal diffusion due to the gradient of temperature, V_O drift due to the gradient of electric potential, and V_O diffusion due to the gradient of V_O concentration, which are represented by the first, second, and third terms on the right side of Eq. (5.3), respectively [20, 21].

For simplicity, the cell structure, including the surrounding atmosphere, was defined in an axisymmetric two-dimensional cylindrical coordinate with radial coordinate r and vertical coordinate z, as shown in Fig. 5.11. Here, only the domains directly below the top electrode with a diameter of 100 μm were defined, ignoring electric potential spread. To verify the electric field spread, the author simulated the distributions of electric potential and electric field in $Pt/TaO_x/Ta_2O_5/Pt$ cells in Appendix B. In Fig. 5.11, the domains,

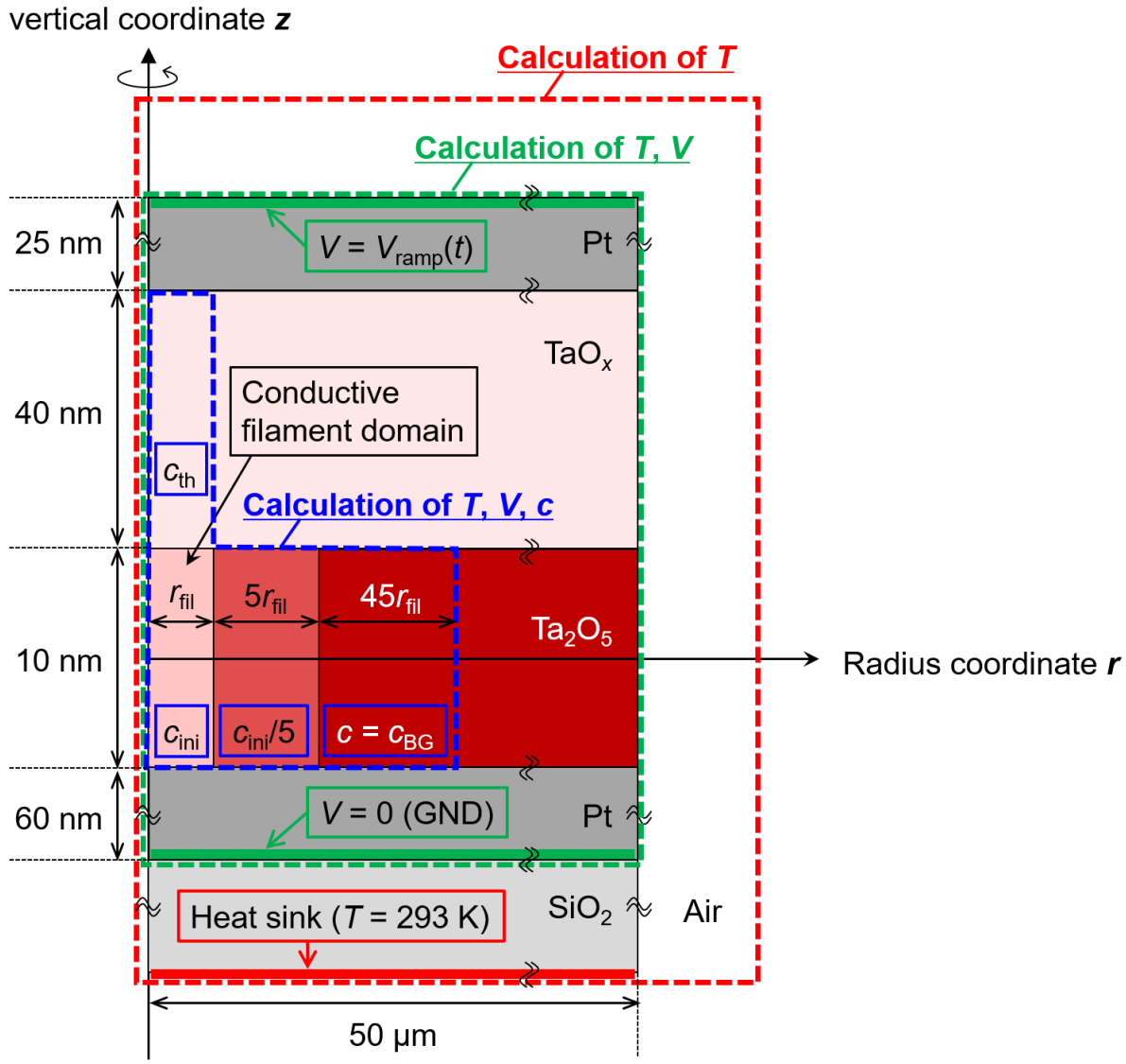

Figure 5.11: Cell structure including the surrounding atmosphere in an axisymmetric two-dimensional cylindrical coordinate with radial coordinate r and vertical coordinate z. The domains, where the heat equation, the current continuity equation, and the drift/diffusion equation were calculated, are indicated by red, green, and blue dashed lines. The initial values in Eqs. (5.1)–(5.3) are also given.

where the heat equation, the current continuity equation, and the drift/diffusion equation were calculated, are indicated by red, green, and blue dashed lines. First, the heat equation was calculated in the whole system including the surrounding atmosphere. The bottom of the SiO_2 was assumed to be an ideal heat sink, and so the boundary condition for Eq. (5.1) was $T = T_0$, where T_0 is room temperature (293 K). The other boundaries were assumed to be thermally insulated. The initial value of temperature in all domains was also set to $T = T_0$. Second, the current continuity equation was calculated in the top and bottom Pt electrodes and the domains sandwiched between these Pt electrodes. The boundary conditions for Eq. (B.1) are $V = 0$ (grounded) and $V = V_{\mathrm{ramp}}(t)$ at the bottom and top electrodes, respectively. The ramp rate and the maximum magnitude of the voltage sweep were set to 0.2 V/s and −0.45 V. The initial value of potential in all calculated domains was set to $V = 0$. Finally, the drift/diffusion equation was calculated in the domain where the initial value of V_O concentration was defined as a higher value (conductive filament domain), and in the surrounding domains. At all boundaries, it was assumed that there was no flux of V_O due to the V_O diffusion for Eq. (5.3). For the convergence of the calculations, no boundary conditions were set for the V_O flux due to thermal diffusion and V_O drift.

Based on the results obtained in Chap. 3, the initial value of V_O concentration and the conductivity of Ta oxide depending on V_O concentration were determined as follows. First, from the results shown in Fig. 3.10, it was assumed that the conductivity of the Ta_2O_5 layer is dominated by the band conduction above room temperature, and is expressed by

$$\sigma(T, c) = \sigma_0(c)\exp\left[-\frac{E_{\mathrm{a}}(c)}{k_{\mathrm{B}}T}\right], \tag{5.4}$$

$$E_{\mathrm{a}}(c) = 0.23\ \mathrm{eV} - (5.6 \times 10^{-8}\ \mathrm{eV \cdot cm}) \cdot c^{\frac{1}{3}}. \tag{5.5}$$

Here, Eq. (5.5) has been obtained from the results of Fig. 3.13 in Chap. 3, assuming that V_O concentration is equal to 0.1 eV·N_{F}. Figure 5.12 shows the relationship between the activation energy E_{a} and V_O concentration calculated by Eq. (5.5). Next, the threshold V_O concentration c_{th} is defined at a V_O concentration of 6.9×10^{19} cm^{-3}, where $E_{\mathrm{a}} = 0$. Thus, the conductivity of the Ta_2O_5 layer $\sigma(T, c)$ depends on V_O concentration c, as shown in Table 5.1. As for σ_0, it was assumed to vary linearly from the conductivity of stoichiometric Ta_2O_5 (3.7×10^{-9} S/m) to that of metallic Ta (7×10^{6} S/m) depending on V_O concentration c. The initial values of V_O concentration in the domains of the conductive filament (c_{ini}), surrounding the conductive filament, above the conductive filament, and the others (c_{BG}) were $c_{\mathrm{th}}/5$, $c_{\mathrm{th}}/25$, c_{th}, and $c_{\mathrm{th}}/4 \times 10^5$, respectively, as shown in Fig. 5.11. Note that the domain surrounding the conductive filament (r = 5–25 nm) was defined as a domain that relaxes the large difference between the initial values of V_O concentration, c_{ini} and c_{BG}, for the convergence of the calculations. Using the above assumptions and initial values, the author comprehensively calculated the Ta oxide conductivity depending on V_O concentration c and temperature T in the domain including the conductive filament indicated by the blue dashed line in Fig. 5.11.

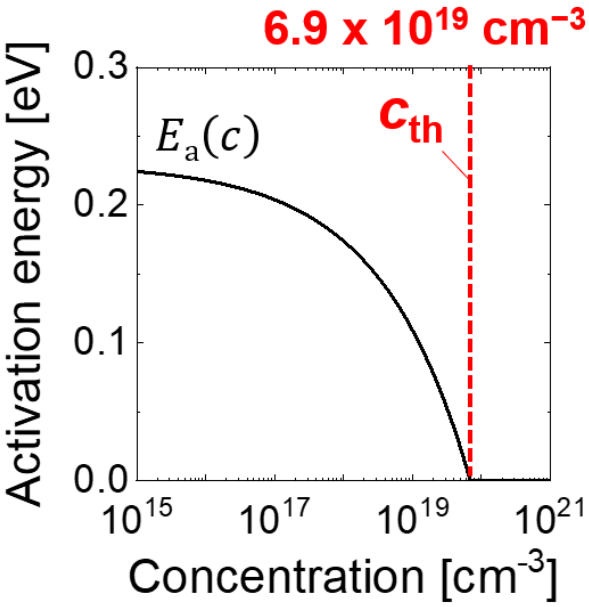

Figure 5.12: The relationship between the activation energy E_a and V_O concentration calculated by Eq. (5.5).

Table 5.1: Expression for the activation energy $E_a(c)$, the conductivity of the Ta_2O_5 layer, and the coefficient of the conductivity, depending on V_O concentration c and temperature T.

	$0 < c < c_{th}$	$c_{th} < c$
	semiconductor-like	metal-like
$E_a(c)$	Eq. (5.5)	0
$\sigma(T,c)$	$\sigma_0(c)\exp\left[-\frac{E_a(c)}{k_B T}\right]$	$\sigma_0(c)$
$\sigma_0(c)$	$\sigma_{Ta} \cdot c/c_{th} + \sigma_{Ta2O5}$	σ_{Ta}

$\sigma_{Ta2O5} = 3.7 \times 10^{-9}$ S/m, $\sigma_{Ta} = 7 \times 10^{6}$ S/m

5.3.2 Distribution of temperature and oxygen vacancies in resistive switching operations

Figure 5.13 shows the experimental and calculation results of I–V characteristics. As for the experimental results, the maximum local temperature obtained in Sec. 5.2 is also shown for reference. Although the absolute values of current and voltage are slightly different, as a result of the calculation, analog reset characteristics similar to the experimental results were obtained. Next, Fig. 5.14(b) shows the distribution of the conductivity before and after the reset process. The results indicate that the reset process is caused by the decrease in the conductivity above the center of the Ta_2O_5 layer. The conductivity distribution is attributed to the distribution of V_O concentration, corresponding to the geometry of the conductive filament. Fig. 5.14(c) shows transient characteristics of the distribution of temperature T and V_O concentration c in the analog reset process. Regarding the temperature distribution, temperature significantly rises at the center of the conductive filament as the magnitude of the negative voltage increases. At the maximum magnitude of the negative applied voltage, the temperature at the center of the conductive filament reaches a maximum value of about 450 °C. After that, the temperature drops to room temperature. Fig. 5.15 shows the temperature distribution including the Pt surface of the $Pt/TaO_x/Ta_2O_5/Pt$ cell when the center of the conductive filament reaches the maximum temperature (t =2.25 s). At this time, the temperature of the Pt surface also reaches its maximum of about 90 °C, which is consistent with the experimental result that the Pt surface temperature reaches about 80 °Cin the analog reset processes, as shown in Fig. 5.13 or Fig. 5.10. Regarding the V_O concentration distribution, the conductive filament dissolves near the TaO_x layer in the Ta_2O_5 layer as the magnitude of the negative voltage increases. After the maximum magnitude of the negative applied voltage, the V_O concentration distribution exhibits little change when the magnitude of the negative voltage decreases, and the constriction of the conductive filament is preserved.

5.3.3 Driving force of oxygen vacancy transport

As mentioned in Sec. 5.3.1, the V_O concentration distributions shown in Fig. 5.14(c) were calculated by Eq. (5.3) for the V_O transport. The first, second, and third terms on the right side of Eq. (5.3) represent the contributions of thermal diffusion due to the gradient of temperature, V_O drift due to the gradient of electric potential, and V_O diffusion due to the gradient of V_O concentration, respectively. The author calculated the components of V_O flux contributed by these three terms on the right side of Eq.(5.3), $F_{\mathrm{Heat-diffusion}}$, $F_{\mathrm{Vo-drift}}$, and $F_{\mathrm{Vo-diffusion}}$, to reveal dominant driving forces for V_O transport. Figure 5.16 shows V_O flux vectors on the V_O distribution when the center of the conductive filament reaches the maximum temperature (t =2.25 s), where F_{tot} is the sum of $F_{\mathrm{Heat-diffusion}}$, $F_{\mathrm{Vo-drift}}$, and $F_{\mathrm{Vo-diffusion}}$. In Fig. 5.16 (a), F_{tot}, $F_{\mathrm{Heat-diffusion}}$, and the sum of $F_{\mathrm{Vo-drift}}$ and $F_{\mathrm{Vo-diffusion}}$

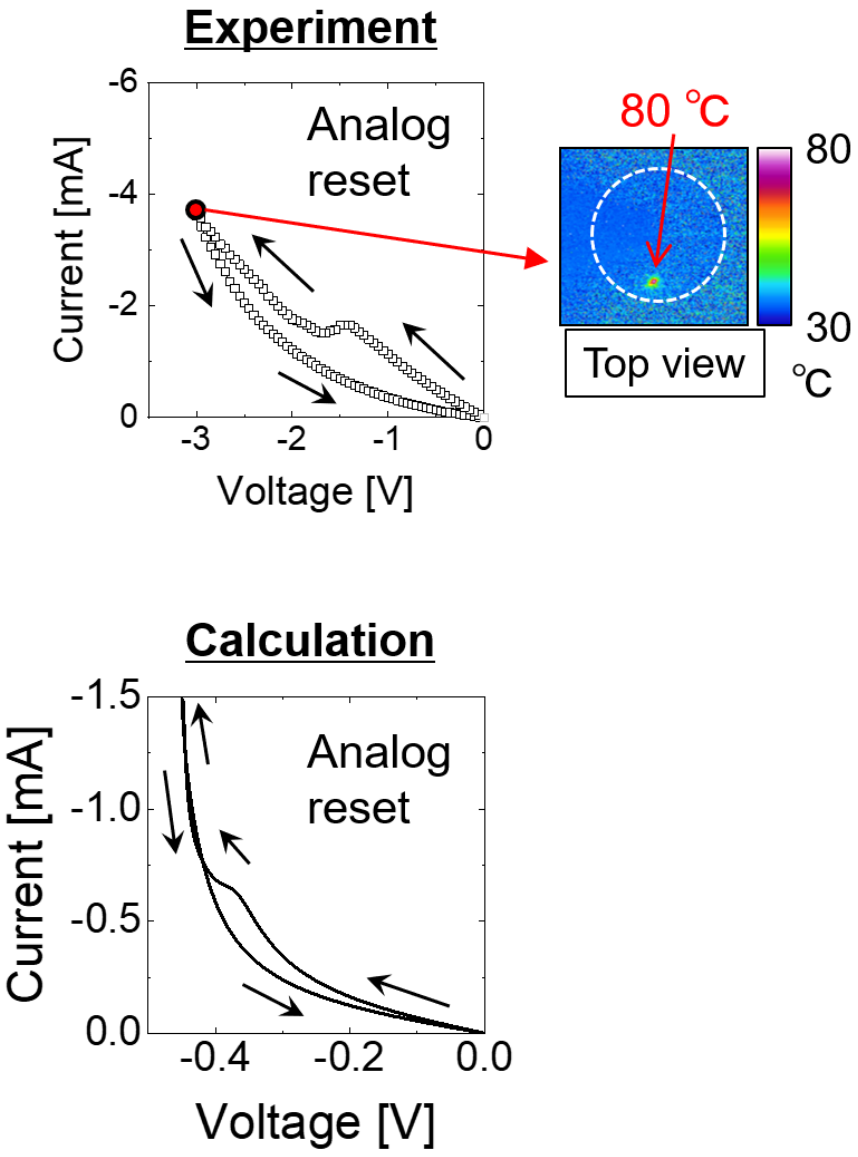

Figure 5.13: The experimental and calculation results of I–V characteristics. As for the experimental results, the maximum local temperature obtained in Sec. 5.2 is also shown for reference.

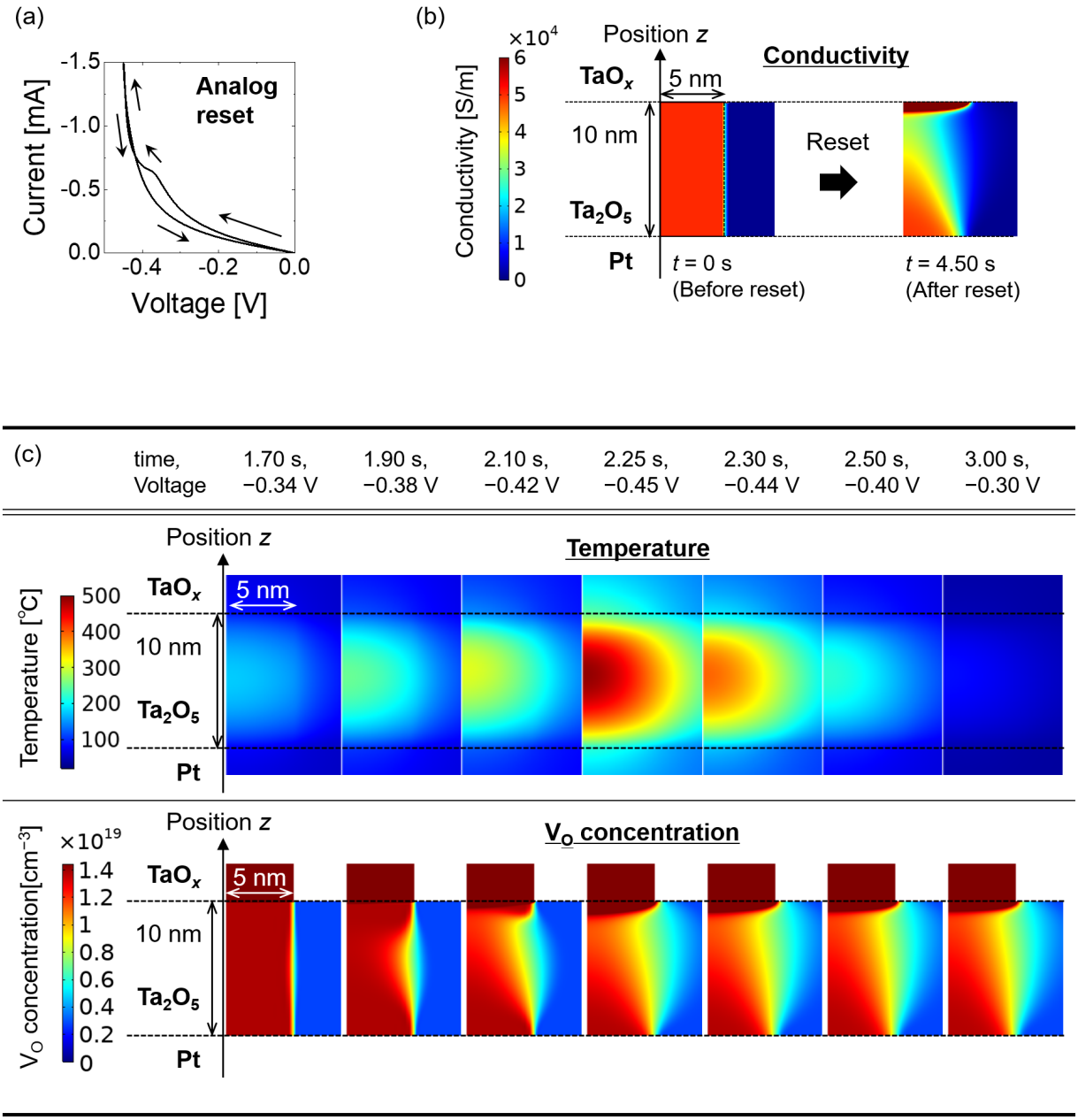

Figure 5.14: (a) The calculated I–V characteristics. (b) Distribution of the conductivity before and after the reset process. (c) Transient characteristics of the distribution of temperature T and V_O concentration c in the analog reset process.

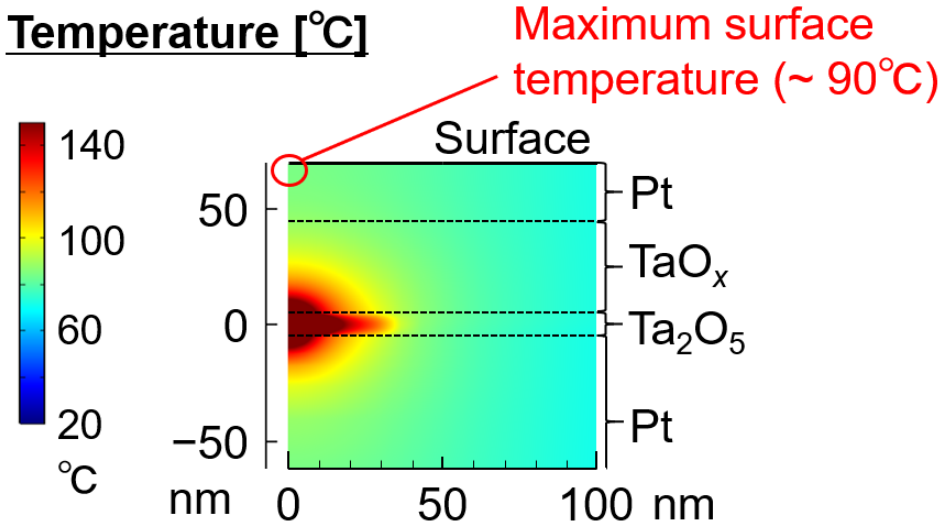

Figure 5.15: The temperature distribution including the Pt surface of the $Pt/TaO_x/Ta_2O_5/Pt$ cell when the center of the conductive filament reaches the maximum temperature. At this time, the temperature of the Pt surface also reaches its maximum of about 90 °C.

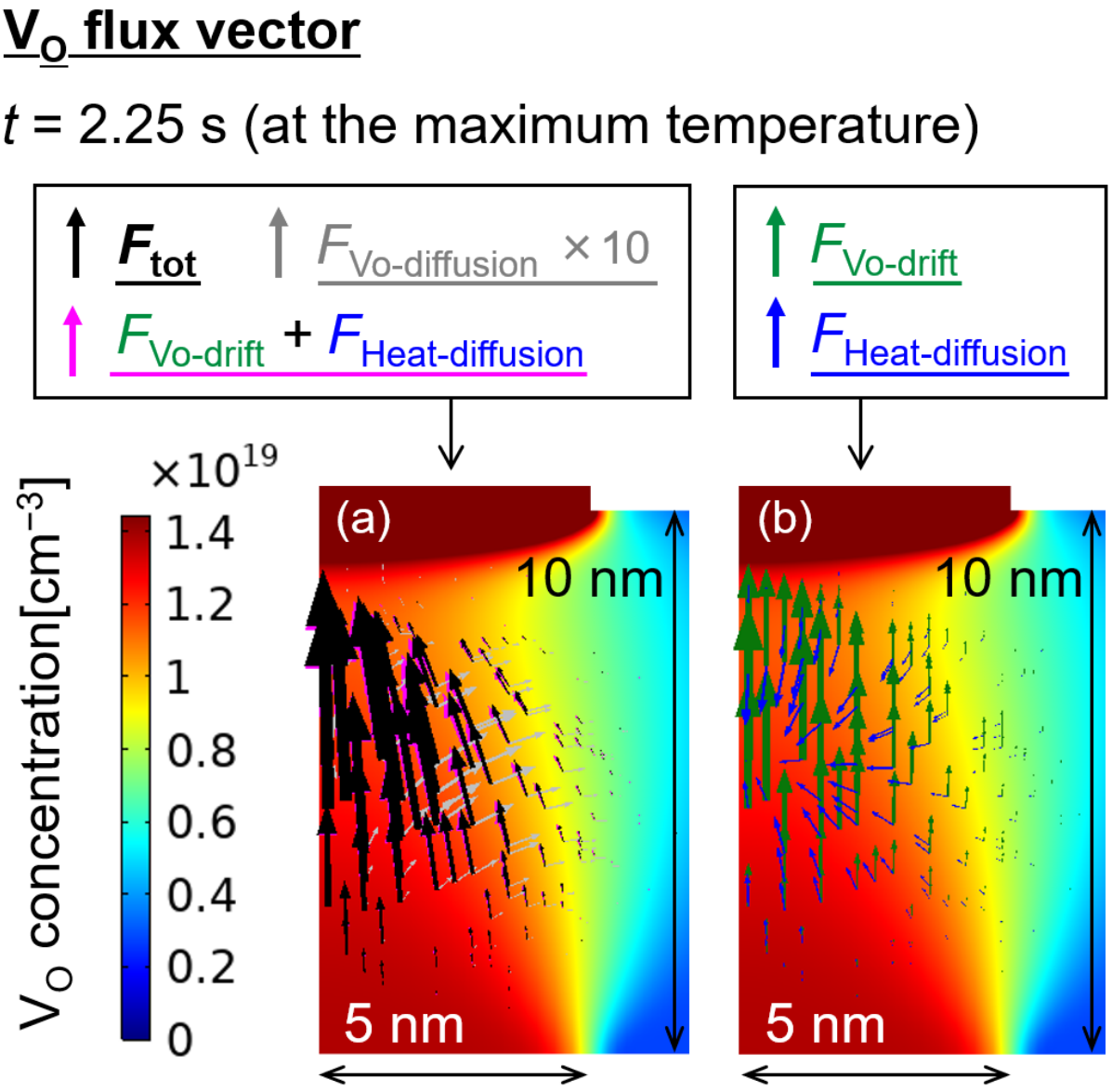

Figure 5.16: When the center of the conductive filament reaches the maximum temperature (t =2.25 s), V_O flux vectors on the V_O distribution. The components of V_O flux contributed by these three terms on the right side of Eq.(5.3), $F_{\mathrm{Heat-diffusion}}$, $F_{\mathrm{Vo-drift}}$ and $F_{\mathrm{Vo-diffusion}}$, and the sum of $F_{\mathrm{Heat-diffusion}}$, $F_{\mathrm{Vo-drift}}$ and $F_{\mathrm{Vo-diffusion}}$ is F_{tot}.

are compared, indicating that the contribution of the V_O diffusion due to the gradient of V_O concentration is sufficiently small to be ignored. Next, in Fig. 5.16 (b), $F_{\mathrm{Vo-drift}}$ and $F_{\mathrm{Vo-diffusion}}$ are compared, revealing that the main driving force for V_O transport is the V_O drift due to the gradient of electric potential although the contribution of the thermal diffusion due to the gradient of temperature cannot be ignored.

5.4 Discussion

In this section, the effects of Joule heating on the V_O drift were investigated in detail. Drift velocity of V_O (v_{V_O}), mobility of V_O (μ_{V_O}), and diffusivity of V_O (D_{V_O}) were defined by the following equations [20, 21];

$$v_{V_O} = \mu_{V_O}(-\nabla V), \tag{5.6}$$

$$\mu_{V_O} = \frac{Z_{V_O} e}{k_B T} D_{V_O}, \tag{5.7}$$

$$D_{V_O} = D_0 \exp\left[-\frac{U_a}{k_B T}\right], \tag{5.8}$$

where Z_{V_O}, D_0, and U_a are a valence of V_O, V_O diffusivity coefficient, and activation energy for V_O diffusivity, respectively. In this study, Z_{V_O}, D_0, and U_a are set to 2, 10^{-6} m^2/s, and 1.06 eV, respectively. Figure 5.17 (a) shows the transient characteristics of the V_O concentration distribution in the analog reset process from -0.36 V to -0.45 V. Figure 5.17 (b), (c), and (d) show transient characteristics of distributions on z-axis ($r = 0$) of electric field in the z-direction, temperature, and the drift velocity in the z-direction.The temperature rise at and near the center of the conductive filament in Fig. 5.17 (c) is attributed to Joule heating generated in the conductive filament. Moreover, these results in Fig. 5.17 (b)–(d) suggest that rising temperature at and near the center of the conductive filament causes an exponential increase in the drift velocity. Therefore, Joule heating generated in the conductive filament has a significant large effect on the diffusivity, which contributes to V_O drift rather than V_O diffusion. As a result, it was revealed that when a negative voltage is applied, V_O transport toward the TaO_x layer occurs due to the V_O drift, and that the conductive filament dissolves near the TaO_x layer in the Ta_2O_5 layer as shown in Fig. 5.17 (a).

5.5 Summary

Effects of Joule heating generated in the conductive filament on transport properties of V_Os in Pt/TaO_x/Ta_2O_5/Pt cells were investigated with both experimental and theoretical approaches. As for the experimental approach, local Joule heating was observed on the surface of Pt/TaO_x/Ta_2O_5/Pt cells during forming and various RS operations. As a result, it was revealed that a single conductive filament is locally formed at the semi-forming, that

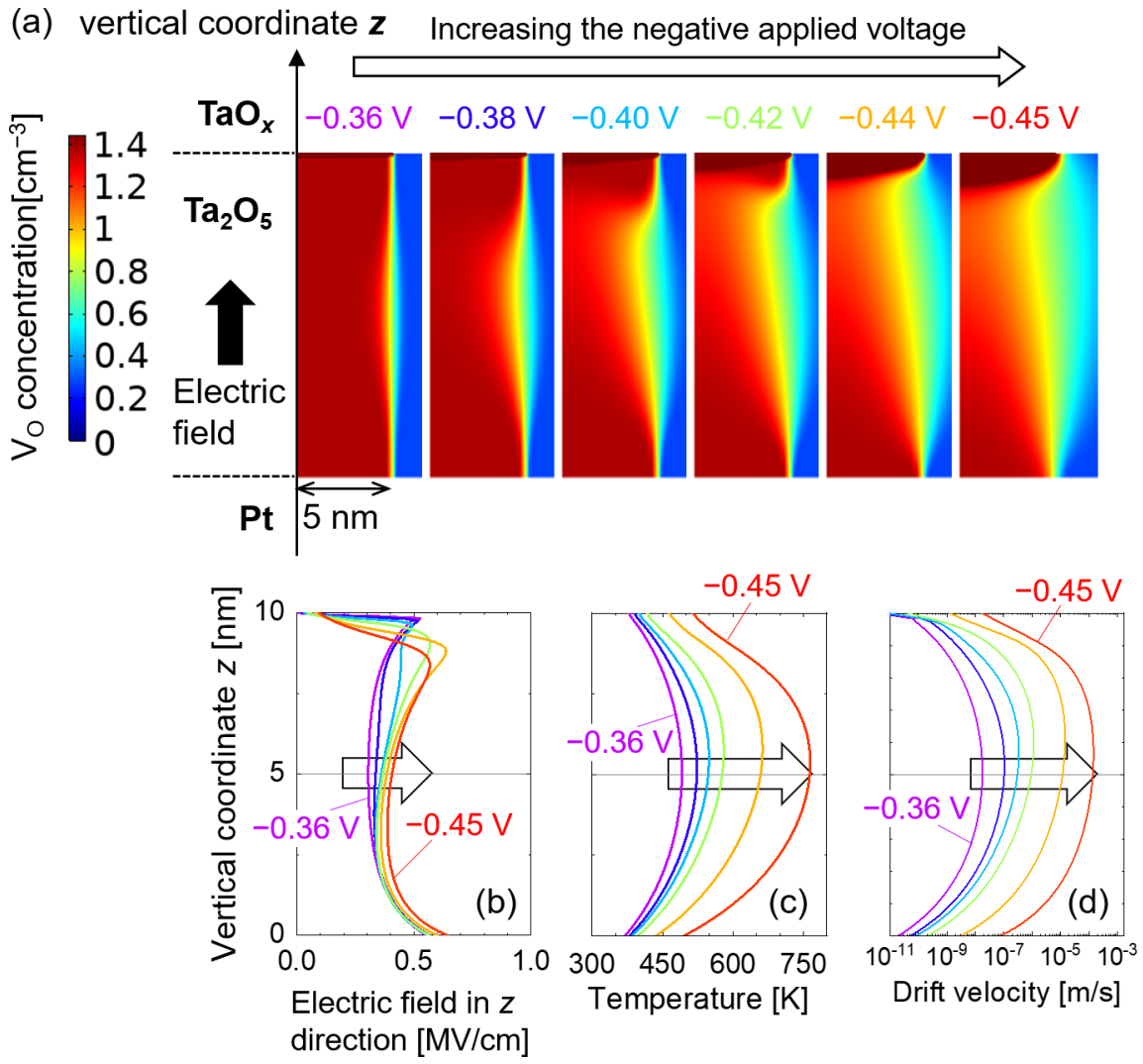

Figure 5.17: (a) Transient characteristics of the V_O concentration distribution in the analog reset process from −0.36 V to −0.45 V. (b) Transient characteristics of distributions on z axis ($r = 0$) of electric field in the z direction (c) Transient characteristics of distributions on z axis ($r = 0$) of temperature. (d) Transient characteristics of distributions on z axis ($r = 0$) of the drift velocity in the z direction.

the growth and dissolution of the conductive filament occur in the same local spot, and that the maximum surface temperature of the Pt/TaO_x/Ta_2O_5/Pt cells reaches about 80 °C when a few mA of current flows. As for the theoretical approach, a coupled simulation of electric potential distribution, temperature distribution, and V_O concentration distribution during a reset process in Pt/TaO_x/Ta_2O_5/Pt cells was performed. Here, key parameters for the calculations were determined based on the results in Chapters 2–4. As a result of the simulation, the current–voltage characteristics in a reset process were consistent with the experimental results. Analyses of the temperature distribution in Pt/TaO_x/Ta_2O_5/Pt cells indicated that the maximum surface temperature reaches about 90 °C when a current of 1.5 mA flows. Moreover, the transient analyses of V_O transport during the reset process revealed that the dominant driving force of V_O transport is the drift due to the electric field.

References

[1] T. Fujii, M. Arita, and Y. Takahashi, *Applied Physics Letters* **98**, 212104 (2011).

[2] Y. Yang, P. Gao, S. Gaba, T. Chang, X. Pan, and W. Lu, *Nature Communications* **3**, 732 (2012).

[3] M. Kudo, M. Arita, Y. Ohno, T. Fujii, K. Hamada, and Y. Takahashi, *Thin Solid Films* **533**, 48 (2013).

[4] Y. Sato, K. Kinoshita, M. Aoki, and Y. Sugiyama, *Applied Physics Letters* **90**, 033503 (2007).

[5] F. Miao, J. P. Strachan, J. J. Yang, M. X. Zhang, I. Goldfarb, A. C. Torrezan, P. Eschbach, R. D. Kelley, G. Medeiros-Ribeiro, and R. S. Williams, *Advanced Materials* **23**, 5633 (2011).

[6] C. Chen, C. Song, J. Yang, F. Zeng, and F. Pan, *Applied Physics Letters* **100**, 253509 (2012).

[7] J. J. Yang, D. B. Strukov, and D. R. Stewart, *Nature Nanotechnology* **8**, 13 (2013).

[8] K. Kinoshita, S. G. Koh, T. Moriyama, and S. Kishida, *Scientific Reports* **5**, 18442 (2015).

[9] S. U. Sharath, S. Vogel, L. Molina-Luna, E. Hildebrandt, C. Wenger, J. Kurian, M. Duerrschnabel, T. Niermann, G. Niu, P. Calka, M. Lehmann, H. J. Kleebe, T. Schroeder, and L. Alff, *Advanced Functional Materials* **27**, 1700432 (2017).

[10] Y. Nishi, H. Sasakura, and T. Kimoto, *Journal of Applied Physics* **124**, 152134 (2018).

[11] S. Petzold, E. Miranda, S. U. Sharath, J. Muñoz-Gorriz, T. Vogel, E. Piros, N. Kaiser, R. Eilhardt, A. Zintler, L. Molina-Luna, J. Suñé, and L. Alff, *Journal of Applied Physics* **125**, 234503 (2019).

[12] Y. Ma, D. A. Cullen, J. M. Goodwill, Q. Xu, K. L. More, and M. Skowronski, *ACS Applied Materials and Interfaces* **12**, 27378 (2020).

[13] L. Gao, Q. Ren, J. Sun, S. T. Han, and Y. Zhou, *Journal of Materials Chemistry C* **9**, 16859 (2021).

[14] Y. Nakamura and Y. Nishi, *Japanese Journal of Applied Physics* **61**, SM1012 (2022).

[15] S. Urakawa, S. Tomai, Y. Ueoka, H. Yamazaki, M. Kasami, K. Yano, D. Wang, M. Furuta, M. Horita, Y. Ishikawa, and Y. Uraoka, *Applied Physics Letters* **102**, 053506 (2013).

[16] K. Kado, M. Uenuma, K. Sharma, H. Yamazaki, S. Urakawa, Y. Ishikawa, and Y. Uraoka, *Applied Physics Letters* **105**, 123506 (2014).

[17] M. Uenuma, Y. Ishikawa, and Y. Uraoka, *Applied Physics Letters* **107**, 073503 (2015).

[18] F. Nardi, S. Larentis, S. Balatti, D. C. Gilmer, and D. Ielmini, *IEEE Transactions on Electron Devices* **59**, 2461 (2012).

[19] S. Larentis, F. Nardi, S. Balatti, D. C. Gilmer, and D. Ielmini, *IEEE Transactions on Electron Devices* **59**, 2468 (2012).

[20] S. Kim, S.-j. Kim, K. M. Kim, S. R. Lee, M. Chang, E. Cho, Y.-b. Kim, C. J. Kim, U. Chung, and I.-k. Yoo, *Scientific Reports* **3**, 1680 (2013).

[21] S. Kim, S. Choi, and W. Lu, *ACS Nano* **8**, 2369 (2014).

Chapter 6

Conclusions

6.1 Conclusions

In this thesis, forming and resistive switching phenomena in TaO_x-based resistive switching cells were studied with both experimental and theoretical approaches for establishing the analog resistive switching characteristics and for elucidating the mechanism of the conductive filament growth/dissolution during the analog resistive switching operations. The major conclusions obtained in this study are summarized as follows.

In Chapter 2, the author worked on modeling the reactive sputtering deposition of Ta oxides, based on experimental characterization of the deposited Ta oxide films. First, a simplified theoretical model (Berg's model) was used to calculate the relationship between the oxygen gas flow rate during deposition and the chemical composition of the Ta oxide films. Second, the composition of Ta oxide films fabricated with different oxygen gas flow rates during deposition was characterized by Rutherford backscattering spectroscopy, indicating that the experimental values of the chemical composition and the density were consistent with the calculated values. Third, the results of X-ray diffraction, cross-sectional transmission electron microscopy, and electron diffraction revealed that the Ta oxide films are microcrystalline close to amorphous. Finally, the high-resolution RBS for the TaO_x/TaO_y/Pt stacking samples, where the TaO_y and TaO_x layers were deposited at oxygen gas flow rates of 2.0 sccm (oxide mode) and 0.8–1.2 sccm (metal mode), respectively, revealed that the oxygen composition ratio in the TaO_x layer linearly increases from 1.51 to 2.13 with the oxygen gas flow rate during the TaO_x deposition and that the oxygen composition ratio of the TaO_y layer is 2.5 (stoichiometry). These results indicate that the oxygen composition of the Ta oxide deposited by reactive sputtering was precisely controlled by the oxygen gas flow rate.

In Chapter 3, the impacts of introducing a Ta-rich TaO_x layer on initial characteristics in Pt/Ta_2O_5/Pt cells were investigated by comparing the electrical properties of Pt/Ta_2O_5/Pt and Pt/TaO_x/Ta_2O_5/Pt cells. First, in Pt/TaO_x/Ta_2O_5/Pt cells, the large device-to-device variation in initial electrical characteristics observed in Pt/Ta_2O_5/Pt cells was significantly

reduced. Second, in Pt/TaO_x/Ta_2O_5/Pt cells, the temperature dependence of initial conductance with the small device-to-device variation was characterized in the wide temperature and frequency ranges to clarify the dominant conduction mechanism. The temperature dependence of DC conductance revealed that Mott variable range hopping (VRH) conduction is dominant in the low-temperature region below 200 K, and that both VRH conduction and band conduction contribute to the DC conductance in parallel from 200 K to 400 K. In contrast, the frequency characteristics of AC conductance at different temperatures indicated that the relaxation of small polarons formed by carriers in the localized states contributed to the AC conductance at high frequency. Moreover, the cell size dependence of AC conductance suggested that the introduction of a TaO_x layer formed filamentary conductive paths without applying voltage. Third, the results of secondary ion mass spectrometry for two samples prepared using oxygen isotopes as markers indicate that the deposition of a TaO_x layer on a Ta_2O_5 layer causes the migration of oxygen atoms from the Ta_2O_5 layer to the TaO_x layer, and the author proposed that oxygen vacancies (V_Os) are supplied from the TaO_x layer as a V_O reservoir to the Ta_2O_5 layer even in the as-deposited Pt/TaO_x/Ta_2O_5/Pt cells. Finally, by using the VRH conduction equation, the density of V_Os in the Ta_2O_5 layer, corresponding to the localized states, was estimated from the temperature dependence of the initial resistance in Pt/TaO_x/Ta_2O_5/Pt cells with different oxygen compositions of the TaO_x layer. It was quantitatively revealed that the density of V_Os supplied from the TaO_x layer to the Ta_2O_5 layer can be controlled by the oxygen composition (1.5–2.1) and thickness in the TaO_x layer.

In Chapter 4, forming and resistive switching characteristics were investigated in detail for demonstration of analog resistive switching characteristics in Pt/TaO_x/Ta_2O_5/Pt cells. First, the author found a unique forming phenomenon (semi-forming) that transitions to a high-resistance state of several kilo-ohms. The dependence of semi-forming properties on the density of oxygen vacancies supplied from the TaO_x layer to the Ta_2O_5 layer was investigated, revealing that the semi-forming phenomenon is more likely to occur when more oxygen vacancies are supplied to the Ta_2O_5 layer. Based on these results, the mechanism of semi-forming was proposed. Second, the author also found that in Pt/TaO_x/Ta_2O_5/Pt cells after semi-forming, set and subsequent reset processes occur when the negative applied voltage increases. Moreover, various operation modes of resistive switching can be controlled by adjusting the magnitude of the negative applied voltage: counterclockwise, complementary, and clockwise resistive switching. In particular, analog control of the cell resistance can be demonstrated even in the set processes in the complementary resistive switching of Pt/TaO_x/Ta_2O_5/Pt cells. The author proposed a qualitative model for the origin of the analog resistive switching that the growth and dissolution in the identical filament in the Ta_2O_5 layer could suppress each other. Finally, by appropriately adjusting the oxygen composition x and thickness of the TaO_x layer, both the initial resistance and the relative occurrence frequency of the semi-forming were successfully controlled to relatively high values of 1 MΩ and 0.9, respectively, leading to establishing the method to reduce an

operation current in analog resistive switching.

In Chapter 5, the effects of Joule heating generated in the conductive filament on the transport properties of V_Os in $Pt/TaO_x/Ta_2O_5/Pt$ cells were investigated with both experimental and theoretical approaches. As for the experimental approach, local Joule heating was observed on the surface of $Pt/TaO_x/Ta_2O_5/Pt$ cells during forming and various resistive switching operations. As a result, it was revealed that a single conductive filament is locally formed at the semi-forming, that the growth and dissolution of the conductive filament occur in the same local spot, and that the maximum surface temperature of the $Pt/TaO_x/Ta_2O_5/Pt$ cells reaches about 80 °C when a few mA of current flows. As for the theoretical approach, a coupled simulation of electric potential distribution, temperature distribution, and V_O concentration distribution during a reset process in $Pt/TaO_x/Ta_2O_5/Pt$ cells was performed. Here, key parameters for the calculations were determined based on the results in Chapters 2–4. As a result of the simulation, the current–voltage characteristics in a reset process were consistent with the experimental results. Analyses of the temperature distribution in $Pt/TaO_x/Ta_2O_5/Pt$ cells indicated that the maximum surface temperature reaches about 90 °C when a current of 1.5 mA flows. Moreover, the transient analyses of the V_O transport during the reset process revealed that the dominant driving force of the V_O transport is the drift due to the electric field.

6.2 Future outlook

Although the experimental and theoretical studies on resistive switching phenomena were performed from various viewpoints in this thesis, there still remain several issues to be solved. In this section, the author describes several challenges and suggestions as future outlooks.

Elucidation of V_O transport properties in analog set processes

In this thesis, the author simulated the distribution of V_O concentration and temperature in the analog reset process in the $Pt/TaO_x/Ta_2O_5/Pt$ cell. However, in order to completely clarify the mechanism of the V_O transport for the analog resistive switching, it is also necessary to calculate the distribution of V_O concentration and temperature in a set process.

Characterization of the cross-sectional structure of a conductive filament

Although *in-situ* observation of a conductive filament has been studied using transmission electron microscopy (TEM) [1, 2], the focused ion beam (FIB) process is used in these studies to extremely thin the resistive switching cells with respect to the vertical direction to the thickness direction, so there is a problem that the cell structure is greatly different from the practical device. In this thesis, by observing the temperature rise using an infrared detector during the semi-forming and subsequent analog resistive switching operations, the

author successfully identified the local spot where the growth and dissolution of a conductive filament occurs. Then, observation of the cross-sectional structure of the identified local spot for several cells with various resistance states could reveal the structure of a conductive filament in the practical resistive switching cells.

Characterization of performance as memory cells

Regarding the analog resistive switching characteristics obtained in this thesis, the basic characteristics as memory devices, such as endurance and retention, have not yet been evaluated. For the application of the $Pt/TaO_x/Ta_2O_5/Pt$ cells to analog memory devices, it is necessary to miniaturize the cell size and characterize these memory performances. It is also necessary to elucidate the impacts of V_O transport properties on such memory performances to obtain guidelines for an optimal device design.

References

[1] T. Fujii, M. Arita, and Y. Takahashi, *Applied Physics Letters* **98**, 212104 (2011).

[2] M. Kudo, M. Arita, Y. Ohno, T. Fujii, K. Hamada, and Y. Takahashi, *Thin Solid Films* **533**, 48 (2013).

Appendix A

Reactive Sputtering Model

Berg' model is well known as one of quantitative models of reactive sputtering. The model assumes the steady-state values, instead of time-variations during reactive sputtering [1, 2].

A.1 Equations in Berg's model

Fig. A.1 and Fig. A.2 show schematic illustrations of reactive sputtering. A uniform partial pressure P of reactive gas causes a uniform bombardment of neutral reactive molecules F (molecules/unit area and time) to all surfaces in the processing chamber. The relationship between F and P is described by

$$F = \frac{P}{\sqrt{2kT\pi m}} \tag{A.1}$$

where k_{B}, T, and m are the Boltzmann constant, temperature in the chamber, and the mass of the reactive gas molecule, respectively. The total supply of the reactive gas Q_{tot} is the sum of all sources for the reactive gas consumption, the consumption at the target Q_{t}, the consumption at the collector (including the substrate) Q_{c}, and the evacuation by a pump Q_{p}:

$$Q_{\mathrm{tot}} = Q_{\mathrm{t}} + Q_{\mathrm{c}} + Q_{\mathrm{p}} \tag{A.2}$$

$$= \alpha_{\mathrm{t}} F(1-\theta_{\mathrm{t}})A_{\mathrm{t}} + \alpha_{\mathrm{c}} F(1-\theta_{\mathrm{c}})A_{\mathrm{c}} + SP, \tag{A.3}$$

where α_{t} and α_{c} are the sticking coefficient for unreacted fraction at the target and at the collector, respectively. Moreover, θ_{t} and θ_{c} are the compound fraction at the target with a size of $A_{\mathrm{t}}$and at the collector with a size of A_{c}, respectively, and S is pumping speed. Here, the total number of sputtered compound molecules F_{c} and metal atoms F_{m} per unit time from the target can be described by

$$F_{\mathrm{c}} = \frac{J}{q} Y_{\mathrm{c}} \theta_{\mathrm{t}} A_{\mathrm{t}}, \tag{A.4}$$

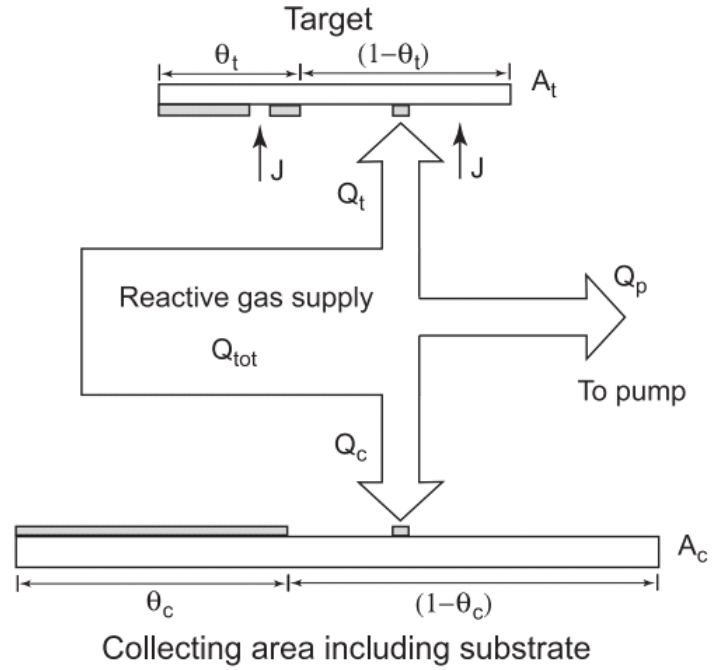

Figure A.1: .

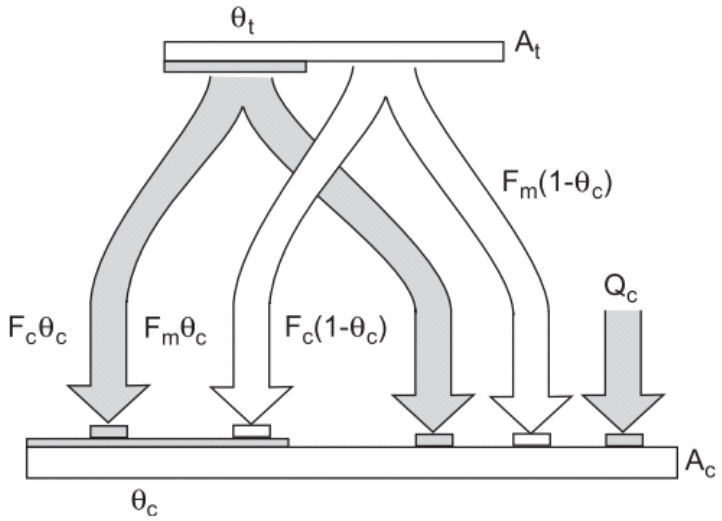

Figure A.2: Illustration of flux of sputtered material to the substrate area A_c.

$$F_{\mathrm{m}} = \frac{J}{q} Y_{\mathrm{m}} \left(1 - \theta_{\mathrm{t}}\right) A_{\mathrm{t}}, \tag{A.5}$$

where J is the ion current density to the target, q is the elementary charge, and Y_{c} and Y_{m} are the sputtering yield of compound molecules and metal molecules, respectively.

The author assumes reactive atom composition n in the compound MX_n (M: metal, X: reactive gas). Therefore, a steady-state equation of X atoms for the target is described as follow:

$$nF_{\mathrm{c}} = 2Q_{\mathrm{t}}. \tag{A.6}$$

Here, a factor of 2 means the number of atoms per the reactive gas molecule, such as O_2 and N_2. In the similar manner, a steady-state equation for the collecting area is described as follow:

$$2Q_{\mathrm{c}} + nF_{\mathrm{c}} \left(1 - \theta_{\mathrm{c}}\right) = \theta_{\mathrm{c}} F_{\mathrm{m}}. \tag{A.7}$$

Note that the terms on the left and right hand correspond the contributions supporting an increase and decrease in θ_{t}, respectively.

A.2 O_2 flow rate dependence

The author calculated the dependences of characteristic parameters on oxygen gas flow rate (Q_{tot}) during the deposition of tantalum oxides.

Partial pressure

θ_{t} and θ_{c} can be derived from Eqs. (A.4)–(A.7). Q_{tot}can be easily described as a function of the O_2 partial pressure P by using Eqs. (A.1)–(A.3).

Deposition rate

When the compound fraction θ_{c} at A_{c} are calculated, the deposition rate D is expressed as

$$D = \frac{F_{\mathrm{m}} + F_{\mathrm{c}}}{A_{\mathrm{c}}} \left[c_1(1 - \theta_{\mathrm{c}}) + c_2\theta_{\mathrm{c}}\right] \tag{A.8}$$

where c_1 and c_2 are constants accounting for unit conversions. The first term represents the contribution by elemental metal atoms, while the second term represents the contribution by compound material. In the deposition of tantalum oxides, c_1 and c_2 are 1.81 $\times 10^{-23}$ cm^3 and 8.44 $\times 10^{-23}$ cm^3, respectively.

Oxygen composition

The oxygen composition x in the tantalum oxide layer is equivalent to $n\theta_c$. Note that the author assumed n as 2.5 because oxygen composition of stoichiometric tantalum oxide is 2.5.

References

[1] S. Berg, H. Blom, T. Larsson, and C. Nender, *Journal of Vacuum Science & Technology A: Vacuum, Surfaces, and Films* **5**, 202 (1987).

[2] S. Berg and T. Nyberg, *Thin Solid Films* **476**, 215 (2005).

Appendix B

Simulation of electric field and electric potential

To verify the validity of considering the size of the top electrode (TE) as that of the $Pt/TaO_x/Ta_2O_5/Pt$ cell, the author simulated the distributions of electric potential and electric field in $Pt/TaO_x/Ta_2O_5/Pt$ cells.

B.1 Simulation methods

The distributions of electric potential and electric field in steady state were calculated by solving a current continuity equation for electrical conduction using a numerical solver (COMSOL Multiphysics). The current continuity equation is presented by

$$\nabla \cdot (\sigma \nabla V) = 0, \tag{B.1}$$

where σ and V are conductivity and electric potential, respectively.

For simplicity, the cell structure was defined in an axisymmetric two-dimensional cylindrical coordinate with radial coordinate r and vertical coordinate z, as shown in Fig. B.1. As shown in Fig. B.1, the boundary conditions were 0 V on the bottom of the Pt bottom electrode (BE) and 1 V on the top of the Pt TE. Other boundaries were assumed to be electrically insulated. The initial value of electric potential was set to 0 V in all domains. The conductivity of Pt was set to be 9.4 $\times 10^6$ S/m. The conductivities of TaO_x and Ta_2O_5 can vary depending on V_O density. Based on the previous study reported by Bondi *et al.* [1], it was assumed that the conductivity of the TaO_x layer changes from 10^4 S/m to 10 S/m when the oxygen composition of the TaO_x layer changes from 1.5 to 1.8. Moreover, from the experimental results in Chap. 3, since the density of V_Os in the Ta_2O_5 layer supplied from the TaO_x layer depends on the oxygen composition of the TaO_x layer, the conductivity of the Ta_2O_5 layer also depends on the oxygen composition of the TaO_x layer. Therefore, it was assumed that the conductivity of the Ta_2O_5 layer changes from 10^{-3} S/m to 10^{-6} S/m when the oxygen composition of the TaO_x layer changes from 1.5 to 1.8. Under the above

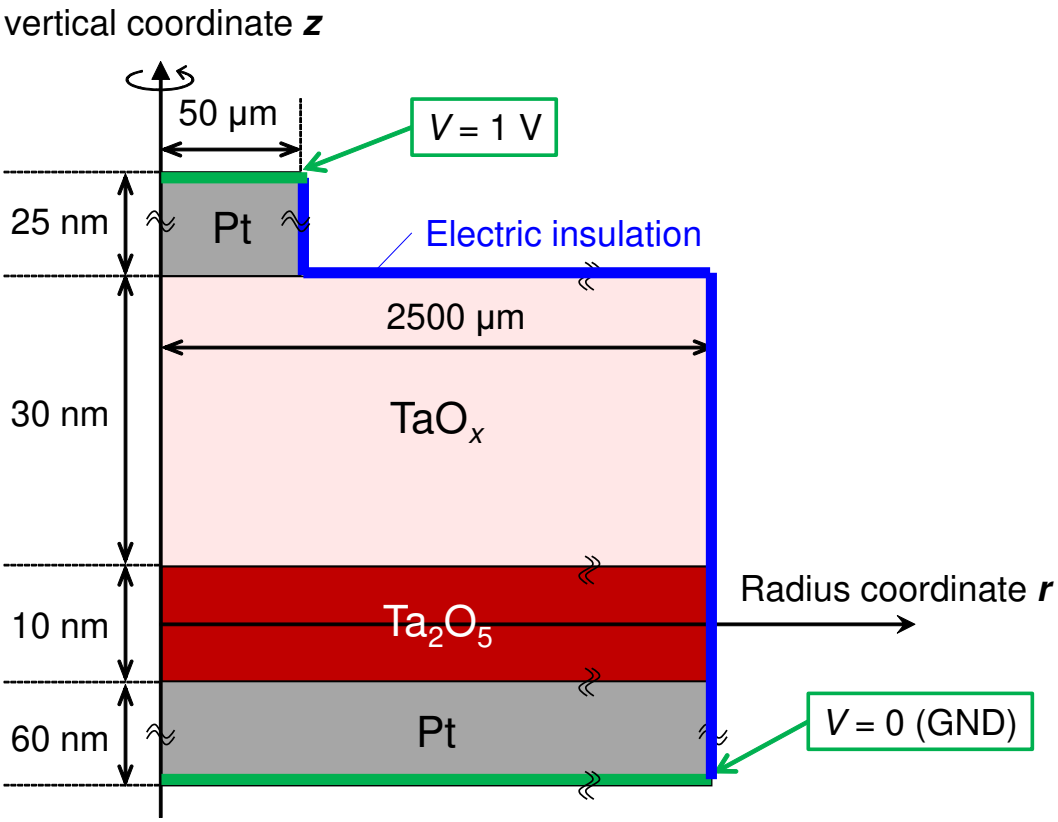

Figure B.1: Cell structure in an axisymmetric two-dimensional cylindrical coordinate with radial coordinate r and vertical coordinate z.

conditions, the distributions of electric potential and electric field were calculated when the oxygen compositions x of the TaO_x layer were 1.5 and 1.8.

B.2 Distributions of electric potential and electric field

Figure B.2 shows the distribution of the electric potential when the oxygen compositions x of the TaO_x layer were 1.5 and 1.8. Note that the scale in the z direction was multiplied by 2000 with respect to the r direction. These results indicates that the spread of electric potential is small enough to be neglected with respect to the size of the Pt TE in both cases of x. Moreover, Fig. B.3 shows the distribution of the electric field when the oxygen compositions x of the TaO_x layer were 1.5 and 1.8, indicating that the electric field intensity is almost zero in the TaO_x layer and that the electric field intensity is maximum in the Ta_2O_5 layer just below the Pt TE.

References

[1] R. J. Bondi, M. P. Desjarlais, A. P. Thompson, G. L. Brennecka, and M. J. Marinella, *Journal of Applied Physics* **114**, 203701 (2013).

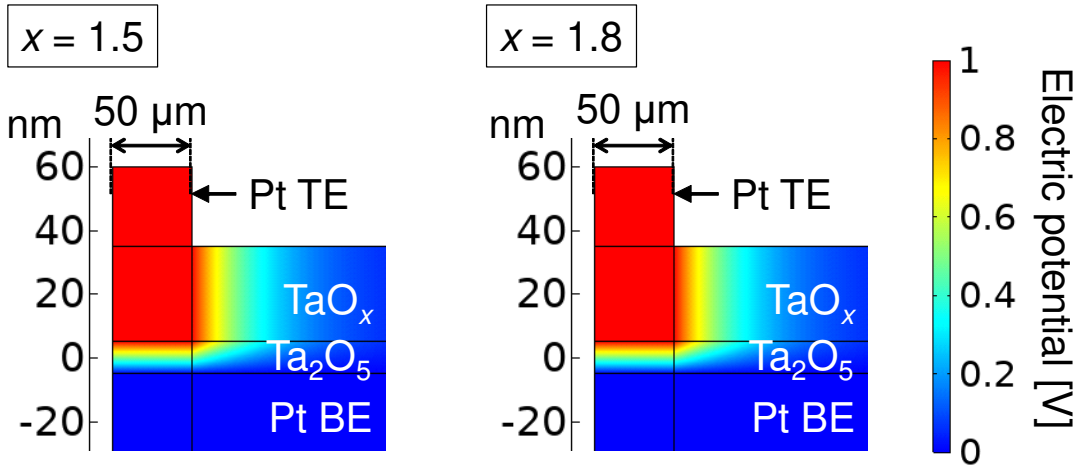

Figure B.2: Distribution of the electric potential when the oxygen compositions x of the TaO_x layer were 1.5 and 1.8.

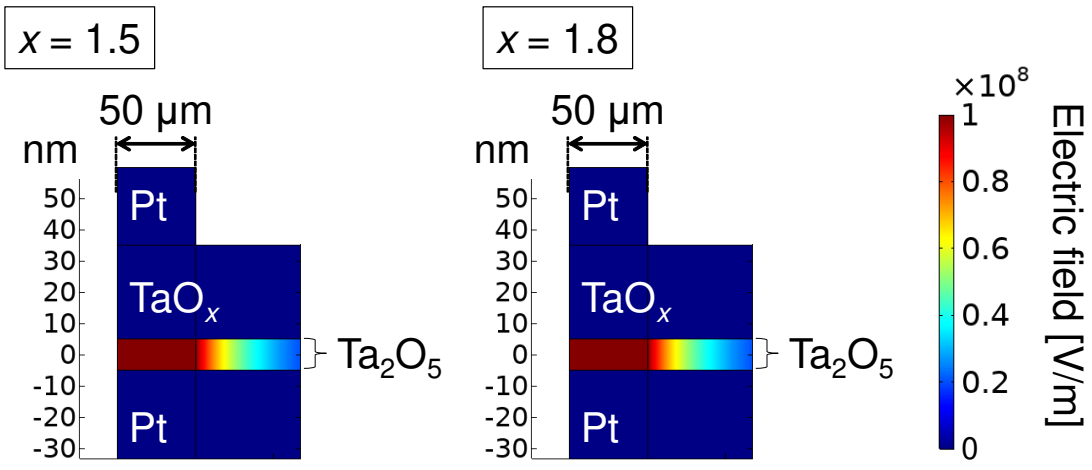

Figure B.3: Distribution of the electric field when the oxygen compositions x of the TaO_x layer were 1.5 and 1.8.

List of Publications

A. Full Length Papers and Letters

1. T. Miyatani, Y. Nishi, and T. Kimoto,
"Two modes of bipolar resistive switching characteristics in asymmetric TaO_x-based ReRAM cells,"
MRS Advances **4**, 2601 (2019).

2. T. Miyatani, Y. Nishi, and T. Kimoto,
"Dominant conduction mechanism in TaO_x-based resistive switching devices,"
Japanese Journal of Applied Physics **58**, 090914 (2019).

3. T. Miyatani, Y. Nishi, and T. Kimoto,
"Methods of controlling operation modes in Pt/TaO_x/Ta_2O_5/Pt resistive switching cells,"
Japanese Journal of Applied Physics **61**, SM1006 (2022).

4. T. Miyatani, T. Kimoto, and Y. Nishi,
"Reduction in current range of analog resistive switching operation by suppressing supply of oxygen-vacancy in Pt/TaO_x/Ta_2O_5/Pt cells,"
in preparation.

B. International Conferences

1. T. Miyatani, Y. Nishi, and T. Kimoto,
"DC and AC electrical characteristics of Ta_2O_5-based ReRAM cells,"
31st International Microprocesses and Nanotechnology Conference 2018 (MNC31), Sapporo, Japan, Nov. (2018), 16P-11-24, poster.

2. T. Miyatani, Y. Nishi, and T. Kimoto,
"Analyses on carrier transport in TaO_x-based ReRAM cells,"
International Symposium on Photonics and Electronics Science and Engineering 2019, Kyoto, Japan, Mar. (2019), P-14, poster.

3. T. Miyatani, Y. Nishi, and T. Kimoto,
   "Impacts of an asymmetric stack structure in TaO_x-based ReRAM cells on resistive switching characteristics,"
   Material Research Society Spring Meeting (MRS spring 2019), Phoenix, USA, Apr. (2019), EP09.07.02, oral.

4. T. Miyatani, Y. Nishi, and T. Kimoto,
   "Gradual resistive switching characteristics in $Pt/TaO_x/Ta_2O_5/Pt$ cells,"
   International Symposium on Creation of Advanced Photonic and Electronic Devices 2020, Kyoto, Japan, Mar. (2020), A-17, poster.

5. T. Miyatani, Y. Nishi, and T. Kimoto,
   "Improvement of analog resistive switching characteristics in TaO_x-based synaptic devices through complementary resistive switching,"
   Material Research Society Spring/Fall Meeting 2020 (MRS spring/fall 2020), Virtual, Nov. (2020), F.NM07.06.06, oral.

6. T. Miyatani, Y. Nishi, and T. Kimoto,
   "Correlation Between Depth Distribution of Chemical Compositions and Resistive Switching Characteristics in $Metal/Ta_2O_5/Pt$ Cells,"
   Material Research Society Spring/Fall Meeting 2020 (MRS spring/fall 2020), Virtual, Nov. (2020), F.NM07.11.08, poster(short presentation).

7. T. Miyatani, Y. Nishi, and T. Kimoto,
   "Complementary Resistive Switching Characteristics and Gradual Set/Reset Processes in $Pt/TaO_x/Ta_2O_5/Pt$ Cells,"
   4th International Conference on Memristive Materials Devices & Systems (MEMRISYS 2021), Virtual, Nov. (2021), 2A-5, oral.

8. T. Miyatani, T. Kimoto, and Y. Nishi,
   "Impacts of Oxygen Composition in an Oxygen-vacancy Reservoir Layer on Forming and Resistive Switching Characteristics in $Pt/TaO_x/Ta_2O_5/Pt$ Cells," [Excellent Poster Presentation Awards]
   4th International Conference on Memristive Materials Devices & Systems (MEMRISYS 2021), Virtual, Nov. (2021), 19, poster.

9. T. Miyatani, T. Kimoto, and Y. Nishi,
   "Oxygen composition dependence of forming characteristics in analog resistive switching cells with $Pt/TaO_x/Ta_2O_5/Pt$ stack structure,"
   Material Research Society Fall Meeting 2021 (MRS fall 2021), Virtual, Nov. (2021), SB04.08.05, oral.

10. T. Miyatani, T. Kimoto, and Y. Nishi,
"Reduction of the operating current range of analog resistive switching in $Pt/TaO_x/Ta_2O_5/Pt$ cells by controlling the supply of oxygen vacancies,"
Material Research Society Spring Meeting 2022 (MRS spring 2022), Virtual, May (2021), EQ11.14.03, oral.